REVIEW

The scattering of fast electrons by crystals

Rep. Prog. Phys., Vol. 42, 1979. Printed in Great Britain

The scattering of fast electrons by crystals

C J HUMPHREYS

Department of Metallurgy and Science of Materials, University of Oxford, Oxford OX1 3PH
and
Jesus College, Oxford

Abstract

Electron diffraction and microscopy are among the most important techniques for studying the structures of solids. This review aims to give a comprehensive introduction to the basic principles of the scattering of fast electrons and to highlight selected applications of importance. It begins by discussing electron scattering by single atoms and describes how single atoms may be imaged. The geometry of diffraction from perfect single crystals is then considered and a simple kinematical theory which yields approximate values for diffracted intensities is given. It is shown how simple principles have been used to image monatomic steps on the surface of crystals.

More accurate methods of calculating diffracted intensities are given and particular attention is paid to describing concepts often found to be difficult, for example the dispersion surface. Principles of various recent electron scattering techniques are outlined including high-voltage electron microscopy, scanning electron microscopy, convergent-beam electron diffraction and the critical voltage effect. Applications described range from measuring bonding electron charge densities to the imaging of dislocations. Finally some recent theoretical developments on the problem of imaging imperfect crystals at atomic resolution are discussed.

This review was received in February 1979.

0034–4885/79/111825+72 $05.00

Contents

1. Introduction

1.1. Historical background

In 1906 J J Thomson was awarded the Nobel Prize for demonstrating that the electron was a particle. Thirty-one years later his son, G P Thomson, was awarded the Nboel Prize for demonstrating that the electron was a wave. The experimental verification of the wave nature of the electron by Thomson and Reid (1927) in Britain, and independently by Davisson and Germer (1927) in America, resulted from the first controlled experiments on the scattering of incident electrons by crystals, prompted by the theoretical deduction of the wave nature of the electron by Louis de Broglie (1924).

At about the same time Heisenberg (1925) and Schrödinger (1926) had begun to build a wave theory of matter and Bethe (1928) applied the Schrödinger equation to the problem of the scattering of a beam of fast electrons by the periodic potential of a crystal. Thus in the space of a few years the theory and practice of the scattering of electrons by crystals was born and achieved significant growth.

The next thirty years saw the gradual development of electron diffraction cameras and electron microscopes. In the last twenty years an enormous expansion of the theory and the practice of electron microscopy has occurred, largely stemming from the discovery that dislocations and other crystalline defects could be imaged in the electron microscope (Hirsch *et al* 1956, Bollmann 1956). In the last few years a similar expansion in very high resolution electron microscopy has started to occur, the study of the structure of matter by imaging the individual atoms that compose it. The resolution necessary to achieve this is obtainable in principle because beams of electrons with wavelengths less than 0·1 Å are easily produced. However, only recently have electron microscopes been produced with aberrations sufficiently low that atomic resolution in images is a practical possibility. The best point-to-point resolution currently available in electron microscopes is 2–3 Å, close to the inter-atomic distances in some solids. Examples of very high resolution images are shown in figures 1 (plate), 2 (plate) and 11 (plate).

1.2. Scope of the review

This review considers the scattering of a beam of fast electrons, fast being roughly defined as the speed of electrons having kinetic energy between about 1 keV to 10 MeV. For 1 keV electrons, the wavelength, λ, is 0·39 Å and the ratio of the electron velocity to the velocity of light, v/c, is 0·06. Electrons slower than this are unlikely to be useful for high resolution imaging studies and their scattering by crystals is complicated by exchange and virtual inelastic scattering effects (see the book by Pendry (1974) for a treatment of low-energy electron scattering). 10 MeV electrons have $\lambda = 0{\cdot}001$ Å and $v/c = 0{\cdot}999$. They are highly relativistic and at higher energies than this bremsstrahlung losses become severe, making it unlikely that such electrons would be useful for diffraction and microscopy work. (The specimen would also be seriously damaged owing to the incident electrons causing many atomic displacements.)

The purpose of this article is to review the basic theory of the scattering of fast

electrons by crystals, starting from first principles. Because the electron microscope is the most important instrument utilising electron scattering from crystals, examples have been given in the text from the world of electron microscopy. However, this review is basically about electron scattering and it is hoped that the text will be of use to all interested in the mechanisms of electron diffraction.

The starting point is the elastic and inelastic scattering of electrons by single atoms, §2, which includes a description of how the known angular distribution of such scattering has been used to image isolated single atoms. Section 3 considers the geometry of scattering by crystals, simple kinematical scattering theory, double diffraction, forbidden reflections and the imaging of monatomic surface steps. The important question of the nature of the crystal potential seen by incident fast electrons is discussed in §4 followed by a development of dynamical diffraction theory for non-absorbing perfect crystals. Particular attention has been paid to explaining concepts often found difficult, for example the dispersion surface.

Inelastic scattering and absorption are considered in §5 together with a description of various important recent developments: penetration in high voltage microscopy; back-scattering in scanning electron microscopy; the reciprocity theorem and scanning transmission electron microscopy; convergent-beam diffraction, zone-axis patterns and their relevance to accurate symmetry determination; the critical voltage effect and its relevance to determining solid-state bonding effects in crystals. The final section discusses diffraction from imperfect crystals with particular emphasis on recent experimental and theoretical developments: the weak-beam technique, the avoidance of the column approximation and elastic diffuse imaging.

1.3. Notation

Unfortunately there is considerable variation in diffraction theory notation. Solid-state physicists usually define the wavevector $\boldsymbol{k}$ and the reciprocal lattice vector $\boldsymbol{g}$ as having magnitudes $|\boldsymbol{k}| = 2\pi/\lambda$ and $|\boldsymbol{g}| = 2\pi/d$, respectively. Crystallographers, on the other hand, usually use

$$|\boldsymbol{k}| = 1/\lambda \qquad |\boldsymbol{g}| = 1/d. \tag{1.1}$$

Some texts (e.g. Cowley 1975) use a hybrid system:

$$|\boldsymbol{k}| = 2\pi/\lambda \qquad |\boldsymbol{g}| = 1/d.$$

Throughout this review we define reciprocal space quantities as being true reciprocals as in equation (1.1). This is preferable from a purist viewpoint and also it simplifies the Fourier transform definition (see below).

The plane wave solutions of the time-independent wave equation

$$\nabla^2\psi + 4\pi^2k^2\psi = 0$$

are $\psi = \exp(+2\pi i\boldsymbol{k}.\boldsymbol{r})$ and $\psi = \exp(-2\pi i\boldsymbol{k}.\boldsymbol{r})$.

We choose $\psi = \exp(+2\pi i\boldsymbol{k}.\boldsymbol{r})$ to represent a plane wave proceeding in the direction specified by the vector $\boldsymbol{k}$ (and $\exp(-2\pi i\boldsymbol{k}.\boldsymbol{r})$ to represent the wave with vector $-\boldsymbol{k}$). About 50% of diffraction and wave mechanics texts adopt this convention, the other half associating the wave $\exp(-2\pi i\boldsymbol{k}.\boldsymbol{r})$ with the vector $\boldsymbol{k}$. Both conventions are equally valid but it is important to be consistent in subsequent mathematics (many texts are not!).

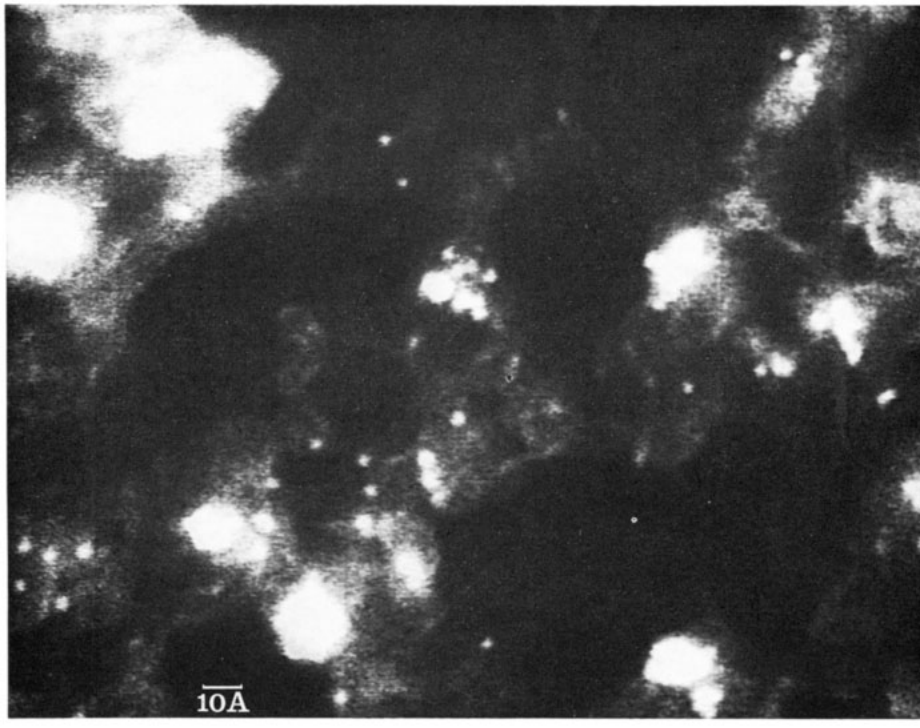

Figure 1. Images of single atoms. The single bright spots are images of single gold atoms, the larger bright spots are clusters of atoms. Specimens prepared by depositing gold chloride solvent onto a 15 Å thick carbon film. (Courtesy of M Isaacson, M Utlaut and M Ohtsuki.)

Adopting the above notation, the Fourier transform of a one-dimensional function $f(x)$ is defined as

$$\mathscr{F}[f(x)] \equiv F(u) = \int_{-\infty}^{\infty} f(x) \exp(-2\pi i u x)\, \mathrm{d}x \tag{1.2}$$

and the inverse transform is defined as

$$f(x) = \int_{-\infty}^{\infty} F(u) \exp(+2\pi i u x)\, \mathrm{d}u. \tag{1.3}$$

If the solid-state physicists convention of defining reciprocal-space quantities is adopted, the 2π is omitted from the exponent in equations (1.2) and (1.3). It must then be included as a constant: either both integrals in (1.2) and (1.3) are multiplied by $(2\pi)^{-1/2}$, or the integral in (1.2) or (1.3) is multiplied by $(2\pi)^{-1}$. If $\exp(-2\pi i \boldsymbol{k}.\boldsymbol{r})$ is chosen as the wave with vector $+\boldsymbol{k}$ then the signs of the exponents in (1.2) and (1.3) must be changed.

The question of notation has been discussed in detail above since it is a common source of confusion. A list of the symbols more frequently used in this article follows.

v	velocity of electron
c	velocity of light
λ	electron wavelength (relativistically correct)
$\boldsymbol{k}$	electron wavevector ($\lvert\boldsymbol{k}\rvert = \lambda^{-1}$)
d	an interplanar lattice spacing
$\boldsymbol{g}$	a reciprocal lattice vector ($\lvert\boldsymbol{g}\rvert = d^{-1}$)
ψ	a wavefunction
m_0	electron rest mass
m	electron mass (relativistically correct)
e	magnitude of the electron charge ($= \lvert e \rvert$)
E	electron accelerating potential
$V^{\mathrm{opt}}(\boldsymbol{r})$	an optical potential
$V(\boldsymbol{r})$	real, Coulomb, potential
$\mathrm{i}V'(\boldsymbol{r})$	imaginary part of the optical potential
$\Delta V(\boldsymbol{r})$	real contribution to the optical potential, due to virtual inelastic scattering
V_g	gth Fourier coefficient of $V(\boldsymbol{r})$
$U(\boldsymbol{r})$	a 'modified potential' ($U(\boldsymbol{r}) = 2meV(\boldsymbol{r})/h^2$)
U_g	gth Fourier coefficient of $U(\boldsymbol{r})$
θ	half-angle of scattering
θ_{B}	the Bragg angle
f	atomic scattering amplitude for electrons
f^{B}	first Born approximation atomic scattering amplitude for electrons
f^{x}	atomic scattering factor for x-rays
$\boldsymbol{k}'$	wavevector of a scattered wave
$\boldsymbol{K}'$	a 'scattering vector' ($\boldsymbol{K}' = \boldsymbol{k}' - \boldsymbol{k}$)
$\boldsymbol{K}$	the wavevector of the incident electron inside the mean inner potential of the crystal
Z	atomic number
r_{e}	classical electron radius ($r_{\mathrm{e}} = e^2/mc^2$)
σ	cross section
F_g	electron structure amplitude for reflection g

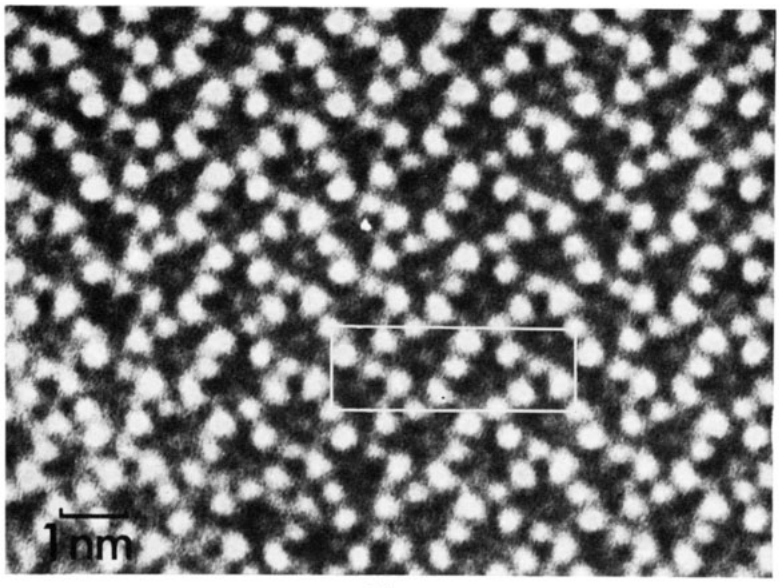

(*a*)

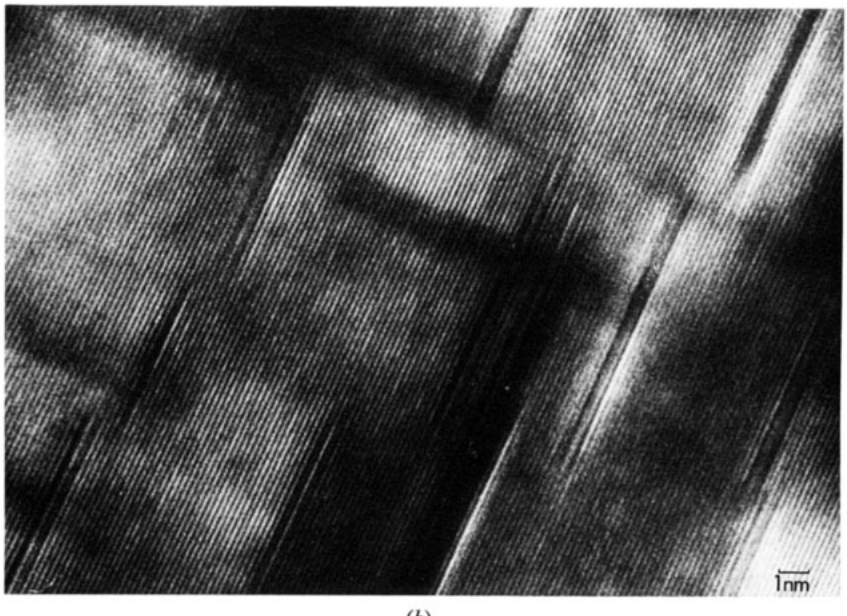

(*b*)

Figure 2. (*a*) High resolution structure image of a thin crystal of $4Nb_2O_5.9WO_3$. The unit cell is outlined. White patches in the image correspond to empty square and pentagonal tunnels in the structure (from Iijima and Allpress (1974), by courtesy of the International Union of Crystallography). (*b*) High resolution lattice fringe image of precipitates in an aluminium–copper alloy. The spacing of (200) planes in the perfect Al–Cu crystal is 2·0 Å. The fringe spacing varies between 2·0 Å (in perfect regions) and 1·7 Å. (Courtesy of E D Boyes.)

ξ_g	extinction distance for reflection g
s	vector in reciprocal space indicating the deviation from the exact Laue condition
w	a deviation parameter ($w=s\xi_g$)
β	a deviation parameter ($\cot\beta=w$)
V_{cell}	volume of unit cell
V_c	the critical voltage
t	crystal thickness
M	Debye–Waller factor
$\psi^{(j)}$	wavefunction of the jth Bloch wave
$\boldsymbol{k}^{(j)}$	wavevector of the jth Bloch wave
$k_z^{(j)}$	component of $\boldsymbol{k}^{(j)}$ along normal to crystal entrance surface
$k_t^{(j)}$	component of $\boldsymbol{k}^{(j)}$ in the plane of the entrance surface
$\alpha^{(j)}$	excitation amplitude of the jth Bloch wave
$C_g^{(j)}$	the gth coefficient of the jth Bloch wave
$\Psi(\boldsymbol{r})$	the total wavefunction
v_g	amplitude of gth diffracted beam
I_g	intensity of gth diffracted beam
$\boldsymbol{A}$	the 'secular matrix' (equation (4.43))
$\boldsymbol{C}$	the eigenvector matrix
$\mathrm{i}\boldsymbol{q}^{(j)}$	imaginary part of the wavevector of the jth Bloch wave
$\kappa^{(j)}$	amplitude absorption coefficient of jth Bloch wave
κ_0	mean amplitude absorption coefficient
μ_0	mean intensity absorption coefficient
ξ_0'	mean absorption length
ξ_g'	anomalous absorption length
$\boldsymbol{R}(\boldsymbol{r}_j)$	displacement of jth atom in a deformed crystal
$\boldsymbol{b}$	Burgers vector of a dislocation.

2. Elastic and inelastic scattering by a single atom

2.1. Elastic scattering

We define elastic scattering by an atom (or a crystal) as a process which does not change the state of the atom (or crystal). An inelastic scattering process, on the other hand, is one in which the state of the atom is changed by the interaction, i.e. the atom is excited or de-excited. The purpose of §2 is to give a brief résumé of scattering by an atom in order to introduce some concepts which will be useful when considering scattering by crystals.

The problem of the collision between an electron and an atom is a many-body problem. However, to a good approximation, particularly in the scattering of fast electrons, the problem may be treated as the scattering of the incident electron by the potential field of the atom (see, for example, Wu and Ohmura 1962, Mott and Massey 1965). The problem of the elastic scattering of a fast electron by an atom is therefore that of solving the Schrödinger equation for the atomic potential $V(\boldsymbol{r})$. It is convenient to write the Schrödinger equation in the form

$$\nabla^2\psi(\boldsymbol{r})+\frac{8\pi^2me}{h^2}\left[E+V(\boldsymbol{r})\right]\psi(\boldsymbol{r})=0 \tag{2.1}$$

where E is the incident electron accelerating potential and $e=|e|=$the magnitude

of the electron charge. $V(\boldsymbol{r})$ is the atomic potential, defined as being intrinsically positive since the incident electron is attracted by the atom (hence eE and $eV(\boldsymbol{r})$ are the total energy and the potential energy, respectively, of the incident electron). It is convenient to gather together the constants in equation (2.1) by setting

$$k^2=\frac{1}{\lambda^2}=\frac{2meE}{h^2} \qquad U(\boldsymbol{r})=\frac{2me}{h^2}V(\boldsymbol{r}) \tag{2.2}$$

so that the Schrödinger equation becomes

$$\nabla^2\psi+4\pi^2[k^2+U(\boldsymbol{r})]\psi=0. \tag{2.3}$$

As is usual in a scattering experiment we assume that the point of observation of the scattered wave is at a distance from the atom which is large compared with the dimensions of the scattering field. If the incident electron is the plane wave $\exp(2\pi ikz)$ then the asymptotic form of the wavefunction ψ in equation (2.3) must be of the form:

$$\psi=\exp(2\pi ikz)+f(\theta)\frac{\exp(2\pi ikr)}{r}. \tag{2.4}$$

In equation (2.4) the first term represents the electron wave incident upon the atom and the second term the scattered wave. The angle between the incident beam and the scattered beam is 2θ. If the atom were a point (that is, if the atomic dimensions were very much less than the incident electron wavelength) then the scattered wave would be a pure spherical wave $\exp(2\pi ikr)/r$. This is the case, for example, in the scattering of slow neutrons by the nucleus, in which the 'interaction distance' of the nuclear force is very much less than the thermal neutron wavelength. However, the incident electron beam 'sees' a finite atom and hence each point of the scattering field radiates a spherical wave, neighbouring waves interfering to produce a total scattered wave of the form $f(\theta)\exp(2\pi ikr)/r$. $f(\theta)$ is clearly the amplitude of the scattered wave at unit distance r, and hence $f(\theta)$ is called the atomic scattering amplitude. The scattered intensity $I(\theta)$ at unit distance is then

$$I(\theta)=|f(\theta)|^2. \tag{2.5}$$

The atomic scattering amplitude $f(\theta)$ is, in general, complex. It may be calculated exactly by expanding in spherical harmonics and using partial wave scattering theory (Hoerni and Ibers 1953) which yields

$$f(\theta)=\frac{1}{4\pi ik}\sum_{l=0}^{\infty}(2l+1)[\exp(2i\eta_l)-1]P_l(\cos\theta) \tag{2.6}$$

where $P_l(\cos\theta)$ is the lth Legendre coefficient, and η_l is a constant determined by integration. The series often converges very slowly.

An alternative approach to expanding in spherical harmonics is to use the Born series method. This is particularly appropriate for the case of fast electrons and also it turns out that the expression given by the first Born approximation atomic scattering amplitude for a single atom has a special significance in the scattering of electrons by crystals (see §4.1).

The integral form of the Schrödinger equation (2.3) which has the asymptotic

solution of equation (2.4) is well known to be (e.g. Mott and Massey 1965)

$$\psi(\boldsymbol{r}) = \exp(2\pi i k z) + \pi \int \frac{\exp(ik|\boldsymbol{r}-\boldsymbol{r}'|)}{|\boldsymbol{r}-\boldsymbol{r}'|} U(\boldsymbol{r}')\psi(\boldsymbol{r}')\,\mathrm{d}\boldsymbol{r}'. \tag{2.7}$$

If the scattering is weak, i.e. the amplitude of the scattered wave is much less than the amplitude of the incident wave, we may assume as a first approximation that $\psi(\boldsymbol{r}')$ in the integral can be replaced by the incident wave amplitude $\exp(2\pi i k z')$. This approximation is known as the 'first Born approximation', or often simply just the 'Born approximation'. Successive, higher-order Born approximations may be obtained by iteration, i.e. $\psi(\boldsymbol{r}')$ in the integral is replaced by progressively better wavefunctions. The iterative procedure generates the 'Born series':

$$\psi(\boldsymbol{r}) = \exp(2\pi i k z) + \psi_1(\boldsymbol{r}) + \psi_2(\boldsymbol{r}) + \ldots \tag{2.8}$$

where $\psi_1(\boldsymbol{r})$ is the first Born approximation solution, $\psi_2(\boldsymbol{r})$ is the second Born approximation solution, and so on. If the scattering is weak so that the Born approximation procedure is valid, the Born series converges and sums to the exact result of equation (2.6) (see, for example, Schomaker and Glauber 1952, Glauber and Schomaker 1953, Gjønnes 1964).

2.2. The first Born approximation atomic scattering amplitude

Since this quantity is important in the scattering of electrons by crystals (see §4.1) we will consider it in some detail. Setting $\psi(\boldsymbol{r}') = \exp(2\pi i k z')$ in equation (2.7), assuming that the point of observation $\boldsymbol{r}$ is at a large distance relative to the dimensions of the atom, and comparing the result with equation (2.4) yields the atomic scattering amplitude on the first Born approximation as (see, for example, Hirsch *et al* 1977)

$$f^{\mathrm{B}}(\boldsymbol{K}') = \frac{2\pi me}{h^2} \int_{-\infty}^{\infty} V(\boldsymbol{r}) \exp(-2\pi i \boldsymbol{K}'.\boldsymbol{r})\,\mathrm{d}\boldsymbol{r} \tag{2.9}$$

where $V(\boldsymbol{r})$ is the atomic potential and $\boldsymbol{K}'$ is the 'scattering vector', i.e. $\boldsymbol{K}' = \boldsymbol{k}' - \boldsymbol{k}$, where $\boldsymbol{k}$ and $\boldsymbol{k}'$ are the wavevectors of the incident wave and the scattered wave, respectively (see figure 3). For elastic scattering $|\boldsymbol{k}| \simeq |\boldsymbol{k}'|$, and hence the triangle in figure 3 is isosceles. Defining the total angle of scatter as 2θ we have from figure 3:

$$K' = 2k \sin\theta = (2 \sin\theta)/\lambda. \tag{2.10}$$

Equation (2.9) shows that the Born approximation atomic scattering amplitude for electrons is proportional to the Fourier transform of the atomic potential. The analogy with optical and x-ray diffraction is clear. In optics the Fraunhofer diffracted amplitude of an object is equal to the Fourier transform of the transmission function of the object. In x-ray diffraction, the atomic scattering factor is equal to the Fourier transform of the electron charge density. Thus the Fourier transform concept is a unifying concept in diffraction theory. However, it is important to realise the limitation of Fourier transform methods in diffraction. The first Born approximation, leading to the Fourier transform in equation (2.9), is a single scattering approximation for a weakly scattering object. This approximation is essentially identical to the approximation made in optics in deriving the Fourier transform relationship for Fraunhofer diffraction. However, whereas this weak scattering approximation

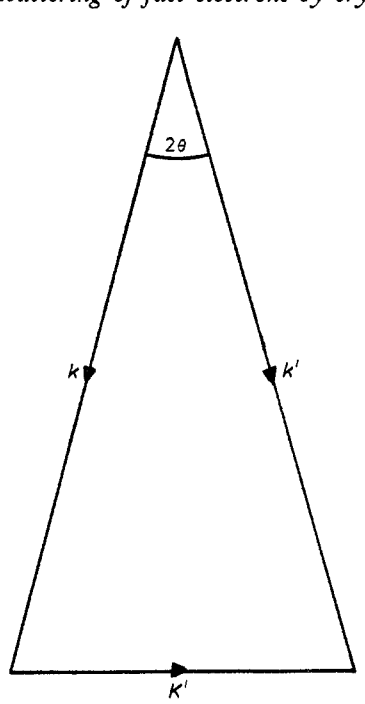

Figure 3. Diagram illustrating scattering from an incident beam of wavevector $\boldsymbol{k}$ to a scattered beam of wavevector $\boldsymbol{k}'$. $\boldsymbol{K}'$ is the 'scattering vector' and the scattering angle is defined as 2θ.

is usually valid in optics, it breaks down completely in the scattering of fast electrons by crystals, which are strongly scattering objects for which a more complex theory is necessary (see §4.2). However, provided the scattering is weak (as in the scattering of fast electrons by light atoms) the first Born approximation is very useful.

The atomic potential $V(\boldsymbol{r})$ is related to another important physical property, the charge density, by Poisson's equation:

$$\nabla^2 V(\boldsymbol{r}) = -4\pi e[\rho_n(\boldsymbol{r}) - \rho_e(\boldsymbol{r})] \tag{2.11}$$

where $\rho_n(\boldsymbol{r})$ is the charge density of the atomic nucleus and $\rho_e(\boldsymbol{r})$ is that of the atomic electrons. To a good approximation for a static atom we may take $\rho_n(\boldsymbol{r})$ to be a point charge at the origin $r=0$, of strength Z, the atomic number.

Equation (2.9) may be written as

$$f^B(\boldsymbol{K}') = -\frac{me}{2\pi h^2 K'^2}\int_{-\infty}^{\infty} V(\boldsymbol{r})\nabla^2 \exp(-2\pi i\boldsymbol{K}'.\boldsymbol{r})\,d\boldsymbol{r}. \tag{2.12}$$

Integrating the above by parts yields, since $V(\infty)=V(-\infty)=0$:

$$f^B(\boldsymbol{K}') = -\frac{me}{2\pi h^2 K'^2}\int_{-\infty}^{\infty} \exp(-2\pi i\boldsymbol{K}'.\boldsymbol{r})\nabla^2 V(\boldsymbol{r})\,d\boldsymbol{r} \tag{2.13}$$

Substituting equation (2.11) into (2.13):

$$\begin{aligned} f^B(\boldsymbol{K}') &= \frac{2me^2}{h^2 K'^2}\int_{-\infty}^{\infty} [Z\delta(\boldsymbol{r}) - \rho_e(\boldsymbol{r})] \exp(-2\pi i\boldsymbol{K}'.\boldsymbol{r})\,d\boldsymbol{r} \\ &= \frac{2me^2}{h^2 K'^2}[Z - f^x(\boldsymbol{K}')] \end{aligned} \tag{2.14}$$

where f^x is the atomic scattering factor for x-rays. Equation (2.14), the Mott formula (Mott 1930), directly relates the electron and x-ray atomic scattering factors. The first term in the bracket of equation (2.14) is due to Rutherford scattering by the nucleus, and the second term is due to scattering by the atomic electrons.

For large-angle scattering $f^x(\boldsymbol{K}')$ tends to zero and from equation (2.14)

$$I(\theta)_{\theta\to 90^\circ} = |f(\theta)|^2_{\theta\to 90^\circ} = \frac{4m^2e^4}{\hbar^4 K'^4} Z^2. \tag{2.15}$$

Equation (2.15), the Rutherford scattering equation, only takes into account scattering by the nucleus and not by the atomic electrons, and hence it is only valid for large scattering angles for which $f^x(\boldsymbol{K}')$ is negligibly small.

$f(\boldsymbol{K}')$ is in fact sharply peaked in the forward direction for fast electrons as may be deduced from the useful 'bandwidth' theorem of Fourier transforms which, applied to equation (2.12), states that

$$\Delta K' \Delta r \simeq 1 \tag{2.16}$$

where $\Delta K'$ represents the range of K' values over which $f^B(\boldsymbol{K}')$ is large, and Δr represents the range of r values over which $V(\boldsymbol{r})$ is large. Now the atomic radius is of the order of 1 Å, and hence $\Delta r \sim 1$ Å. Therefore:

$$\Delta K' \sim 1 \text{ Å}^{-1}$$

and

$$\Delta[(\sin\theta)/\lambda] \sim 0{\cdot}5 \text{ Å}^{-1}.$$

For 100 keV electrons, $\lambda = 0{\cdot}037$ Å. Therefore:

$$\Delta(\sin\theta) \sim \Delta\theta \simeq 0{\cdot}02 \text{ rad} \simeq 1^\circ. \tag{2.17}$$

Hence $f^B(\boldsymbol{K}')$ is sharply peaked in the forward direction and the curve of $f^B(\boldsymbol{K}')$ against θ has a semi-half-peak width of about 1° for 100 keV electrons (see figure 4).

The magnitude of $f^B(\boldsymbol{K}')$ is typically between 1–10 Å. This is very much greater than the scattering length b for neutrons ($\sim 10^{-4}$ Å) or the corresponding scattering amplitude for x-rays, $r_e f^x$($\sim 10^{-4}$ Å), where r_e is the classical electron radius which is the scaling factor necessary in order to compare the magnitude of x-ray and electron scattering (see, for example, James 1967). Hence electrons are elastically scattered by atoms very much more strongly than are x-rays or neutrons.

2.3. The total elastic scattering cross section

The total elastic scattering cross section for a fast electron incident on a single atom is, from equation (2.5),

$$\sigma = \int I \, d\Omega = \int |f(\theta)|^2 \, d\Omega. \tag{2.18}$$

It is useful to have an approximate analytical expression for σ. Two different treatments of this problem yield a similar result:

$$\sigma = \frac{A\lambda^2 Z^{4/3}}{\pi(1 - v^2/c^2)} \tag{2.19}$$

where $(1 - v^2/c^2)$ is a relativistic correction factor (see §4.8), v is the incident electron velocity and c is the velocity of light. Using the Wentzel (1927) model for the atom, Lenz (1954) gives $A = 1$ in equation (2.19). Using the Thomas–Fermi statistical

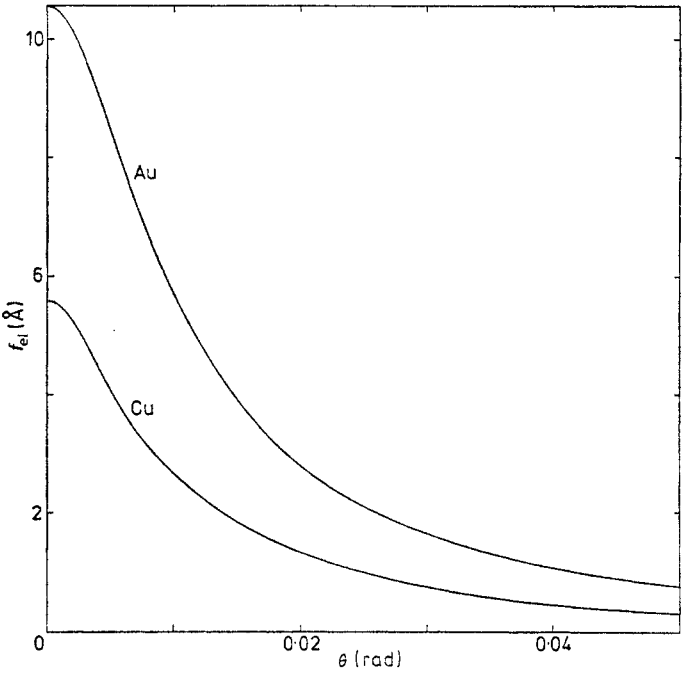

Figure 4. The first Born approximation scattering amplitude, $f^B(\boldsymbol{K}')$, as a function of θ for 100 keV electrons incident upon single atoms of gold and copper. The plots have been made using the relativistic Hartree–Fock scattering amplitudes of Doyle and Turner (1968).

model of the atom, Mott and Massey (1965) give $A = 1 \cdot 8$. More accurate computations of the first Born approximation cross section using different atomic models have been made by Langmore *et al* (1973) and Humphreys *et al* (1974). The results of Humphreys *et al*, using relativistic Hartree–Fock wavefunctions for the atoms (Doyle and Turner 1968), which are probably the most accurate wavefunctions currently available, are shown in figure 5. Electron shell effects are clearly evident in the accurate cross sections and equation (2.19) is seen to be a considerable oversimplification. However, equation (2.19) is evidently valid for approximate semiquantitative estimates. In particular, the Z^2 dependence of the cross section on the Rutherford model is replaced by an approximately $Z^{4/3}$ dependence of the cross section when scattering by both the nucleus and the atomic electrons is taken into account.

Finally it should be noticed that the first Born approximation gives f^B as a real quantity (e.g. see equation (2.14)). This is an important point in the scattering of electrons by crystals (see §4.1). The exact treatment for single atoms, equation (2.6), yields that f is a complex quantity, as does using higher-order Born approximations, of the form $|f| \exp(i\eta)$. The phase shift η is appreciable for heavy atoms and it must be taken into account in gas diffraction studies (Hoerni and Ibers 1953, Ibers and Hoerni 1954).

2.4. Inelastic scattering

The major inelastic scattering mechanism for fast incident electrons with energies in the range 1 keV to 10 MeV is single-electron excitation of the atomic electrons.

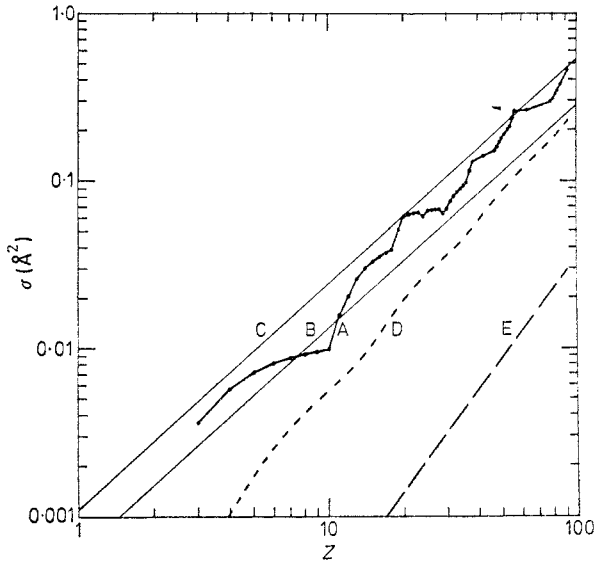

Figure 5. The elastic scattering cross section against atomic number (on a log–log scale) for 100 keV electrons incident upon single atoms. A, B and C plot the total elastic cross section using relativistic Hartree–Fock wavefunctions, Wentzel potentials and Thomas–Fermi potentials, respectively. D and E plot the cross section for scattering between $\theta = \theta(\text{min})$ and $\frac{1}{2}\pi$. In D, $\theta(\text{min}) = 0{\cdot}024$ rad; in E, $\theta(\text{min}) = 0{\cdot}15$ rad, and σ varies as Z^2 (Rutherford scattering), as expected when the small-angle scattering is not taken into account (from Humphreys *et al* (1974), by courtesy of the Australian Academy of Sciences).

This may take two forms, excitation of atomic electrons to higher bound atomic states and excitation to a positive total energy state, i.e. ionisation of the atom.

For simplicity we again use the first Born approximation as a reasonable first approximation for the scattering of a fast electron by an atom. The first Born approximation differential cross section for scattering by an atom initially in the ground state 0 and finally in the nth excited state (Born 1926) may be written in the form:

$$\frac{\mathrm{d}\sigma_{0n}}{\mathrm{d}\Omega} = \frac{4m^2e^4|Z\delta_{0n} - f_{0n}^{\mathrm{x}}|^2}{h^4K'^4}\frac{k'}{k} \tag{2.20}$$

where, as before, k and k' are the magnitudes of the fast electron wavevector before and after scattering respectively, $\boldsymbol{K}' = \boldsymbol{k}' - \boldsymbol{k}$, and Z is the atomic number of the scattering atom; $\delta_{0n} = 1$ for elastic scattering, $\delta_{0n} = 0$ for inelastic scattering. $f_{0n}^{\mathrm{x}}(\boldsymbol{K}')$ is a generalised atomic form factor (or atomic scattering factor) for x-rays defined by

$$f_{0n}^{\mathrm{x}}(\boldsymbol{K}') = \int_{-\infty}^{\infty} u_0(\boldsymbol{r})u_n^*(\boldsymbol{r}) \exp(-2\pi\mathrm{i}\boldsymbol{K}'.\boldsymbol{r})\,\mathrm{d}\boldsymbol{r} \tag{2.21}$$

where u_0 and u_n are the ground-state and nth excited-state wavefunctions (including position and spin) of the atom. For elastic scattering, equation (2.20) clearly reduces to equation (2.14) using equation (2.18), since $f_{0n}^{\mathrm{x}}(\boldsymbol{K}') \to f_{00}^{\mathrm{x}}(\boldsymbol{K}') = f^{\mathrm{x}}(\boldsymbol{K}')$. Detailed exact evaluations of equation (2.20) have not yet been made, but a number of approximate calculations have been performed. Usually, following Morse (1932), the wavelength change on scattering is neglected. Equation (2.20) may then be

summed over all excited states, taking into account the exclusion principle, to give the differential cross section for all inelastic scattering transitions:

$$\frac{\mathrm{d}\sigma_{\mathrm{inel}}}{\mathrm{d}\Omega}=\frac{4m^2e^4S(\boldsymbol{K}')}{h^4K'^4} \tag{2.22}$$

where $S(\boldsymbol{K}')$ is an inelastic scattering function, which may be evaluated using various atomic models. In the Hartree–Fock representation, $S(\boldsymbol{K}')$ is given by

$$S(\boldsymbol{K}')=Z-\sum_i |f_{ii}^{\mathrm{x}}(\boldsymbol{K}')|^2-\sum_{i\neq j} |f_{ij}^{\mathrm{x}}(\boldsymbol{K}')|^2 \tag{2.23}$$

where $f_{ij}^{\mathrm{x}}(\boldsymbol{K}')$ is given by equation (2.21). The summation over i is taken over the occupied levels only, and the third term is the exchange term (due to the exclusion principle, transitions to occupied states are forbidden). The terms $f_{ij}^{\mathrm{x}}(\boldsymbol{K}')$ have been computed from Hartree–Fock wavefunctions for a number of elements by Freeman (1959, 1960). Calculations using the above method but neglecting exchange have been made by Whelan (1965) and Radi (1970). However the effect of the exchange term is likely to be important (Pogany 1971), as are also electron correlation effects (i.e. deviations from the Hartree–Fock theory), and for very small angle scattering equation (2.22) breaks down. Further work is needed in this area.

The angular distribution of the inelastically scattered electrons may be estimated using equations (2.22) and (2.23), and it is found that the inelastically scattered electrons are very sharply peaked in the forward direction. 100 keV incident electrons typically have a semi-half-peak width after inelastic scattering of about 10^{-4} rad, and the total cross section for inelastic scattering varies approximately as $Z^{1/3}$ (Lenz 1954).

2.5. The imaging of single atoms

Figure 4 shows that the inelastically scattered electrons are much more sharply peaked in the forward direction than the elastically scattered electrons. This fact was utilised by Crewe *et al* (1970) in order to detect single heavy atoms supported on a thin carbon substrate. Figure 6 shows schematically the experimental arrangement. Electrons are focused to a very small spot (~5 Å diameter) and transmitted through the thin carbon substrate upon which rest the single heavy atoms. If the incident beam convergence angle is appropriately chosen, most of the inelastically scattered electrons fall within the incident beam cone, and most of the elastically scattered electrons fall

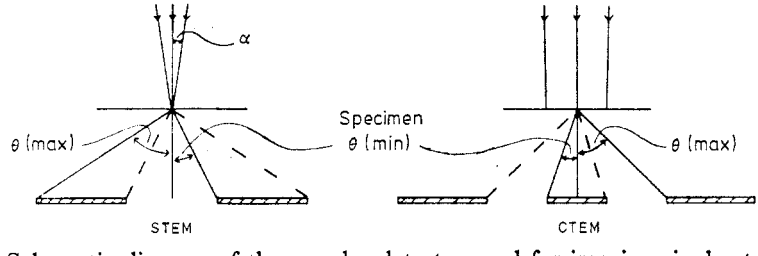

Figure 6. Schematic diagram of the annular detector used for imaging single atoms in STEM (scanning transmission electron microscopy). An alternative dark-field method for CTEM (conventional transmission electron microscopy) is also shown (from Humphreys *et al* (1974), courtesy of the Australian Academy of Science).

outside the beam cone and can be collected on an annular detector as shown. From equation (2.19), the total elastically scattered intensity is approximately proportional to $Z^{4/3}$. Hence, if the incident beam is scanned across the carbon surface the ratio of the elastically scattered intensity when the beam is scattered by the (heavy atom + carbon substrate) relative to that when the beam is scattered by the carbon substrate alone is

$$\frac{I(\mathrm{C+atom})}{I(\mathrm{C})}=1+\frac{1}{n_c}\left(\frac{Z(\mathrm{atom})}{Z(\mathrm{C})}\right)^{4/3} \tag{2.24}$$

where n_c is the number of carbon atoms in the path of the beam. For example, if $n_c=100$ and the heavy atom is uranium, equation (2.24) yields $I(\mathrm{C+atom})/I(\mathrm{C})=1{\cdot}3$, i.e. there should be 30% contrast from the single uranium atom, which is readily detectable in the Crewe scanning transmission electron microscope (STEM). For further details the reader is referred to Crewe *et al* (1970). An example of the heavy atom images obtained is shown in figure 1. Single heavy atoms have also been detected in a conventional transmission electron microscope (Hashimoto *et al* 1971, Formanek *et al* 1971, Henkelman and Ottensmeyer 1971).

The individual heavy atoms diffuse across the substrate surface at room temperature by thermal motion. Hence, unfortunately, this technique has not yet been used to determine the positions of atoms in a heavy-atom-substituted DNA molecule, for example. However, work is in progress to observe the specimen in a liquid-helium-cooled stage, which may make such experiments possible. The distribution and diffusion at room temperature of individual heavy atoms on thin film substrates has recently been studied (Isaacson *et al* 1977) using the high resolution STEM of Crewe.

3. The geometry of diffraction by perfect crystals

3.1. Introduction

In §2 we have seen that a single atom scatters an incident electron beam in all directions, the scattering being strongly peaked in the forward direction. A perfect crystal is a periodic array of atoms. The scattered waves from one atom interfere with scattered waves from other atoms in the crystal, this interference redistributing the scattered amplitude and yielding directions in which the scattered intensity is a maximum, due to constructive interference, or a minimum, due to destructive interference. Usually the directions of diffracted maxima are given by geometrical considerations only (i.e. that path differences should be a whole number of wavelengths). Hence the basic geometry of the diffraction by crystals of any incident wave (electron, x-ray, neutron, etc) is essentially the same. Some specific features of the diffraction of electrons will be discussed in §§3.6 and 3.7.

3.2. The Bragg law

The simplest statement of the condition for a diffracted maximum is the well-known Bragg equation (Bragg 1913)

$$2\,d'\sin\theta=n\lambda \tag{3.1}$$

where d' is the spacing between lattice planes and n is an integer. The particular

angle θ satisfying equation (3.1) is known as the Bragg angle (often denoted by θ_B).

It is conventional and convenient to put $d = d'/n$, so that equation (3.1) is

$$2\,d \sin\theta = \lambda. \tag{3.2}$$

Thus, although the diffracted beam may arise from an nth-order reflection from actual lattice planes of spacing d', it is convenient to regard this as a first-order reflection from planes of spacing $d = d'/n$, which may be real or fictitious lattice planes.

Bragg arrived at his concept of a 'reflection', in the optical sense, of x-rays from planes of atoms by applying Huygens' principle to an array of atoms lying in a plane, and showing that the secondary waves from each atom build up a wavefront exactly as if part of the incident wave had been specularly reflected from the plane, provided that the angle of incidence satisfies equation (3.2).

3.3. The Laue condition

von Laue (see Friedrich *et al* 1912) considered the problem of the geometry of diffraction by crystals slightly in advance of the work of Bragg. Considering the scattering of waves by the individual unit cells of the crystal, rather than by lattice planes, he derived the well-known 'Laue condition' for a diffracted maximum, that

$$\boldsymbol{k}' - \boldsymbol{k} = \boldsymbol{g} \tag{3.3}$$

where $\boldsymbol{k}'$ and $\boldsymbol{k}$ are the wavevectors of the scattered and incident waves, respectively, and $\boldsymbol{g}$ is a reciprocal lattice vector. For elastic scattering $|\boldsymbol{k}'| = |\boldsymbol{k}|$, hence equation (3.3) defines an isosceles triangle and, given that $|\boldsymbol{g}| = 1/d$, Bragg's law follows immediately. Thus Bragg's law and the Laue condition are entirely equivalent, being real-space and reciprocal-space formulations, respectively, of the geometry of diffraction.

The physical significance of the Laue condition can be seen by forming the scalar product of equation (3.3) with $\boldsymbol{a}$, $\boldsymbol{b}$ and $\boldsymbol{c}$ successively (where $\boldsymbol{a}$, $\boldsymbol{b}$ and $\boldsymbol{c}$ are the lattice translation vectors) which yields:

$$\begin{aligned} \boldsymbol{a}.(\boldsymbol{k}' - \boldsymbol{k}) &= \boldsymbol{a}.\boldsymbol{g} = n_1 \\ \boldsymbol{b}.(\boldsymbol{k}' - \boldsymbol{k}) &= n_2 \\ \boldsymbol{c}.(\boldsymbol{k}' - \boldsymbol{k}) &= n_3 \end{aligned} \tag{3.4}$$

where n_1, n_2 and n_3 are integers. Equations (3.4) are known as the three Laue equations for diffraction, which must all be satisfied simultaneously for a maximum to occur.

Each of the three equations (3.4) is the condition for a diffracted maximum from a one-dimensional grating of spacing $\boldsymbol{a}$, $\boldsymbol{b}$ and $\boldsymbol{c}$, respectively. For any given angle of incidence corresponding to $\boldsymbol{k}$ a diffracted maximum always occurs in a one-dimensional grating in a direction corresponding to $\boldsymbol{k}'$ given by one of the equations (3.4). However, for a crystal the conditions for a diffracted maximum are much more stringent since all three equations (3.4) must be satisfied simultaneously. The geometry of diffraction by a three-dimensional crystal is equivalent

to simultaneous diffraction by three one-dimensional gratings of spacing $\boldsymbol{a}$, $\boldsymbol{b}$ and $\boldsymbol{c}$, each grating being parallel to $\boldsymbol{a}$, $\boldsymbol{b}$ and $\boldsymbol{c}$, respectively.

The Laue condition $(\boldsymbol{k}'-\boldsymbol{k})=\boldsymbol{g}$, or the equivalent Bragg law, is a necessary but not a sufficient condition for a diffracted maximum. The Laue condition is derived by considering scattering by a periodic array of unit cells. For a non-zero diffracted amplitude it is clearly also necessary that the amplitude scattered by one unit cell, the structure amplitude to be defined in equation (3.5), is non-zero. Thus there are two geometrical conditions for a non-zero reflection:

(i) The Laue condition: $(\boldsymbol{k}'-\boldsymbol{k})=\boldsymbol{g}$.

(ii) A non-zero structure amplitude: $F_g \neq 0$.

The above two conditions are usually necessary and sufficient for a diffracted maximum although the effects of dynamical diffraction (see §4), in particular extinction and the critical voltage effect (§5.9), can impose additional conditions.

3.4. The Ewald sphere (or reflecting sphere) construction

This is a very useful geometrical interpretation made by Ewald (1913) of the Laue condition $\boldsymbol{k}'-\boldsymbol{k}=\boldsymbol{g}$. The steps in the construction are as follows (and see figure 7(*a*)):

(*a*) Plot the reciprocal lattice of the crystal.

(*b*) Choose any reciprocal lattice point as origin O and draw a line CO parallel to $\boldsymbol{k}$, the incident beam direction and of magnitude $|\boldsymbol{k}|$.

(*c*) Draw a sphere centre C, radius $|\boldsymbol{k}|$.

If the sphere intersects a reciprocal lattice point G at distance $\boldsymbol{g}$ from the origin O, then a diffracted beam occurs (provided $F_g \neq 0$) and the direction of the diffracted beam is $\mathrm{CG}=\boldsymbol{k}'$. The proof of the construction follows immediately from the geometry of the situation. If G lies on the sphere then $(\boldsymbol{k}'-\boldsymbol{k})=\boldsymbol{g}$, as required.

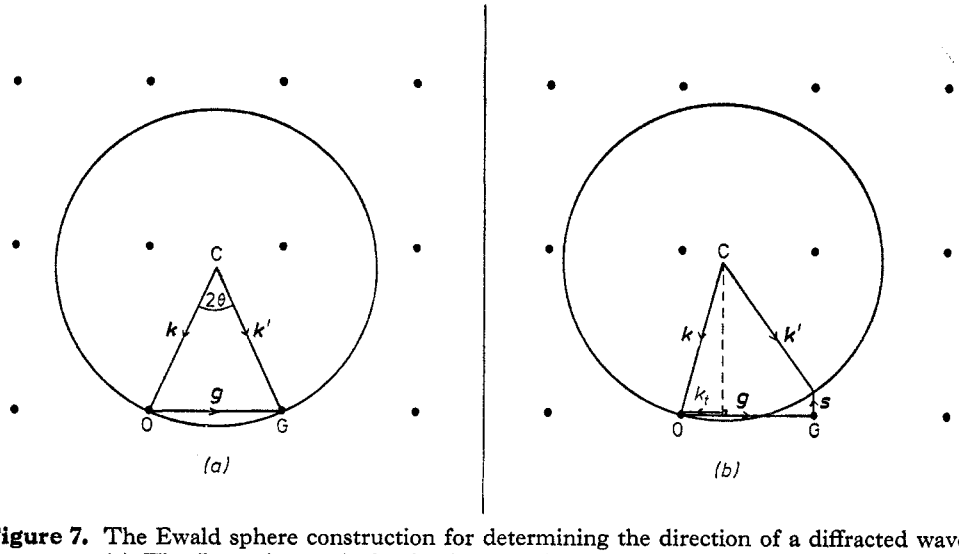

Figure 7. The Ewald sphere construction for determining the direction of a diffracted wave. (*a*) The Laue (or equivalently the Bragg) condition is exactly satisfied. (*b*) The crystal is slightly deviated from the exact Laue (or Bragg) condition. The deviation is indicated by s. s is defined to be negative when the reciprocal lattice point is outside the sphere, as in this figure. k_t is the component of $\boldsymbol{k}$ along $\boldsymbol{g}$.

3.5. Kinematical theory of diffraction by finite perfect crystals

The Ewald sphere construction considers a sphere exactly intersecting a point. This corresponds to the Laue condition, or equivalently Bragg's law, being exactly satisfied. Physically this corresponds to complete destructive interference in all other directions. Such complete interference can only occur in the limit of an infinite number of unit cells, i.e. for an infinite crystal (which is also perfect and in which no inelastic scattering is allowed).

For a finite crystal there will be only partially destructive interference and hence there will be a finite non-zero diffracted intensity in directions other than exact Bragg reflection directions. For finite crystals, as used in practice, it is therefore necessary to give a more careful treatment of the geometry of diffraction. It must be emphasised that in the following treatment we are concerned with the geometry of diffraction, and not with accurate diffracted intensities. We shall assume the crystal to be a weakly scattering object (the kinematical approximation), which is approximately valid as regards the geometry of diffraction, but which is invalid as regards the intensities of electrons diffracted by crystals, apart from special cases (see §4).

We define the structure amplitude $F(\boldsymbol{g})$ as the amplitude scattered by a unit cell at unit distance in the direction $(\boldsymbol{k}+\boldsymbol{g})$, i.e. the defining equation is (e.g. Hirsch *et al* 1977)

$$F(\boldsymbol{g}) = \sum_i f_i^{\mathrm{B}}(\boldsymbol{g}) \exp(-2\pi i \boldsymbol{g}.\boldsymbol{r}_i) \tag{3.5}$$

where $\boldsymbol{r}_i$ is the position of the ith atom in the unit cell having an atomic scattering amplitude $f_i^{\mathrm{B}}(\boldsymbol{g})$ given by equation (2.9). The use of the first Born approximation atomic scattering amplitude here is discussed in §4.1. Equation (3.5) represents scattering by all the atoms in the unit cell taking into account the phase difference for scattering in a direction $(\boldsymbol{k}+\boldsymbol{g})$, where $\boldsymbol{k}$ is the incident wavevector. The minus sign in the exponential of equation (3.5) is consistent with our choice of representing a plane wave travelling in the positive $\boldsymbol{k}$ direction as $\exp(+2\pi i \boldsymbol{k}.\boldsymbol{r})$ (see §1.3).

Consider two unit cells within the crystal, at O and P, separated by $\boldsymbol{r}_j$. From simple geometry (see figure 8) the phase difference between waves scattered at O and at P is $-2\pi \boldsymbol{r}_j.(\boldsymbol{k}'-\boldsymbol{k})$. If the crystal is at an exact Bragg position, $\boldsymbol{k}'-\boldsymbol{k}=\boldsymbol{g}$. Consider the crystal slightly deviated from the Bragg position so that

$$\boldsymbol{k}'-\boldsymbol{k}=\boldsymbol{g}+\boldsymbol{s} \tag{3.6}$$

where $\boldsymbol{s}$ is a small vector in reciprocal space indicating the deviation from the exact Laue condition (see figure 7(*b*)). The deviation parameter $\boldsymbol{s}$ is defined as negative when the reciprocal lattice point is outside the Ewald sphere, as in figure 7(*b*) and $\boldsymbol{s}$ is positive if the reciprocal lattice point is inside the sphere. The total amplitude scattered by the crystal in the direction $\boldsymbol{k}'=(\boldsymbol{k}+\boldsymbol{g}+\boldsymbol{s})$ to a point at a large distance $\boldsymbol{r}$ is

$$\begin{aligned} A(\boldsymbol{s}) &= r^{-1}F_g \sum_j \exp[-2\pi i \boldsymbol{r}_j.(\boldsymbol{g}+\boldsymbol{s})] \\ &= r^{-1}F_g \sum_j \exp(-2\pi i \boldsymbol{r}_j.\boldsymbol{s}) \end{aligned} \tag{3.7}$$

since $\boldsymbol{r}_j.\boldsymbol{g}$ is an integer. The summation is taken over all unit cells of the crystal. The r^{-1} factor in equation (3.7) is frequently omitted in textbooks, which gives rise to a considerable apparent simplification of the kinematical theory. However,

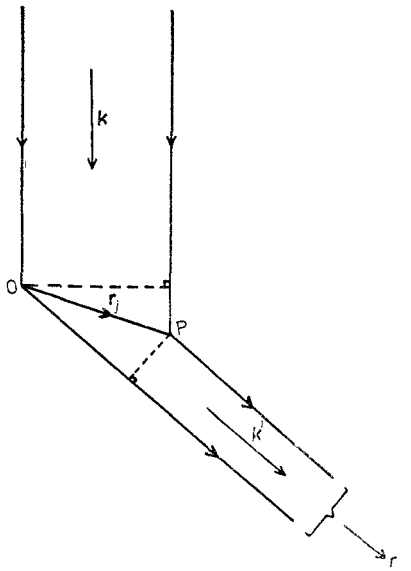

Figure 8. Diagram illustrating the diffraction of an incident wave of vector $\boldsymbol{k}$ to a point $\boldsymbol{r}$ at large distance in the direction $\boldsymbol{k}'$, by two unit cells at O and P separated by $\boldsymbol{r}_j$.

it is important to leave in the r^{-1} factor in order to show how the spherical-type wave of equation (3.7) finally yields a plane-type total Bragg scattered wave from a crystal. The r^{-1} factor arises in the same way as in equation (2.4) and $\boldsymbol{r}$ is assumed to be large by comparison with the crystal dimensions.

For simplicity, consider scattering by a rectangular parallelepiped crystal. Let the unit cell have sides $\boldsymbol{a}$, $\boldsymbol{b}$ and $\boldsymbol{c}$ and let the crystal dimensions be A, B and C parallel to the unit cell sides, respectively. We may write

$$\boldsymbol{r}_j = u\boldsymbol{a} + v\boldsymbol{b} + w\boldsymbol{c} \tag{3.8}$$

where u, v and w are integers. Let $\boldsymbol{s}$ have components s_a, s_b and s_c so that

$$\boldsymbol{s} = s_a\hat{\boldsymbol{a}}^* + s_b\hat{\boldsymbol{b}}^* + s_c\hat{\boldsymbol{c}}^* \tag{3.9}$$

where $\hat{\boldsymbol{a}}^*$, $\hat{\boldsymbol{b}}^*$ and $\hat{\boldsymbol{c}}^*$ are reciprocal lattice unit vectors. Then

$$A(\boldsymbol{s}) = r^{-1}F_g \sum_u \sum_v \sum_w \exp\left[-2\pi i(uas_a + vbs_b + wcs_c)\right]. \tag{3.10}$$

It is convenient to choose the origin at the centre of the crystal. $\Sigma_u \exp(-2\pi i u a s_a)$ is a standard progression which sums to give

$$\sum_u \exp(-2\pi i\, uas_s) = \frac{\sin \pi N_1 a s_a}{\sin \pi a s_a} \tag{3.11}$$

where N_1 is the number of unit cells along the A dimension, i.e. $N_1 a = A$. Since we are considering small deviations from the Bragg position, s_a is small and $\sin \pi a s_a \approx \pi a s_a$. Hence from (3.10) and (3.11) the intensity scattered in the direction

$(\boldsymbol{k}+\boldsymbol{g}+\boldsymbol{s})$, at a large distance r, is

$$I(s)=A(s)A^*(s)=\frac{F_g^2}{r^2}\frac{\sin^2\pi As_a}{(\pi as_a)^2}\frac{\sin^2\pi Bs_b}{(\pi bs_b)^2}\frac{\sin^2\pi Cs_c}{(\pi cs_c)^2}$$

$$=\left(\frac{F_g}{r^2V_{\text{cell}}}\right)^2\left(\frac{\sin\pi As_a}{\pi s_a}\right)^2\left(\frac{\sin\pi Bs_b}{\pi s_b}\right)^2\left(\frac{\sin\pi Cs_c}{\pi s_c}\right)^2 \qquad (3.12)$$

where V_{cell} is the volume of the unit cell. Equation (3.12) was first derived by von Laue (see Friedrich *et al* 1912) and is known as the Laue interference function. In going from equation (3.11) to (3.12) we considered $\boldsymbol{s}$ to be small. Physically this means that the phase angle $(2\pi\boldsymbol{r}_j.\boldsymbol{s})$ in equation (3.7) varies slowly from cell to cell and we may therefore approximate the summation in equation (3.7) to an integral so that

$$A(s)=r^{-1}F_g\sum_j\exp\left(-2\pi i\boldsymbol{r}_j.\boldsymbol{s}\right)=\frac{F_g}{V_{\text{cell}}r}\int_{\text{crystal}}\exp\left(-2\pi i\boldsymbol{r}.\boldsymbol{s}\right)\mathrm{d}\boldsymbol{r}. \qquad (3.13)$$

Evaluating the integral in equation (3.13) yields equation (3.12). Equation (3.13) states that the amplitude diffracted from a perfect crystal is proportional to the Fourier transform of a function which is unity inside the crystal and zero outside. This is called the shape transform of the crystal. Although proved here for the case of a rectangular parallelepiped crystal, the result holds generally for a crystal of any shape, on the kinematical theory. Each term in equation (3.12) is analogous to the Fraunhofer intensity diffracted by a single slit, of width A, B or C, in optics.

There is therefore a complete analogy between the kinematical theory of the diffraction of electrons (or x-rays, neutrons, etc) by a crystal, and the diffraction of light by three diffraction gratings (the three gratings being mutually perpendicular if the crystal axes are mutually perpendicular). The directions of the diffracted maxima are determined by the lattice vectors or, by analogy, by the grating spacings $\boldsymbol{a}$, $\boldsymbol{b}$ and $\boldsymbol{c}$ (equation (3.4)). The intensity distribution of each diffracted beam, or each order of diffraction, is determined by the dimensions of the crystal or, by analogy, by the dimensions of the gratings A, B and C (equation (3.12)).

The above description of the geometry of diffraction by finite crystals applies to any incident radiation (electrons, x-rays, neutrons, etc). Equation (3.13) shows that we may consider each reciprocal lattice point associated with a finite crystal to have a finite extension in reciprocal space given by the amplitude distribution $A(\boldsymbol{s})$. In x-ray diffraction this broadening is known as particle-size broadening, and the measured widths of diffracted beams may be used to determine the crystal dimensions A, B and C (see, for example, James 1967).

3.6. Kinematical diffraction by thin crystals

In transmission electron diffraction the specimens studied must be very thin (typically 1000 Å thick for conventional 100 keV electron microscopy and diffraction), since the penetration of electrons through crystals is much less than that of x-rays or neutrons. The specimen is therefore approximately a thin plate, of thickness t $(=C)$ much less than its lateral dimensions A and B. The terms in equation (3.12) involving A and B tend to δ functions for large values of A and B. Hence the intensity

diffracted by a thin plate of thickness t is

$$I(\mathbf{s}) = \frac{ABF_g^2}{r^2 V_{\text{cell}}^2} \left(\frac{\sin \pi t s_c}{\pi s_c} \right)^2 \delta(s_a)\delta(s_b). \tag{3.14}$$

Equation (3.14) shows that the intensity $I(\mathbf{s})$ is spread out in the form of a spike normal to the crystal plate. This is shown schematically in figure 9, and is the well-known diffracted intensity distribution in optics of light from a slit of width t. The width, at half-height, of the spike in reciprocal space is approximately t^{-1}. We can represent this finite distribution of scattered intensity in the Ewald sphere construction (§3.4) by drawing a line of length t^{-1} through each reciprocal lattice point in a direction normal to the crystal plate (see figure 10). These extended

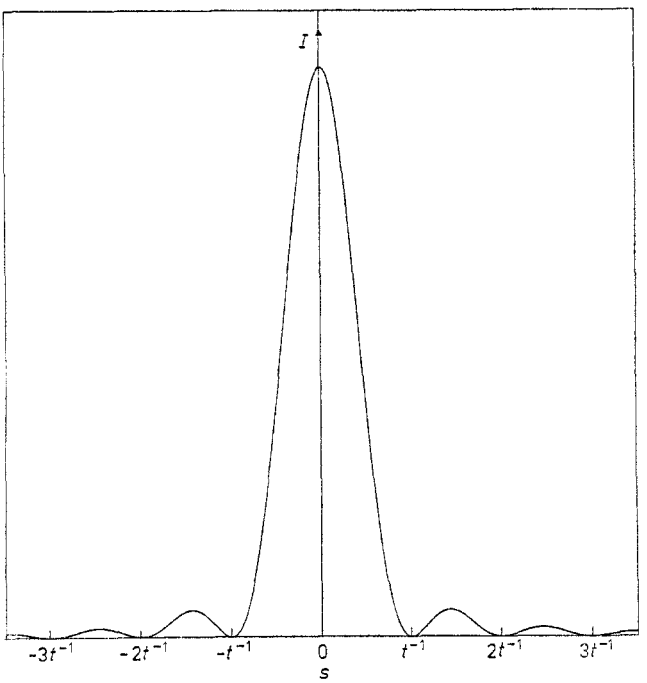

Figure 9. The intensity distribution along the spike through a reciprocal lattice point for a plate crystal of thickness t, on the kinematical theory (see equation (3.14)).

reciprocal lattice points are known as reciprocal lattice rods, or sometimes as rel-rods. On the Ewald sphere construction, the condition for reflection by a thin crystal is that a reciprocal lattice rod, rather than a point, should cut the Ewald sphere.

For low-energy electron diffraction (LEED), the incident electrons penetrate only a thin surface layer of the crystal. The effective value of t is therefore very small and each reciprocal lattice rod is very long, extending to cut the Ewald sphere twice and yielding strong diffracted beams in both forward and backward directions. Resonance effects can occur when a reciprocal lattice rod is tangent to the Ewald sphere (which has a small radius of curvature for low-energy electrons). For a detailed treatment of LEED see Pendry (1974).

We can calculate the absolute intensity, in the kinematical approximation, of the diffracted beam emerging from the crystal by using equation (3.14). For simplicity

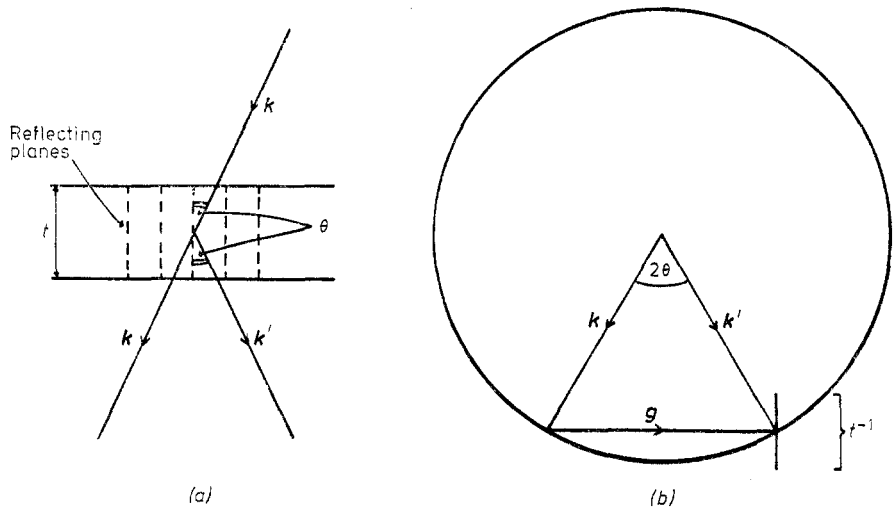

Figure 10. Diagrams illustrating the symmetrical Laue case (*a*) in real space, (*b*) in reciprocal space, for a plate crystal of thickness t. The intensity distribution along the spike in (*b*) is given in figure 9 and it has a full width at half-height (FWHH) of t^{-1} as shown.

consider the symmetrical Laue case (in which the Bragg planes are perpendicular to the crystal surface) shown in figure 10. The spike then bisects the angle 2θ between $\boldsymbol{k}$ and $\boldsymbol{k}'$ and the incident and diffracted beams enter and leave the crystal symmetrically. Consider the total intensity scattered into a solid angle $\mathrm{d}\Omega$ about the diffracted beam. In real space $r^2\,\mathrm{d}\Omega = \mathrm{d}S$, where $\mathrm{d}S$ is an area element on a plane of radius r. In reciprocal space $\mathrm{d}\Omega = \mathrm{d}s_a\,\mathrm{d}s_b/k^2\cos\theta$. Hence the total intensity scattered over the sphere of radius r about the diffracted beam direction $\boldsymbol{k}' = \boldsymbol{k}+\boldsymbol{g}$ is

$$\int I(s)\,\mathrm{d}S = \frac{ABF_g{}^2}{k^2V_{\mathrm{cell}}{}^2\cos\theta}\left(\frac{\sin\pi ts_c}{\pi s_c}\right)^2\int\delta(s_a)\,\mathrm{d}s_a\int\delta(s_b)\,\mathrm{d}s_b. \qquad (3.15)$$

Now $AB\cos\theta$ is the area of the crystal projected along $\boldsymbol{k}' = \boldsymbol{k}+\boldsymbol{g}$. Thus the intensity per unit area of the diffracted beam, i.e. the diffracted beam flux, is

$$I_g(t) = \frac{F_g{}^2(2\theta)}{k^2V_{\mathrm{cell}}{}^2\cos^2\theta}\frac{\sin^2\pi ts_c}{(\pi s_c)^2}. \qquad (3.16)$$

It is conventional to refer to $I_g(t)$ as the diffracted beam intensity, although strictly it is a flux. Also following convention we replace s_c by s, where s is the component of $\boldsymbol{s}$ normal to the crystal plate, and we define a parameter

$$\xi_g = \pi kV_{\mathrm{cell}}\cos\theta/F_g(2\theta). \qquad (3.17)$$

ξ_g has the dimensions of length and is called the extinction distance for reasons to be given in §4. Typically ξ_g is several hundred Å for 100 keV incident electrons. Equation (3.17) then gives the intensity scattered through 2θ in the gth diffracted beam from a crystal of thickness t on the kinematical theory as

$$I_g(t) = \left(\frac{\pi}{\xi_g}\right)^2\left(\frac{\sin\pi ts}{\pi s}\right)^2. \qquad (3.18)$$

It should be noted that the total Bragg diffracted beam intensity, unlike equation (3.12), is not a function of r. The validity of equation (3.18) will be discussed in §4.

3.7. Double diffraction

For incident fast electrons the Ewald sphere radius of curvature is very large with respect to reciprocal lattice vectors (for 100 keV electrons, $k=\lambda^{-1}\approx 27$ Å^{-1}). Since for a thin crystal each reciprocal lattice spot is effectively extended into a spike, many spikes usually cut the Ewald sphere. Hence a typical electron diffraction pattern, using monochromatic electrons, has many diffraction spots. For monochromatic x-ray diffraction, on the other hand, the radius of curvature of the Ewald sphere is small ($k\sim 1$ Å^{-1}) and the crystal thickness is large, hence the crystal has to be orientated very carefully to obtain even one diffracted beam.

Since a number of strong diffracted beams can easily occur in the diffraction of fast electrons, double and multiple diffraction must occur. An example of this is the 222 reflection in the diamond structure. The structure amplitude for the 222 reflection, $F(222)$, is zero if spherical atoms are assumed. However, atoms in the diamond structure are covalently bonded, and hence non-spherical, and $F(222)$ has a small finite value. In x-ray diffraction a very weak 222 reflection is observed, and a measurement of this intensity gives direct evidence of the bonding charge. In electron diffraction, on the other hand, the 222 reflection usually appears strongly on the diffraction pattern, due to the double diffraction from 111 (the electron beam is first scattered from 0 to 111 involving $F(111)$ and is then re-scattered from 111 to 222, again involving $F(111)$). Thus in this case the double diffraction to 222 resulting from two successive 111 scatterings completely masks the small direct $F(222)$ scattering. In general, if $(h_1k_1l_1)$ and $(h_2k_2l_2)$ are two allowed diffraction spots, then $(h_1+h_2,\ k_1+k_2,\ l_1+l_2)$ is also an allowed double-diffraction spot. (It should be pointed out that forbidden reflections which result entirely from the choice of a non-primitive unit cell cannot be generated by double diffraction.)

3.8. Forbidden reflections

We have made the assumption that for a perfect crystal a reflection is forbidden if the structure factor for that reflection is zero (§3.3). This assumption is correct if the crystal is perfect and if it contains an integral number of unit cells. However, crystal surfaces are not atomically smooth but contain steps, the height of which may not be an integral number of unit cells. For example, consider a {111} surface of an FCC crystal. The stacking of close-packed planes along [111] is ABCABCABC ... in conventional crystallographic notation. A surface step may therefore be of height $n/3$ unit cells, where n is an integer, so that the crystal thickness does not necessarily correspond to an integral number of unit cells. Hence, although $F_g=0$ for a particular reflection, that reflection may be present with very weak intensity if the crystal is not an integral number of unit cells thick. The fact that a finite intensity can occur in a 'forbidden' reflection for the above reason appears to have been first pointed out by Morris *et al* (1968).

Cherns (1974) has utilised such 'forbidden' reflections to image directly monatomic surface steps on thin metal films (see figure 11 (plate)). Using a different direct imaging technique Moodie and Warble (1967) have resolved atomic scale surface

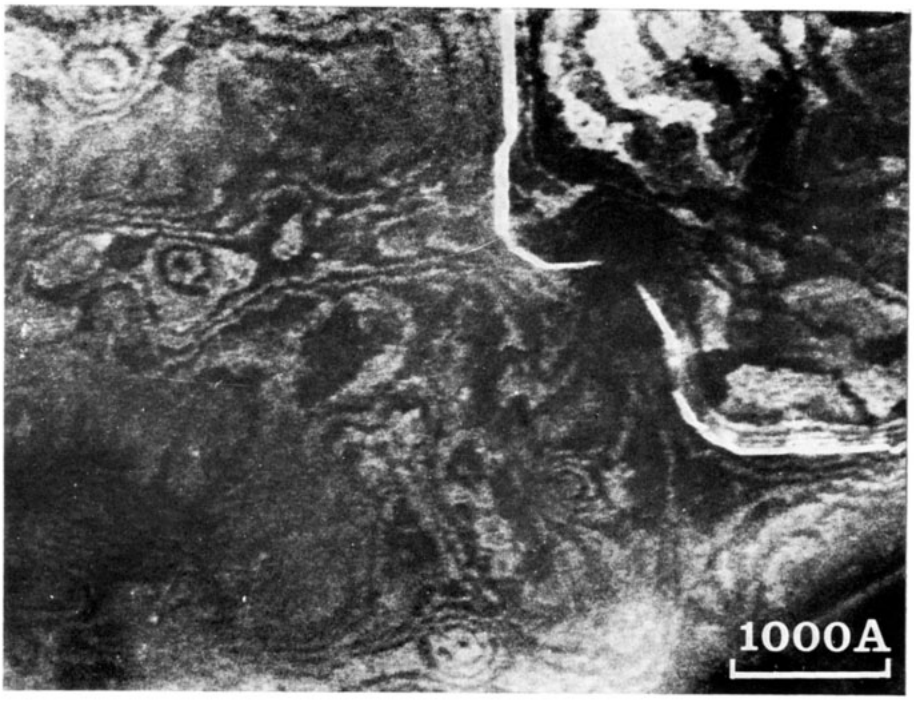

Figure 11. Monatomic surface steps on a 400 Å thick evaporated (111) gold film imaged to atomic resolution using a 'forbidden' reflection (from Cherns (1979), by courtesy of North-Holland).

steps on magnesium oxide crystals. Since surface step sites are believed to be preferred sites for chemical activity (e.g. reduction, oxidation and catalysis), the ability to image directly such sites may be of considerable importance in the determination of catalytic mechanisms, for example.

4. Elastic scattering by non-absorbing perfect crystals

4.1. The crystal potential

The crystal potential 'seen' by incident electrons is of fundamental importance in electron diffraction, since it is this potential which is responsible for the scattering and it is this potential which features in calculations of diffraction contrast. Whereas a great deal of thought has been given by solid-state physicists to the nature of the potential seen by the conduction electrons in crystals, very little consideration has been given until recently to the nature of the potential seen by an incident beam of fast electrons (see, for example, Kambe and Molière 1970, Dederichs 1972, Howie and Stern 1972, Humphreys 1977, Smart and Humphreys 1978).

It is of interest to note that electron diffraction theory is basically similar to band theory (electron diffraction theory in fact came first (Bethe 1928)) except that in electron diffraction the incident electron energy is fixed and positive and the problem is to find permitted values of the electron wavevector inside the crystal: in band theory, on the other hand, the problem is to find permitted values of the electron energy (negative corresponding to bound states) for given values of the wavevector and so to build up E against k curves (Humphreys and Fisher 1971, Stern *et al* 1969).

The incident electrons undergo elastic and inelastic scattering in the crystal, which gives rise to diffraction, refraction and absorption, and which may be represented by an 'optical' potential (see, for example, Yoshioka 1957, Mott and Massey 1965), which is the potential that the incident electrons effectively see, of the form

$$V^{\text{opt}}(\boldsymbol{r}) = V(\boldsymbol{r}) + \mathrm{i}V'(\boldsymbol{r}) + \Delta V(\boldsymbol{r}) \tag{4.1}$$

where $V(\boldsymbol{r})$ is due to elastic scattering, $V'(\boldsymbol{r})$ is due to inelastic scattering, and $\Delta V(\boldsymbol{r})$ is a real part addition to the potential due to virtual inelastic scattering processes. $V'(\boldsymbol{r})$ and $\Delta V(\boldsymbol{r})$ are considered further in §5.

By definition a perfect crystal is periodic, hence we can expand the crystal potential as a Fourier series based on either the real space or the reciprocal space lattice, i.e. we may write $V(\boldsymbol{r})$ as

$$V(\boldsymbol{r}) = \sum_{\boldsymbol{g}} V_{\boldsymbol{g}} \exp(2\pi \mathrm{i}\boldsymbol{g}.\boldsymbol{r}) \tag{4.2}$$

where $\boldsymbol{g}$ is a reciprocal lattice vector. Equation (4.2) explicitly takes into account the translational symmetry of the crystal structure. $V(\boldsymbol{r})$ must also have the rotational symmetry of the crystal structure. This is taken into account in equation (4.2) by having the $V_{\boldsymbol{g}}$ appropriately related. As a simple example, if the crystal possesses a centre of symmetry then $V(\boldsymbol{r}) = V(-\boldsymbol{r})$. Hence from equation (4.2) it follows that we must have $V_{\boldsymbol{g}} = V_{-\boldsymbol{g}}$ for all values of $\boldsymbol{g}$. With the $V_{\boldsymbol{g}}$ correctly chosen for a given crystal structure equation (4.2) is thus a valid expansion of $V(\boldsymbol{r})$. We may similarly express $V'(\boldsymbol{r})$ and $\Delta V(\boldsymbol{r})$ as Fourier series and the $\boldsymbol{g}$th Fourier coefficient of the optical potential is therefore

$$V_{\boldsymbol{g}}^{\text{opt}} = V_{\boldsymbol{g}} + \mathrm{i}V_{\boldsymbol{g}}' + \Delta V_{\boldsymbol{g}}. \tag{4.3}$$

The real part of the optical potential is often called the crystal potential and any measurement of this real crystal potential therefore measures $(V_g+\Delta V_g)$. Although calculations exist of ΔV_0, the mean real part addition to the potential (Yoshioka 1957, Ichikawa and Ohtsuki 1968), no calculations have existed until recently of the magnitude of the more important quantity ΔV_g $(g\neq 0)$. It has now been shown (Rez 1978a) that for 100 keV incident electrons $\Delta V_g/V_g$ is typically between 10^{-4} and 10^{-5}, which is less than the current experimental errors in measuring the real part of the potential. Hence for fast incident electrons the real part of the potential is essentially due only to elastic scattering since virtual inelastic scattering is negligible.

The elastic scattering part of the potential, $V(\boldsymbol{r})$, is in principle due to both the Coulomb interaction between the incident electron and the crystal and to exchange. However, the exchange terms are negligible for incident electron energies over about 50 keV (Rez 1978a). Thus we have the important result that for fast incident electrons (50 keV and above) exchange and virtual inelastic scattering are negligible and the crystal potential seen by the fast incident electron is simply Coulombic for the elastic scattering, plus an imaginary part $iV'(\boldsymbol{r})$ to represent absorption, considered further in §5.

Hence, the real crystal potential seen by incident fast electrons is simply related to the crystal charge density $\rho(\boldsymbol{r})$ by Poisson's equation. In considering the scattering of fast electrons by crystals we are therefore in the fortunate position of knowing the nature of the crystal potential, unlike the situation in band theory or low-energy electron diffraction (LEED) in which exchange, correlation and virtual inelastic scattering complicate the situation considerably.

The electron microscope can be used for accurate measurement of the crystal potential. This will of course differ from isolated free-atom potentials since the crystal potential seen by the incident fast electrons includes all solid-state bonding effects. For example, it has recently been found using electron microscopy that V_{100} for graphite deviates by about 9% from the calculated spherical free-atom value (Goodman 1976); and the critical voltage effect (see §5.9) has been used to investigate in some detail the covalent bonding charge density distribution in Si and Ge (Hewat and Humphreys 1974).

From equation (4.2) we have

$$V_g=\frac{1}{V_{\text{cell}}}\int_{\text{cell}} V(\boldsymbol{r})\exp\left(-2\pi i\boldsymbol{g}.\boldsymbol{r}\right)\mathrm{d}\boldsymbol{r} \tag{4.4}$$

where V_{cell} is the volume of the unit cell and the integral is taken over this cell. Comparing equations (4.4), (2.9) and (3.5) it is clear that

$$V_g=\frac{h^2}{2\pi meV_{\text{cell}}}F_g. \tag{4.5}$$

Thus the Fourier coefficients of the real crystal potential are exactly related to structure amplitudes F_g for electrons as determined from the first Born approximation (equations (3.5) and (2.9)) provided that the potential $V(\boldsymbol{r})$ in equation (2.9) takes into account solid-state bonding effects. The fact that equation (4.5) is exact when F_g is calculated using an expression identical to the first Born approximation is a subtle point and it has caused a great deal of confusion in the literature. The ex-

planation is that from equation (4.4) V_g must be exactly related to the Fourier transform of the atomic potential (corrected for solid-state bonding). It so happens that this Fourier transform is identical to the expression for the first Born approximation (equation (2.9)).

A number of authors (for example, Hoerni 1956, Boersch *et al* 1964) have calculated f_g and F_g using higher-order Born approximations, or using phase-shift methods, which yield complex scattering amplitudes. These complex amplitudes have then been substituted in equation (4.5) to yield a complex potential. This is clearly wrong since only elastic scattering has been considered and the complex part of the potential (equation (4.3)) can only arise from inelastic scattering. Although the scattering factors calculated using higher-order Born approximations, or using phase-shift methods, give the correct results for scattering from free atoms and molecules (see §§2.1–2.3), it is the expression which happens to be identical to the first Born approximation, i.e. equation (2.9), which should be used in calculating f_g, F_g and V_g for crystals, using equation (4.5). For further details see, for example, Fukuhara (1965) and Cowley and Moodie (1970).

Scattering factors reliably corrected for solid-state bonding effects are not readily available for most materials and as a first approximation theoretical free-atom scattering factors are usually used in equation (4.5) to calculate values of V_g. For example, the relativistic Hartree–Fock free-atom values tabulated by Doyle and Turner (1968) are widely used in electron diffraction calculations.

To a good approximation the effect of thermal vibrations of the atoms on the electron structure amplitude may be taken into account by the Debye–Waller factor, as in standard x-ray diffraction theory (e.g. James 1967). Hence $F_g{}^T$, the structure amplitude at temperature T, is related to F_g, the structure amplitude for zero atomic vibration, by

$$F_g{}^T = F_g \exp(-M) \tag{4.6}$$

where $M = 8\pi^2\overline{u_s{}^2}(\sin^2\theta)/\lambda^2 = Bg^2/4$ where M is the Debye–Waller factor, $\overline{u_s{}^2}$ is the mean-square displacement of the atom, and $B = 8\pi^2\overline{u_s{}^2}$ is the 'temperature factor' of the atom. Values of B for different materials and temperatures are given in the *International Tables for X-ray Crystallography* (1962). It should be noted that M varies as g^2, and thus for high-order reflections the Debye–Waller factor is extremely important. For example, for the 555 reflection in gold the room-temperature value of the structure amplitude is only one-half of the zero vibration value. The related Fourier coefficient of potential is also halved (equation (4.5)) and the extinction distance is doubled (equation (3.17)). It should be borne in mind that values of B and the related Debye temperature determined from diffraction experiments may be considerably different from those determined from specific heat measurements since the phonon spectrum is weighted differently. It is of course the Debye temperature determined from diffraction experiments which should be used in equation (4.6).

4.2. The breakdown of the kinematical theory

Equation (3.18) gives the diffracted intensity in the gth diffracted beam from a crystal of thickness t as

$$I_g(t) = \left(\frac{\pi}{\xi_g}\right)^2 \left(\frac{\sin \pi t s}{\pi s}\right)^2. \tag{4.7}$$

At the exact Bragg position, $s=0$ and

$$I_g(t)=\left(\frac{\pi t}{\xi_g}\right)^2. \tag{4.8}$$

Now $I_g(t)$ cannot be greater than unity, the incident beam intensity, hence an upper limit of the foil thickness t_{max} for which kinematical theory is valid at the Bragg position is $t_{max}=\xi_g/\pi$. Since extinction distances are typically a few hundred Å for 100 keV incident electrons, $t_{max}\sim 100$ Å. In fact this must be very much an upper limit since kinematical theory assumes only single scattering and hence assumes that the diffracted beam is very much weaker than the incident beam. We might expect kinematical theory to be valid if $I_g(t)\approx 0{\cdot}1$, i.e. if $t\leqslant 30$ Å. Since typical specimen thicknesses in conventional 100 keV electron microscopy are ~ 1000 Å, it is clear that kinematical theory normally cannot be used and instead a theory which considers multiple scattering within the specimen, a dynamical theory, must be used.

The fact that single-scattering kinematical theories are not normally valid in the electron microscopy of crystals is not always appreciated and has caused, and still causes, considerable confusion, particularly in the interpretation of lattice images of crystals containing defects (see Cockayne *et al* 1971b). However if s, the deviation from the Bragg condition, is large then from equation (4.7) $I_g(t)$ may be small and kinematical theory may still be usefully applied (see, for example, Whelan 1975). Due to its very limited quantitative use we shall not consider the kinematical theory further in this review.

4.3. Relativistic effects

Electrons in a conventional electron microscope have an energy of 100 keV and travel with 55% of the speed of light. 1 MeV electrons in a high-voltage electron microscope travel at 94% of the speed of light. Thus a theory of diffraction and microscopy using fast electrons must take into account relativistic effects.

Fujiwara (1962) and Howie (1962, see Whelan 1962) showed by different methods that the effects of electron spin appear to be negligible and hence fortunately we do not need to solve the Dirac equation. They showed that relativistic effects are adequately taken into account by solving the Schrödinger equation, provided that relativistic corrections to the electron mass and wavelength are made. Thus for an incident electron of velocity v and energy eE, where E is the accelerating potential, the relativistic mass and wavelength are:

$$m=m_0(1-v^2/c^2)^{-1/2} \tag{4.9}$$

and

$$\lambda=\frac{h}{[2m_0eE(1+eE/2m_0c^2)]^{1/2}} \tag{4.10}$$

where c is the velocity of light.

The real part of the crystal potential $V(\boldsymbol{r})$, and hence the V_g, seen by the incident electrons is independent of the incident electron energy (provided this is sufficiently high that exchange and virtual inelastic scattering are negligible, see §4.1). The electron scattering amplitude and the structure amplitude $f(\theta)$ and F_g, respectively, are a function of m and hence vary with the incident electron energy as $[1-(v/c)^2]^{-1/2}$.

The extinction distance ξ_g (defined by equation (3.17)) varies as v (the variation in cos θ being negligible). The absorption distance ξ_g', to be defined (equation (5.20)),

varies approximately as v^2 (this neglects retardation effects (Terakura *et al* 1966) and aperture effects (Humphreys 1972)). It should be borne in mind that other parameters associated with the incident electron may need to be relativistically corrected.

A relatively simple derivation of equations (4.9) and (4.10) is as follows. In the non-relativistic case, the total electron energy W $(=eE)$ is

$$W=\frac{p^2}{2m}+(-e)V(\boldsymbol{r}).$$

The equivalent relativistic equation is

$$p^2c^2+m_0{}^2c^4=[e(E+V)+m_0c^2]^2=W_r{}^2$$

where W_r is the relativistic total energy:

$$W_r=mc^2=e(E+V)+m_0c^2.$$

Hence

$$p^2c^2=e^2E^2+2eEm_0c^2+2mc^2eV-e^2V^2.$$

Neglecting e^2V^2 gives

$$p^2c^2-2mc^2eV=eE(2m_0c^2+eE).$$

Replace p by $-i\hbar\nabla$ and operate on ψ:

$$\nabla^2\psi+\frac{8\pi^2meV(\boldsymbol{r})\psi}{h^2}+\frac{8\pi^2m_0eE}{h^2}\left(1+\frac{eE}{2m_0c^2}\right)\psi=0.$$

This is effectively the Klein–Gordon equation for electron diffraction. This differs from the non-relativistic Schrödinger equation (equation (2.1)) in that:

(*a*) m replaced m_0 in the potential energy term $V(\boldsymbol{r})$, which gives equation (4.9);

(*b*) $E\rightarrow E(1+eE/2m_0c^2)$.

Hence, using the de Broglie relationship, the relativistic wavevector is

$$k_r=\frac{1}{\lambda_r}=\frac{2\,m_0eE(1+eE/2m_0c^2)^{1/2}}{h}$$

which gives equation (4.10).

4.4. Dynamical diffraction theory

Various theoretical approaches have been used for the formulation of the dynamical theory of electron diffraction. The method which will be used in this review is based on that given by Bethe (1928), in which the wavefunction for fast electrons within the crystal is represented by a linear superposition of Bloch waves. This approach is analogous to the nearly-free electron model developed subsequently in band theory.

Other approaches include the wave-optical method of Howie and Whelan (1961), which is similar to the x-ray diffraction theory of Darwin (1914); a different wave-optical theory of Cowley and Moodie (1957) using the concept of transmission through a large number of crystal slices of very small thickness; a real-space theory of Berry (1971) which considers the crystal as a periodic array of potential wells, with transmission and reflection of the incident electrons at the well boundaries, and a group-theoretical algebraic approach by Hurley *et al* (1978). The Bethe

(1928) theory has been developed by MacGillavry (1940), Sturkey (1957), Fujimoto (1959) and Niehrs (1959a, b). The nature and inter-relation of some of the various theories of electron diffraction has been discussed by Goodman and Moodie (1974).

The starting point in the Bethe theory is the Schrödinger equation for the wavefunction $\psi(\boldsymbol{r})$ of the fast electron within the crystal potential $V(\boldsymbol{r})$:

$$\nabla^2\psi(\boldsymbol{r})+\frac{8\pi^2 m|e|}{h^2}\,[E+V(\boldsymbol{r})]\,\psi(\boldsymbol{r})=0 \tag{4.11}$$

where m is the relativistic mass of the fast electron, given by equation (4.9), E is the incident electron accelerating potential (so that the total energy of the incident electron is $|e|E$), and $V(\boldsymbol{r})$ is the real crystal potential defined here as being positive since the incident electrons are attracted by the atoms.

We expand the periodic potential as a Fourier series based on the reciprocal lattice (see §4.1)

$$V(\boldsymbol{r})=\sum_{-\infty}^{\infty} V_h \exp(2\pi i\boldsymbol{h}.\boldsymbol{r}). \tag{4.12}$$

The electron wavefunction within the crystal may be represented by a Bloch wave

$$\psi(\boldsymbol{r})=C(\boldsymbol{r})\exp(2\pi i\boldsymbol{k}.\boldsymbol{r}) \tag{4.13}$$

where $C(\boldsymbol{r})$ has the periodicity of the lattice and hence may be expanded as a Fourier series based on the reciprocal lattice to give

$$\psi(\boldsymbol{r})=\sum_{g} C_g \exp[2\pi i(\boldsymbol{k}+\boldsymbol{g}).\boldsymbol{r}]. \tag{4.14}$$

The C_g are known as the Bloch wave coefficients.

The constants may be collected together by defining a 'modified potential' $U(\boldsymbol{r})$ with Fourier coefficients

$$U_h=\frac{2m|e|}{h^2}\,V_h \tag{4.15}$$

and a quantity K given by

$$K^2=\frac{2m|e|}{h^2}\,(E+V_0) \tag{4.16}$$

where K is the magnitude of the mean electron wavevector in the crystal after allowing for the mean crystal potential (a small correction: typically $E=10^5$ V, $V_0\sim 10$ V).

Substituting equations (4.12)–(4.16) in (4.11) yields

$$\sum_{g}\left\{[K^2-(\boldsymbol{k}+\boldsymbol{g})^2]C_g+\sum_{h\neq g} U_{g-h}C_h\right\}\exp[2\pi i(\boldsymbol{k}+\boldsymbol{g}).\boldsymbol{r}]=0. \tag{4.17}$$

Equation (4.17) holds for all points $\boldsymbol{r}$ in the crystal, hence the coefficient of each exponential term must be equal to zero (the coefficient is not a function of $\boldsymbol{r}$). Thus we have the set of equations

$$[K^2-(\boldsymbol{k}+\boldsymbol{g})^2]C_g+\sum_{h\neq g} U_{g-h}C_h=0 \tag{4.18}$$

there being one such equation for each value of $\boldsymbol{g}$ (i.e. each reflection) considered. The set of equations represented by equation (4.18) is exact provided an infinite number of $\boldsymbol{g}$ values is considered. In practice an approximate solution considering a finite number of reflections must be used in calculations. Equation (4.18) can

be solved to any required degree of accuracy by choosing the appropriate number of reflections to consider. For n reflections, we have n equations similar to equation (4.18) and n different Bloch wave solutions.

4.5. The two-beam approximation

As a first approximation, often only two reflections are considered in equation (4.18) (this approximation is similar to the nearly-free electron approximation in band theory). The two-beam approximation is in many cases, but not always, valid as a first approximation for 100 keV incident electrons although it breaks down for higher incident electron energies. Physically we may expect the two-beam approximation to be valid if one diffracted beam is much stronger than all others so that an incident beam of wavevector $\boldsymbol{k}$ gives rise to only two strong beams leaving the crystal (the transmitted beam of wavevector $\boldsymbol{k}$ and the diffracted beam of wavevector $(\boldsymbol{k}+\boldsymbol{g})$). Mathematically the two-beam approximation is valid if the Bloch wave expansion of equation (4.14) can be terminated, to a good approximation, after the first two terms, i.e.

$$\psi(\boldsymbol{r}) = C_0 \exp(2\pi i \boldsymbol{k}.\boldsymbol{r}) + C_g \exp[2\pi i(\boldsymbol{k}+\boldsymbol{g}).\boldsymbol{r}]. \tag{4.19}$$

In the two-beam approximation equation (4.18) is

$$\begin{aligned} (K^2-k^2)C_0 + U_{-g}C_g &= 0 \\ [K^2-(\boldsymbol{k}+\boldsymbol{g})^2]C_g + U_g C_0 &= 0. \end{aligned} \tag{4.20}$$

Writing equations (4.20) in matrix form:

$$\begin{pmatrix} K^2-k^2 & U_{-g} \\ U_g & K^2-(\boldsymbol{k}+\boldsymbol{g})^2 \end{pmatrix} \begin{pmatrix} C_0 \\ C_g \end{pmatrix} = 0. \tag{4.21}$$

Equation (4.21) has a solution if the determinant of the coefficients is equal to zero, i.e.

$$\begin{vmatrix} K^2-k^2 & U_{-g} \\ U_g & K^2-(\boldsymbol{k}+\boldsymbol{g})^2 \end{vmatrix} = 0. \tag{4.22}$$

Equation (4.22) is clearly an equation in k^4. If we had considered n beams instead of 2 beams we would similarly have had an equation in k^{2n}, with $2n$ roots. n of these roots are positive and n negative, corresponding to forward and backward propagation, respectively. Application of the boundary conditions (see §4.6) shows that for the transmission electron diffraction of fast electrons backward propagating waves are negligible (see, for example, Hirsch *et al* 1977), and hence we need only consider the n positive roots of k. For low-energy electron diffraction, on the other hand, it is necessary to consider all $2n$ roots (see Pendry 1974).

Now K is the magnitude of the fast electron wavevector after correction for the mean crystal potential (see equation (4.16)) and k is the magnitude of the wavevector of the fast electron within the crystal. Since the Fourier coefficients of crystal potential V_g are typically $\lesssim 10$ V and for fast electron diffraction the incident electron accelerating voltage is typically 10^5 V it can be seen that $K \approx k$. Also for fast electrons $K \gg g$, and therefore $K \approx |\boldsymbol{k}+\boldsymbol{g}|$. Hence in equation (4.22) we may, to a very good

approximation, put

$$K^2-k^2=2K(K-k)$$
$$K^2-(\boldsymbol{k}+\boldsymbol{g})^2=2K(K-|\boldsymbol{k}+\boldsymbol{g}|). \tag{4.23}$$

The above approximation is known as the high-energy approximation. Use of this approximation makes equation (4.22) quadratic in k, rather than quartic, since essentially it neglects back-reflected waves. Setting equation (4.23) in (4.22) yields

$$(K-k)(K-|\boldsymbol{k}+\boldsymbol{g}|)=U_gU_{-g}/4K^2. \tag{4.24}$$

Equation (4.24) has two roots $\boldsymbol{k}^{(1)}$ and $\boldsymbol{k}^{(2)}$. We will denote these roots by $\boldsymbol{k}^{(j)}$ $(j=1, 2)$.

4.6. The significance of more than one Bloch wave

Equation (4.24) shows that using the two-beam approximation we have two values of the electron wavevector inside the crystal for a given incident electron energy eE (where E is the accelerating potential). Similarly, if we consider n beams we have n values of $\boldsymbol{k}^{(j)}$ (n-beam theory will be given in §4.9). Each value of $\boldsymbol{k}^{(j)}$ is the electron wavevector corresponding to a different Bloch wave. We originally considered a particular Bloch wave solution, equation (4.14), to the Schrödinger equation. We now find that more than one wavevector is possible inside the crystal. Hence the general solution is a linear combination of Bloch waves, each with a different wavevector. The total wavefunction $\Psi(\boldsymbol{r})$ of the fast electron is therefore given by

$$\Psi(\boldsymbol{r})=\sum\alpha^{(j)}\psi^{(j)}(\boldsymbol{r})=\sum_j\alpha^{(j)}\sum_g C_g^{(j)}\exp\left[2\pi i(\boldsymbol{k}^{(j)}+\boldsymbol{g}).\boldsymbol{r}\right] \tag{4.25}$$

using equation (4.14). $\alpha^{(j)}$ is the amplitude (often called the excitation amplitude) of the jth Bloch wave $\psi^{(j)}(\boldsymbol{r})$.

Physically the crystal acts as an interferometer. An incident electron of energy eE and fixed wavevector is partitioned by the crystal into a set of Bloch waves of differing wavevectors $\boldsymbol{k}^{(j)}$. As each Bloch wave propagates it becomes out of phase with its neighbours (due to its different wavevector). Hence interference occurs, for example if the crystal thickness varies interference fringes known as thickness fringes are formed.

At the entrance surface of the crystal we must match the incident wave (assumed to be a plane wave throughout this review) with the total wave inside the crystal, given by equation (4.25). The boundary conditions are the usual quantum-mechanical ones for continuity of current at an interface, namely that Ψ and grad Ψ must be continuous. Define the z direction as the downward normal to the surface of the crystal. Let $k_z^{(j)}$ and $k_t^{(j)}$ be the components of $\boldsymbol{k}^{(j)}$ in the z direction and in the plane of the surface, respectively. Consider the symmetrical Laue case (with $\boldsymbol{g}$ parallel to the surface, i.e. $g_z=0$). It follows immediately from the continuity of $\Psi(\boldsymbol{r})$ at the surface $z=0$ that the tangential components of $\boldsymbol{k}^{(j)}$ must all be equal, and equal to the tangential component of the incident wavevector. We therefore set $k_t^{(j)}=k_t$ for all j. Hence, the wavevector of each Bloch wave differs only in the z direction in the symmetrical Laue case. In addition, continuity of Ψ and grad Ψ at the crystal entrance surface yields that $\alpha^{(j)}=C_0^{(j)*}$ (see §4.9).

Since the Bloch waves have different wavevectors, $\boldsymbol{k}^{(j)}$, they have different kinetic

energies. For elastic scattering the total energy (kinetic plus potential) is a constant equal to the incident electron energy. Hence each Bloch wave must have a different potential energy. This is physically due to a different localisation (defined as $|\psi^{(j)}(\boldsymbol{r})|^2$) of each Bloch wave within the crystal. The situation can be compared to that in band theory: at a Brillouin zone boundary on nearly-free electron theory the valence electron Bloch waves below and above the energy gap have a different localisation within the crystal (of the form $\sin^2$ and $\cos^2$); hence their potential energies are different. However, in the band theory case this difference is for a particular wavevector $\boldsymbol{k}$, i.e. a particular kinetic energy, and hence the total electron energy differs, yielding the familiar E against k curves of band theory.

4.7. The dispersion surface

The dispersion surface in electron diffraction is a plot of the allowed values of the z component of the Bloch wavevector $\boldsymbol{k}^{(j)}$ in the crystal. It is the electron diffraction equivalent of the E against k curves of band theory, and of similar importance.

Consider a particular Bloch wavevector $\boldsymbol{k}^{(j)}$ with components $k_z^{(j)}$ and k_t as described above, i.e.

$$k^{(j)2} = k_z^{(j)2} + k_t^2. \tag{4.26}$$

Using the high-energy approximation (see equation (4.23)) we have

$$K^2 - k^{(j)2} = K^2 - k_z^{(j)2} - k_t^2 \approx 2K(K - k_z^{(j)}) - k_t^2 \tag{4.27(a)}$$

$$\begin{aligned} K^2 - (\boldsymbol{k}^{(j)} + \boldsymbol{g})^2 &= (K^2 - k_z^{(j)2}) - (k_t^2 + 2gk_t + g^2) \\ &\approx 2K(K - k_z^{(j)}) - (k_t + g)^2 \end{aligned} \tag{4.27(b)}$$

since in the Laue case considered here $\boldsymbol{g}$ is parallel to k_t. If we solve the Schrödinger equation as before, but take as the fast electron wavefunction the general solution (4.25) rather than a particular Bloch wave solution (4.14), then the two-beam approximation equation (4.21) becomes generalised to

$$\begin{pmatrix} K^2 - k^{(j)2} & U_{-g} \\ U_g & K^2 - (\boldsymbol{k}^{(j)} + \boldsymbol{g})^2 \end{pmatrix} \begin{pmatrix} C_0^{(j)} \\ C_g^{(j)} \end{pmatrix} = 0. \tag{4.28}$$

Setting equations (4.27) in equation (4.28) yields

$$\frac{1}{2K} \begin{pmatrix} -k_t^2 & U_{-g} \\ U_g & -(k_t + g)^2 \end{pmatrix} \begin{pmatrix} C_0^{(j)} \\ C_g^{(j)} \end{pmatrix} = (k_z^{(j)} - K) \begin{pmatrix} C_0^{(j)} \\ C_g^{(j)} \end{pmatrix}. \tag{4.29}$$

Equation (4.29) is a standard eigenvalue equation of the form

$$\boldsymbol{A}\boldsymbol{C}^{(j)} = (k_z^{(j)} - K)\boldsymbol{C}^{(j)}. \tag{4.30}$$

Diagonalising the matrix $\boldsymbol{A}$ (using the normal methods) yields each eigenvalue $(k_z^{(j)} - K)$ and corresponding eigenvector $\boldsymbol{C}^{(j)}$.

Since $U(\boldsymbol{r})$ is real, $U_g = U_{-g}^*$ (asterix denotes complex conjugate) and the matrix $\boldsymbol{A}$ is Hermitian. Hence the eigenvalues $(k_z^{(j)} - K)$ are real although the eigenvectors $C_g^{(j)}$ are, in general, complex. If the crystal has a centre of symmetry and we choose this as the origin of $\boldsymbol{r}$, then $U_g = U_{-g}$ (see §4.1) $\boldsymbol{A}$ is real symmetric, and the eigenvalues and the eigenvectors are all real (for further properties of $\boldsymbol{A}$ see §4.9). In

the two-beam approximation $\boldsymbol{A}$ is the 2×2 matrix given by equation (4.29) and we write the two eigenvalues as $(k_z^{(1)}-K)$ and $(k_z^{(2)}-K)$. From equation (4.29) it is clear that for a given value of k_t, i.e. a given orientation of the incident beam with respect to the crystal, we have two values of $k_z^{(j)}$, i.e. $k_z^{(1)}$ and $k_z^{(2)}$. For a different value of k_t we have different values of $k_z^{(1)}$ and $k_z^{(2)}$. The dispersion surface is a plot of the permitted values of $k_z^{(j)}$ against k_t (where k_t is the component of the incident wavevector parallel to the crystal surface). The curve for a particular Bloch wave, i.e. for wave 1 or 2, is called a branch of the dispersion surface. Thus in the two-beam approximation the dispersion surface has two branches as shown in figure 12. If n beams are considered we have n Bloch waves with n values of $k_z^{(j)}$ for a given k_t and hence the dispersion surface has n branches (see figure 13). Since we are plotting the z component of $\boldsymbol{k}^{(j)}$, the extended dispersion surface is periodic with $\boldsymbol{g}$, i.e. it is a periodic zone scheme representation similar to the periodic zone scheme E against k curves of band theory. It should be noted that at the exact Bragg position $k_t=-0{\cdot}5g$, the minus sign arising since the incident beam wavevector is directed to 0 and not to g.

It is useful to consider 'free-electron theory' for the incident fast electron within the crystal. Neglecting diffraction, by setting $U_g=U_{-g}=0$ in equation (4.29), yields as a solution that the electron wavevector should lie on one of two free-electron

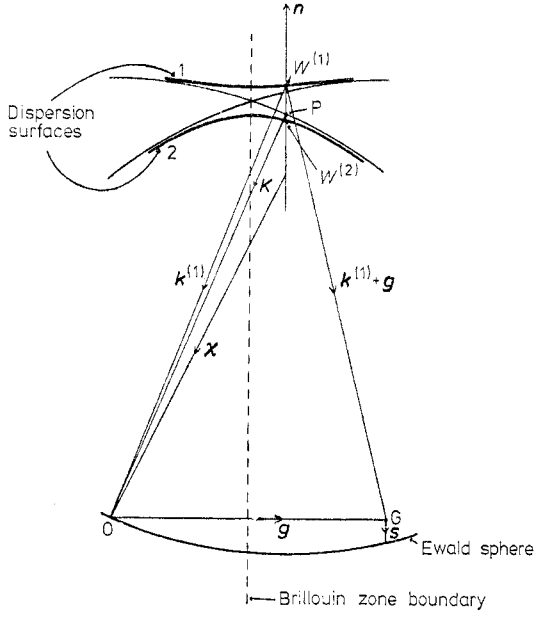

Figure 12. The dispersion surface in the two-beam approximation. χ is the incident wavevector, $\boldsymbol{K}$ is the incident wavevector after correction for the mean crystal potential. The Ewald sphere is the sphere, radius K centre P. The dispersion surface is asymptotic to a sphere, radius K centre O, and a sphere, radius K centre G, as shown. The surface is a plot of $k_z^{(j)}$ against k_t (see text). The waves excited in the crystal correspond to the wave-points $W^{(1)}$ and $W^{(2)}$. $W^{(1)}$ and $W^{(2)}$ are the points of intersection of the dispersion surface branches 1 and 2 with the normal $\boldsymbol{n}$ to the crystal, the normal passing through the end-point of χ as shown. For clarity only the wavevectors from wave-point $W^{(1)}$ are shown (i.e. $\boldsymbol{k}^{(1)}$ and $\boldsymbol{k}^{(1)}+\boldsymbol{g}$). The diagram is not to scale.

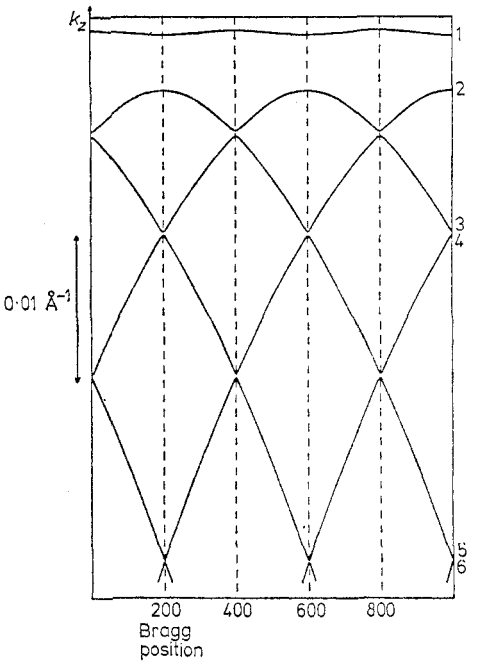

Figure 13. n-beam dispersion surface for 100 keV electrons incident upon copper. Note the periodicity of the surface (i.e. this is a periodic zone scheme representation). The dispersion surface branches are clearly asymptotic to spheres (distorted in the figure since the k_z scale is enlarged relative to k_t).

spheres of radius K, one centred on the origin of reciprocal space and one centred on the reciprocal lattice point g as shown in figure 12. These spheres intersect at the Brillouin zone boundary, i.e. at the exact Bragg position for which $k_t = -0{\cdot}5\,g$. Switching on the crystal potential (i.e. setting $U_g \neq 0$) removes this degeneracy. The dispersion surface branches become asymptotic to the free-electron spheres of radius K away from the Bragg position. (K is the incident electron wavevector corrected for the mean inner crystal potential, hence the free-electron spheres are in fact 'corrected' free-electron spheres for the fast electron in the crystal.)

The numbering system used for labelling the dispersion surface branches and the corresponding Bloch waves is a topic of some confusion. Prior to about 1971, most calculations used the two-beam approximation and the system normally used in publications was to label the top branch of the dispersion surface (i.e. the branch with the highest $k_z^{(j)}$ value) branch 2 (i.e. $k_z^{(2)}$) and the next branch, branch 1. Since about 1971, n-beam calculations ($n > 2$) have been more widely used, most of which adopt an ordered labelling scheme (Humphreys and Fisher 1971) which numbers the dispersion surface branches from the upper to the lower, i.e. 1, 2, 3, 4, etc, in order of decreasing $k_z^{(j)}$. This scheme will be used throughout this review.

Just as the Ewald sphere construction is a useful geometrical aid in kinematical diffraction theory, the dispersion surface is a useful geometrical aid in dynamical diffraction theory. We know that the tangential components of $\boldsymbol{k}^{(j)}$ are all equal to the tangential component of the incident wavevector (see §4.6). Hence, to find the allowed values of the $\boldsymbol{k}^{(j)}$ for a given orientation of the crystal with respect to the incident beam we construct a normal to the crystal surface through the end of $\boldsymbol{K}$ at P in figure 12 (or equivalently through the end point of $\boldsymbol{\chi}$, the vacuum wave-

vector). The intersections of this normal with the branches of the dispersion surface give the 'wave-points' corresponding to $\boldsymbol{k}^{(j)}$. The individual wavevectors $\boldsymbol{k}^{(j)}$ and $\boldsymbol{k}^{(j)}+\boldsymbol{g}$ can then be drawn in as shown.

4.8. Diffracted intensities: two-beam theory

From equation (4.25), the electron wavefunction at the bottom of the crystal of thickness t is

$$\Psi(t)=\sum_j \alpha^{(j)} \sum_g C_g^{(j)} \exp\left[2\pi i(\boldsymbol{k}^{(j)}+\boldsymbol{g})_z t\right]. \tag{4.31}$$

Since z is defined as perpendicular to $\boldsymbol{g}$, $\boldsymbol{g}_z=0$. At the bottom surface of the crystal the Bloch waves decouple into their plane wave components, so that the amplitude in the diffracted beam direction $(\boldsymbol{k}+\boldsymbol{g})$ is

$$v_g(t)=\sum_j \alpha^{(j)} C_g^{(j)} \exp\left(2\pi i k_z^{(j)} t\right) \tag{4.32}$$

where $\alpha^{(j)}=C_0^{(j)*}$ (see § 4.6).

Hence the intensity scattered in the gth diffracted beam is

$$I_g(t)=\left|\sum_j C_0^{(j)*} C_g^{(j)} \exp\left(2\pi i k_z^{(j)} t\right)\right|^2. \tag{4.33}$$

Consider the crystal set at the exact Bragg position for the reflection g, so that the reciprocal lattice point g lies on the Ewald sphere and $|\boldsymbol{k}|=|\boldsymbol{k}+\boldsymbol{g}|$. k_t, the component of the incident beam wavevector along the direction $\boldsymbol{g}$, is then $-0{\cdot}5\boldsymbol{g}$, and equation (4.28) or (4.29) is easily solved to give

$$(k_z^{(1)}-k_z^{(2)})=U_g/K\cos\theta_B \tag{4.34}$$

and

$$C_0^{(1)}=C_0^{(2)}=C_g^{(1)}=-C_g^{(2)}=2^{-1/2} \tag{4.35}$$

taking the $C_g^{(j)}$ to be normalised, i.e. $\Sigma_g C_g^{(j)2}=1$, and assuming a centrosymmetric crystal (i.e. $U_g=U_{-g}$).

From figure 12, $(k_z^{(1)}-k_z^{(2)})$ is the separation of branches 1 and 2 of the dispersion surface, and equation (4.34) gives the minimum value of this separation, which occurs at the Bragg position. The extinction distance is defined to be the inverse of this minimum separation, i.e.

$$\xi_g=(k_z^{(1)}-k_z^{(2)})^{-1}=K(\cos\theta_B)/U_g. \tag{4.36}$$

The expression for the extinction distance given by equation (4.36) is identical to that used in kinematical theory (equation (3.17)), as can be seen by using equations (4.5) and (4.15), except that K, the mean wavevector of the fast electron within the crystal, replaces the incident wavevector used in the kinematical theory expression, a very small correction. θ_B is typically 10^{-2} rad for 100 keV incident electrons and hence to a good approximation we may set $\cos\theta_B=1$ in equation (4.36).

From equations (4.33)–(4.36), the intensities diffracted from a perfect crystal of thickness t at the Bragg position on the two-beam dynamical theory are:

$$\begin{aligned} I_0(t)&=\cos^2(\pi t/\xi_g)\\ I_g(t)&=\sin^2(\pi t/\xi_g) \end{aligned} \tag{4.37}$$

where $I_0(t)$ and $I_g(t)$ are the transmitted and diffracted intensities, respectively,

plotted in figure 14. For varying t there is an interchange of intensity between the two beams analogous to the energy interchange of two coupled pendulums. Intensity is conserved as expected (i.e. $I_0(t)+I_g(t)=1$). The intensity in the diffracted beam is zero for $t=n\xi_g$ (n an integer), hence the term extinction distance. The periodicity of thickness fringes is ξ_g in both the transmitted and the diffracted beams (see figure 14), i.e. ξ_g is the 'oscillation distance' resulting from the interference between the two superimposed Bloch waves having different $\boldsymbol{k}$ vectors.

Equation (4.28) or (4.29) can also be solved by hand for the crystal deviated from the Bragg position. Using the Ewald sphere construction (figure 7(*b*)) simple geometry shows that the deviation parameters s and k_t are related by

$$\begin{aligned} k_t &= -\frac{g}{2}-\frac{s}{2\tan\theta_B} \\ &\approx -\frac{g}{2}-\frac{sK}{g}. \end{aligned} \tag{4.38}$$

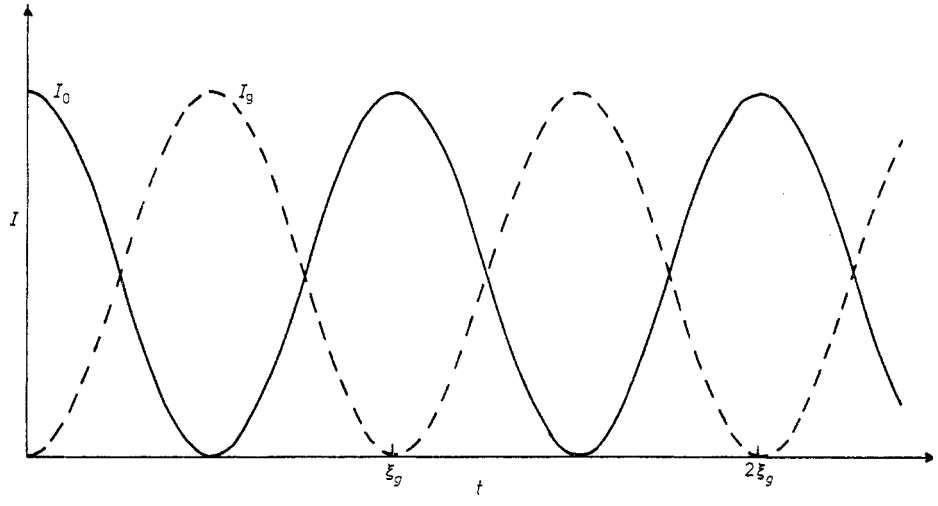

Figure 14. The variation of intensity with crystal thickness for a crystal at a Bragg position, two-beam theory, no absorption. ξ_g is the extinction distance, i.e. the periodicity of the thickness fringes.

It is convenient algebraically to introduce a further deviation parameter β (Takagi 1962) defined by

$$\cot\beta = s\xi_g = w. \tag{4.39}$$

In terms of β the solution of equation (4.28) or (4.29) for an arbitrary deviation can be written as follows:

$$\begin{aligned} C_0^{(1)} &= -C_g^{(2)} = \sin\tfrac{1}{2}\beta \\ C_0^{(2)} &= C_g^{(1)} = \cos\tfrac{1}{2}\beta. \end{aligned} \tag{4.40}$$

Equations (4.40) are very useful compact analytical forms. In the general case the direct and diffracted beam intensities may be easily shown to be

$$\begin{aligned} I_0(t) &= 1-I_g(t) \\ I_g(t) &= \left(\frac{\pi}{\xi_g}\right)^2\left(\frac{\sin\pi ts'}{\pi s'}\right)^2 \end{aligned} \tag{4.41}$$

where

$$s' = (s^2 + \xi_g^{-2})^{1/2}. \tag{4.42}$$

Equation (4.41) is similar in form to the kinematical theory equation (3.18) except that s is replaced by s'. This is a very important difference, however, since in most electron scattering experiments the crystal is oriented close to a Bragg position so that s is small and s' differs appreciably from s. Thus, as argued qualitatively in §4.2, kinematical theory normally is not valid. However, if s is large then $s' \approx s$, the diffracted beam is very weak, and kinematical theory may be a useful approximation under these conditions (see Cockayne *et al* (1969) for the application of kinematical theory to the weak-beam method of dislocation imaging).

4.9. The many-beam dynamical theory and matrix notation

The two-beam approximation considered above is often a valid first approximation for 100 keV incident electrons. However it breaks down even as a first approximation for higher-energy incident electrons (see Humphreys *et al* 1971). Hence for all accurate quantitative work, and for some qualitative work, a many-beam dynamical theory is necessary. This is a straightforward algebraic extension of the two-beam theory, although the many-beam equations usually require a computer for their solution. The necessary extensions of the two-beam theory are briefly presented below.

The total wavefunction of the fast electron within the crystal is given by equation (4.25). The many-beam theory eigenvalue equation (the so-called secular equation) is a straightforward extension of the two-beam equation (4.29), i.e.

$$\frac{1}{2K}\begin{bmatrix} -k_t^2 & U_{-g} & U_{-h} & \cdots \\ U_g & -(k_t+g)^2 & U_{g-h} & \cdots \\ U_h & U_{h-g} & -(k_t+h)^2 & \cdots \\ \cdot & \cdot & \cdot & \\ \cdot & \cdot & \cdot & \\ \cdot & \cdot & \cdot & \end{bmatrix} \begin{bmatrix} C_0^{(j)} \\ C_g^{(j)} \\ C_h^{(j)} \\ \\ \\ \end{bmatrix} = (k_z^{(j)} - K) \begin{bmatrix} C_0^{(j)} \\ C_g^{(j)} \\ C_h^{(j)} \\ \\ \\ \end{bmatrix} \tag{4.43}$$

i.e. the many-beam equation is of the form

$$\boldsymbol{A}\boldsymbol{C}^{(j)} = (k_z^{(j)} - K)\boldsymbol{C}^{(j)}. \tag{4.44}$$

If n beams are considered (including the forward scattered beam for which $g=0$) $\boldsymbol{A}$ is an $(n \times n)$ matrix, and there are n eigenvalues and n Bloch waves, each Bloch wave having n plane wave components.

For a non-centrosymmetric crystal $\boldsymbol{A}$ is Hermitian since $U_g = U_{-g}^*$, the eigenvalues are real and the $(n \times n)$ eigenvector matrix $\boldsymbol{C}$, the columns of which are the complex eigenvectors $\boldsymbol{C}^{(j)}$, is unitary, i.e.

$$\boldsymbol{C}^{-1} = \boldsymbol{C}^{\dagger} = \tilde{\boldsymbol{C}}^*. \tag{4.45}$$

The physical interpretation of equation (4.45) is clearer if the terms are explicitly written out, which yields:

$$\sum_g C_g^{(i)} C_g^{(j)*} = \delta_{ij} \tag{4.46}$$

and

$$\sum_j C_g^{(j)} C_h^{(j)*} = \delta_{gh} \tag{4.47}$$

i.e. the eigenvectors form a complete orthogonal and normalised set.

For the particular case of a centrosymmetric crystal $\boldsymbol{A}$ is real symmetric, all the eigenvalues and the eigenvectors are real and $\boldsymbol{C}$ is a real orthogonal matrix (i.e. $\tilde{\boldsymbol{C}} = \boldsymbol{C}^{-1}$). If the n eigenvalues are plotted out, a dispersion surface with n 'branches' is obtained, as in figure 13.

The boundary condition of continuity of the wavefunction at the top crystal surface gives immediately that for an incident beam of unit amplitude the amplitudes $\alpha^{(j)}$ of the Bloch waves excited in the crystal must be such that $\Sigma_j \alpha^{(j)} C_0^{(j)} = 1$, or in matrix form

$$\boldsymbol{C}\boldsymbol{\alpha} = \boldsymbol{u} \tag{4.48}$$

where the column vector $\boldsymbol{u}$ has the first element equal to 1 and all other elements zero. Using equation (4.45):

$$\boldsymbol{\alpha} = \boldsymbol{C}^{-1}\boldsymbol{u} = \tilde{\boldsymbol{C}}^*\boldsymbol{u}. \tag{4.49}$$

Thus $\alpha^{(j)} = C_0^{(j)*}$, as assumed earlier in §4.6.

The amplitude of the gth diffracted beam leaving the bottom of the crystal has already been given as

$$v_g(t) = \sum_j \alpha^{(j)} C_g^{(j)} \exp(2\pi i k_z^{(j)} t). \tag{4.32}$$

We may write the amplitudes of all the diffracted beams as the column vector $\boldsymbol{v}$ where

$$\boldsymbol{v} = \begin{bmatrix} v_0(t) \\ v_g(t) \\ v_h(t) \\ \cdot \\ \cdot \\ \cdot \end{bmatrix}.$$

Thus using equations (4.49) and (4.32) the amplitudes of all the diffracted beams are

$$\begin{aligned} \boldsymbol{v} &= \boldsymbol{C}[\exp(2\pi i k_z^{(j)} t)]_{\mathrm{D}} \boldsymbol{\alpha} \\ &= \boldsymbol{C}[\exp(2\pi i k_z^{(j)} t)]_{\mathrm{D}} \boldsymbol{C}^{-1}\boldsymbol{u} \end{aligned} \tag{4.50}$$

where $[\ ]_{\mathrm{D}}$ denotes a diagonal matrix. Thus the diffracted beam amplitudes from a crystal of thickness t are completely specified by the eigenvalues and eigenvectors of $\boldsymbol{A}$. Equation (4.50) may be written in the compact form (Fujimoto 1959, Sturkey 1962)

$$\boldsymbol{v} = \exp(i\boldsymbol{A}t)\boldsymbol{u}. \tag{4.51}$$

5. Elastic scattering in absorbing crystals

5.1. Inelastic scattering and absorption

The theory developed in §4 considered only elastic scattering in a perfect non-absorbing crystal. We now consider the possibility of inelastic scattering and ab-

sorption. There are three main inelastic scattering mechanisms for fast electrons incident on a crystal. The incident electrons may be inelastically scattered by single-electron excitations, plasmons and phonons. The excitation of single electrons has been considered in §2.4 in connection with inelastic scattering by a single atom. In a crystal we also have the possibility of collective excitations, both collective electron excitations (plasmons) and collective atom excitations (phonons).

The general dynamical theory of the inelastic scattering of electrons by crystals was first formulated by Kainuma (1955) and Yoshioka (1957) and has been reviewed by Kambe and Molière (1970). The theory of plasmon scattering has been discussed by Howie (1963), single-electron excitations by Cundy *et al* (1969) and Humphreys and Whelan (1969), and phonon scattering by Takagi (1958), Gjønnes (1966), Natta (1968), Melander and Sandström (1975a, b) and Rez *et al* (1977). In this review we shall be mainly concerned with a simple phenomenological treatment of the effects of inelastic scattering although the important concept of resonance errors is discussed in §5.10.

Inelastic scattering causes the incident electrons not only to lose energy but it may also cause them to be angularly scattered out of Bragg-reflected beams. In an electron microscope an objective aperture is used to select one or more Bragg-reflected beams to form an image, and hence many of the inelastically scattered electrons are excluded from the image. These electrons are effectively absorbed. However, not all inelastic scattering produces absorption. For example, the angular distribution of incident electrons inelastically scattered by plasmons is sharply peaked about the forward-scattered and the Bragg-reflected beams. Thus many plasmon-scattered electrons pass through the objective aperture and contribute to the image. These electrons are therefore not absorbed and an important question is whether or not such electrons exhibit the same image contrast effects as the elastically scattered electrons. It must be emphasised that absorption in electron microscopy is not 'true absorption' in the sense of photoelectric absorption in which the incident photon is totally absorbed. Absorption as commonly understood in electron microscopy is due to electrons being excluded from the image because they have been inelastically scattered outside the objective aperture.

5.2. The phenomenological treatment of absorption

In optics it is well known that the effects of absorption can be treated mathematically by letting the refractive index be complex. In a somewhat analogous manner the refractive index of a crystal for incident electrons can be made complex and hence the optical potential $V^{\text{opt}}(\boldsymbol{r})$ is complex (see equation (4.1)). Yoshioka (1957) formally showed that the effect of inelastic scattering processes on the elastic scattering by crystals could be taken into account by the addition of an imaginary part $iV'(\boldsymbol{r})$ to the potential. The magnitude of $V'(\boldsymbol{r})$ is typically less than or equal to one-tenth of the real part of the potential (Humphreys and Hirsch 1968). From the discussion of absorption given in §5.1 it will be clear that $V'(\boldsymbol{r})$ is a function of the objective aperture size. The theory outlined below is an approximate phenomenological approach to a complex situation, and it does not properly consider the small-angle inelastically scattered electrons which pass through the objective aperture.

However, in practice the phenomenological theory is found to work extremely well, both qualitatively and quantitatively, and it can account for a very wide range of experimental observations.

Since the imaginary part of the potential, $V'(\boldsymbol{r})$, is associated with the crystal lattice, it can be expanded as a Fourier series based on the reciprocal lattice in a similar manner to the expansion of the real part of the potential (see equation (4.3)). We can then take absorption into account by modifying the elastic scattering theory (equations (4.11) to (4.51)) so that

$$\begin{aligned} V(\boldsymbol{r}) &\rightarrow V(\boldsymbol{r}) + \mathrm{i}V'(\boldsymbol{r}) \\ V_g &\rightarrow V_g + \mathrm{i}V_g' \\ U_g &\rightarrow U_g + \mathrm{i}U_g'. \end{aligned} \tag{5.1}$$

Virtual inelastic scattering processes give rise to a very small real part addition to the potential $\Delta V(\boldsymbol{r})$ (see §4.1). For convenience of notation we incorporate $\Delta V(\boldsymbol{r})$, ΔV_g and ΔU_g into $V(\boldsymbol{r})$, V_g and U_g, respectively, on the right-hand side of equations (5.1).

If the potential in the Schrödinger equation (equation (4.11)) is made complex it follows that the wavevectors $\boldsymbol{k}^{(j)}$ inside the crystal will be complex, i.e.

$$\boldsymbol{k}^{(j)} \rightarrow \boldsymbol{k}^{(j)} + \mathrm{i}\boldsymbol{q}^{(j)}. \tag{5.2}$$

From equation (4.25) the total wavefunction of the fast electron within the crystal is then given by

$$\Psi(\boldsymbol{r}) = \sum_j \alpha^{(j)} \sum_g C_g^{(j)} \exp\left[2\pi\mathrm{i}(\boldsymbol{k}^{(j)} + \boldsymbol{g}).\boldsymbol{r}\right] \exp\left(-2\pi\boldsymbol{q}^{(j)}.\boldsymbol{r}\right). \tag{5.3}$$

Thus each Bloch wave is exponentially attenuated as it propagates through the crystal, as physically expected. It follows from the boundary conditions (§4.6) that the direction of $\boldsymbol{q}^{(j)}$ is along the inward surface normal for all j. In the absence of absorption each Bloch wave excitation amplitude in the crystal $\alpha^{(j)}$ is a constant (equal to $C_0^{(j)*}$, see §4.6). The effect of absorption is to replace $\alpha^{(j)}$ by an exponentially attenuated amplitude $\alpha^{(j)}(z)$ where

$$\alpha^{(j)}(z) = \alpha^{(j)} \exp\left(-2\pi q^{(j)} z\right) \tag{5.4}$$

where the origin of z is taken at the top surface of the crystal and z lies along the surface normal.

We have seen that for purely elastic scattering in a general non-centrosymmetric crystal $U(\boldsymbol{r})$ is real, and therefore $U_g = U_{-g}^*$ and $\boldsymbol{A}$ is Hermitian (§4.9). Since the imaginary part of the potential $\mathrm{i}U'(\boldsymbol{r})$ is purely imaginary, we must have $U_g' = U_{-g}^{*\prime}$ and therefore for the complex optical potential:

$$(U_g + \mathrm{i}U_g') \neq (U_{-g} + \mathrm{i}U_{-g}')^*.$$

Hence the matrix $\boldsymbol{A}$(abs), for an absorbing crystal, given by setting equation (5.1) in equations (4.43) and (4.44), is a complex general matrix. Obtaining eigenvalues and eigenvectors of this matrix is a problem of some difficulty but standard computer programs are available.

The problem simplifies if the crystal has a centre of symmetry, since then $U_g = U_{-g}$, $U_g' = U_{-g}'$ and

$$(U_g + \mathrm{i}U_g') = (U_{-g} + \mathrm{i}U_{-g}').$$

Thus $\boldsymbol{A}$(abs) is complex symmetric, the eigenvalues are complex and the eigenvector matrix $\boldsymbol{C}$ is complex orthogonal.

For electron diffraction calculations which require high precision, for example in the accurate determination of crystal potentials and charge densities, the full complex matrix should be diagonalised (e.g. Hewat and Humphreys 1974). This is time-consuming on a computer, however, and for the vast majority of applications it is a very good approximation to treat absorption by a perturbation method since, as mentioned earlier, $V'(\boldsymbol{r})$ is typically $\leqslant 0{\cdot}1\, V(\boldsymbol{r})$. A formal non-degenerate perturbation treatment of absorption is given by Metherell (1975). In particular cases degenerate or nearly degenerate eigenvalues occur (see §5.9), and it is then necessary to use degenerate perturbation theory (see Sprague and Wilkens 1970) or to diagonalise the complex matrix as described above.

The formal perturbation treatment of absorption is equivalent to, and yields the same result as, the treatment given below in which the approximations made are more easily seen. Setting equations (5.1) and (5.2) in (4.18) gives

$$\{K^2-[(\boldsymbol{k}+\boldsymbol{g})^2-q^2+2\mathrm{i}\boldsymbol{q}.(\boldsymbol{k}+\boldsymbol{g})]\}C_g+\sum_{h\neq g} U_{g-h}C_h+\mathrm{i}\sum_h U_{g-h}'C_h=0. \qquad (5.5)$$

In perturbation theory the wavefunction is unchanged to first order, hence the C_g in equations (5.5) and (4.18) are the same. Subtracting equation (4.18) from equation (5.5) gives

$$-2\mathrm{i}\boldsymbol{q}.(\boldsymbol{k}+\boldsymbol{g})C_g+\mathrm{i}\sum_h U_{g-h}'C_h=0 \qquad (5.6)$$

where we have assumed that $q^2\ll(\boldsymbol{k}+\boldsymbol{g})^2$ for a small perturbation. In the symmetrical Laue case $\boldsymbol{q}$ is along the surface normal (defined as the z direction) and $\boldsymbol{g}$ is perpendicular to this, hence $\boldsymbol{q}.\boldsymbol{g}=0$. Also $\boldsymbol{q}.\boldsymbol{k}=qk_z\approx qK_z$ to a very good approximation. Thus equation (5.6) is, for the jth Bloch wave,

$$2q^{(j)}K_zC_g^{(j)}=\sum_h U_{g-h}'C_h^{(j)}. \qquad (5.7)$$

Multiplying both sides by $C_g^{(j)*}$, summing over g and assuming that the $C_g^{(j)}$ are normalised (equation (4.46)) gives

$$q^{(j)}=\frac{1}{2K_z}\sum_g\sum_h C_g^{(j)*}U_{g-h}'C_h^{(j)}. \qquad (5.8)$$

Equation (5.8) in matrix form is

$$q^{(j)}=\frac{1}{2K_z}(C_0^{(j)*}\ C_g^{(j)*}\ \ldots)\begin{bmatrix} U_0' & U_{-g}' & \ldots \\ U_g' & U_0' & \ldots. \\ . & . & \\ . & . & \\ . & . & \end{bmatrix}\begin{bmatrix} C_0^{(j)} \\ C_g^{(j)} \\ . \\ . \\ . \end{bmatrix}. \qquad (5.9)$$

Hence $q^{(j)}$, the imaginary part of the wavevector for the jth Bloch wave, is easily calculated from the eigenvectors and the matrix of the $U'(\boldsymbol{r})$ Fourier coefficients.

5.3. Anomalous absorption and anomalous transmission

Equations (5.3) and (5.4) show that the (amplitude) absorption coefficient of the jth Bloch wave is $2\pi q^{(j)}$ and from equation (5.9) it is clear that there is a different value of $q^{(j)}$ for each Bloch wave. Hence some Bloch waves are more strongly absorbed than average and others are more strongly transmitted, which gives rise

to so-called anomalous absorption and anomalous transmission, respectively. The physical reason for anomalous absorption is that the periodic imaginary part of the potential $V'(\boldsymbol{r})$ has maxima in those regions of the unit cell in which inelastic scattering is strongest. A consideration of the basic inelastic scattering mechanisms (see §5.1) shows that phonon scattering is strongly localised at the atoms, single-electron excitations are relatively weakly localised at the atoms and plasmon scattering is not localised at all to first order. Hence we expect $V'(\boldsymbol{r})$ to have maxima at atom sites. Clearly those Bloch waves which have maximum electron density at atom sites will be strongly absorbed and those which have maximum density between atoms will be weakly absorbed.

This effect is most clearly illustrated by considering the two-beam approximation in a centrosymmetric crystal of simple structure set at an exact Bragg reflecting position. Figure 15 shows the reflecting planes with the regions of maximum inelastic scattering drawn around each atom site. From equations (4.25) and (4.35) the wavefunctions of Bloch waves 1 and 2 are

$$\psi^{(1)}(\boldsymbol{r}) = 2^{1/2} \cos(\pi \boldsymbol{g}.\boldsymbol{r}) \exp[2\pi i(\boldsymbol{k}^{(1)} + 0{\cdot}5\boldsymbol{g}).\boldsymbol{r}] \tag{5.10}$$

$$\psi^{(2)}(\boldsymbol{r}) = -i2^{1/2} \sin(\pi \boldsymbol{g}.\boldsymbol{r}) \exp[2\pi i(\boldsymbol{k}^{(2)} + 0{\cdot}5\boldsymbol{g}).\boldsymbol{r}]. \tag{5.11}$$

The electron density in each Bloch wave is

$$|\psi^{(1)}(\boldsymbol{r})|^2 = 2\cos^2(\pi g x) \tag{5.12}$$

$$|\psi^{(2)}(\boldsymbol{r})|^2 = 2\sin^2(\pi g x) \tag{5.13}$$

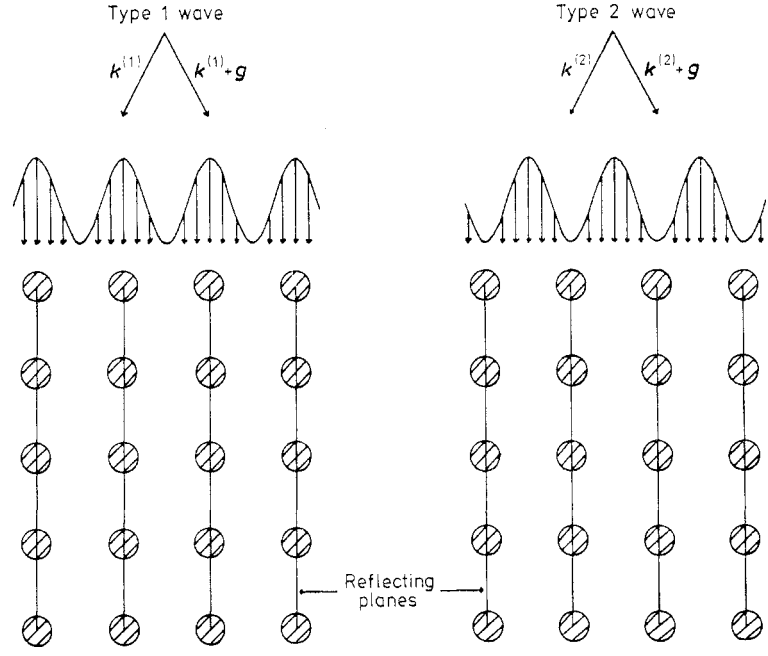

Figure 15. Schematic diagram illustrating the nature of Bloch wave absorption in the two-beam case at the Bragg reflecting position. Regions around atoms where the inelastic scattering is a maximum are shown shaded. The Bloch wave current flow is parallel to the reflecting planes. The type 1 wave is absorbed more than the type 2 wave, which 'channels' between the atoms.

where the x coordinate is defined parallel to $\boldsymbol{g}$. The origin of $\boldsymbol{r}$ is at a centre of symmetry (see §4.7) which we choose to be an atomic site in the simple crystal structure. Equations (5.10) and (5.12) show that the current flow of Bloch wave 1 is in the direction $(\boldsymbol{k}^{(1)}+0{\cdot}5\boldsymbol{g})$, which is exactly parallel to the reflecting planes when the crystal is at the Bragg position. The electron probability has a $\cos^2(\pi gx)$ modulation normal to the reflecting planes, i.e. a maximum at the atom sites (see figure 15). Equations (5.11) and (5.13) show that wave 2 is also a standing wave in the x direction and a travelling wave in the z direction with current flow in the direction $(\boldsymbol{k}^{(2)}+0{\cdot}5\boldsymbol{g})$ again exactly parallel to the reflecting planes. For wave 2, however, the electron probability is proportional to $\sin^2(\pi gx)$, i.e. it has minima at the atom sites (figure 15). Since the inelastic scattering is a maximum around atom sites it is clear that the absorption of wave 1 is above average and that of wave 2 is below average. A modified form of figure 15 was first used by Hashimoto *et al* (1962). It should be noted that the ordered labelling scheme used in the present review (see §4.7) and in many recent papers differs from that used by Hashimoto *et al* (1962), in that Bloch wave 1 of Hashimoto *et al* (1962) is here labelled Bloch wave 2 and vice versa.

q_0, the imaginary part of the wavevector corresponding to mean absorption, is given by setting $U_g'=0$ for all g except $g=0$ in equation (5.8) or (5.9). This gives, using (4.46),

$$q_0=U_0'/2K_z. \tag{5.14}$$

The (amplitude) mean absorption coefficient is, using equation (5.4),

$$\kappa_0=2\pi q_0=\pi U_0'/K_z \tag{5.15}$$

the intensity absorption coefficient being $\mu_0=4\pi q_0$. The mean absorption length ξ_0' is defined as

$$\xi_0'=K_z/U_0' \tag{5.16}$$

so that the mean absorption coefficient for amplitude is, using equation (4.15),

$$\kappa_0=\frac{\pi}{\xi_0'}=\frac{2\pi me}{h^2K_z}V_0'. \tag{5.17}$$

At an exact Bragg position and using the two-beam approximation, equations (5.8) or (5.9) give, using equation (4.35),

$$q^{(1)}=\frac{1}{2K_z}(U_0'+U_g') \tag{5.18}$$

$$q^{(2)}=\frac{1}{2K_z}(U_0'-U_g'). \tag{5.19}$$

For simple crystal structures, and taking the origin at an atom site, the Fourier coefficients of $U'(\boldsymbol{r})$ are all positive and decrease with increasing $\boldsymbol{g}$. It is clear therefore from equations (5.18) and (5.19) that, on the two-beam approximation, wave 1 is strongly absorbed and wave 2 is well transmitted. It is conventional to define an anomalous absorption length ξ_g', by comparison with equations (5.16) and (4.36), as

$$\xi_g'=K_z/U_g'. \tag{5.20}$$

The amplitude absorption coefficient of Bloch waves 1 and 2 at the Bragg position is then

$$\kappa^{(j)} = \pi\left(\frac{1}{\xi_0'} \pm \frac{1}{\xi_g'}\right). \tag{5.21}$$

5.4. The orientation which maximises the penetration

In an amorphous material the transmitted intensity is not a function of orientation and it is given simply by

$$I(t) = I_0 \exp(-\mu_0 t) \tag{5.22}$$

where I_0 is the incident intensity.

In a crystal, the transmitted intensity is a sensitive function of orientation owing to diffraction. In electron microscopy it is often desirable to study as thick a specimen as possible in order to minimise surface effects. It is therefore necessary to use the crystal orientation, relative to the incident beam direction, which gives the maximum transmitted electron intensity.

The intensity of the gth diffracted beam from a crystal of thickness t is, from equations (4.33) and (5.4),

$$I_g(t) = \left| \sum_j C_0^{(j)*} C_g^{(j)} \exp(2\pi i k_z^{(j)} t) \exp(-2\pi q^{(j)} t) \right|^2. \tag{5.23}$$

For small crystal thicknesses, at least two Bloch waves normally significantly contribute to $I_g(t)$. As t increases, the number of waves which make a substantial contribution to $I_g(t)$ decreases due to the term $\exp(-2\pi q^{(j)} t)$. For thick crystals only one wave effectively contributes to $I_g(t)$ at a given orientation, the wave with the smallest $\mu^{(j)}$ value for that orientation. Let this wave be wave i, then for a thick crystal equation (5.23) reduces to

$$I_g(t) = |C_0^{(i)}|^2 |C_g^{(i)}|^2 \exp(-4\pi q^{(i)} t). \tag{5.24}$$

The orientation which maximises the transmitted intensity for the gth diffracted beam is given by the orientation for which equation (5.24) is a maximum. As an example we take the particular case of the 'bright-field' forward scattered beam with $g = 0$. Equation (5.24) is then

$$I_0(t) = |C_0^{(i)}|^4 \exp(-4\pi q^{(i)} t). \tag{5.25}$$

Figure 16 plots values of the excitation amplitude $\alpha^{(i)} = C_0^{(i)*}$ and of the absorption eigenvalue $q^{(i)}$ as a function of orientation for 100 keV electrons incident upon copper. Bloch wave 1 is not included since it is very strongly absorbed at all orientations, and in thick crystals it does not contribute significantly to the transmitted intensity.

From figure 16, the minimum values of $q^{(j)}$ occur for wave 2 when the crystal is at the Bragg position for the (200), (600), etc, reflections. (The $q^{(j)}$ values are periodic with Bragg deviation, as can be shown from equation (5.8) (see Metherell and Fisher 1969).) However, from equation (5.25), for good transmission the excitation of this Bloch wave $\alpha^{(2)} = C_0^{(2)*}$ ($= C_0^{(2)}$ in centrosymmetric copper) must also be large. In this case $C_0^{(2)}$ is largest between the (200) and (400) positions, and the orientation of maximum transmission will occur between the first and second Bragg reflecting positions. In very thick crystals the absorption term is dominant

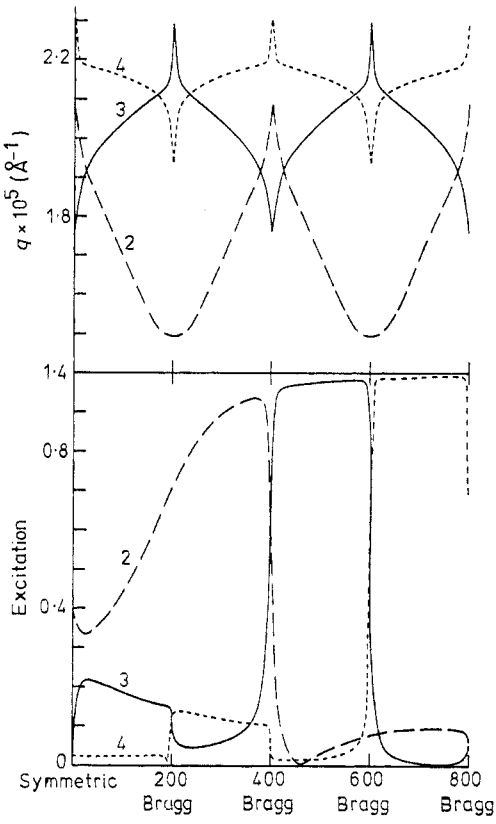

Figure 16. Values of the absorption eigenvalue $q^{(i)}$ and the excitation amplitude $\alpha^{(i)}$ for Bloch waves 2, 3 and 4 as a function of orientation for 100 keV electrons incident upon copper (from Humphreys *et al* (1971), by courtesy of The Philosophical Magazine).

and the position of best transmission is with the crystal set only slightly positive of the first-order Bragg position. This is confirmed in figure 17 which plots the calculated transmitted intensity, for the bright-field and several dark-field beams, as a function of the orientation of the incident beam with respect to the crystal.

Figures 16 and 17 are typical of results obtained for the majority of materials and incident electrons of energy 100 keV or less, for which the orientation which maximises the penetration is slightly positive of the first-order Bragg position for the bright-field beam, and at their respective Bragg positions for the dark-field beams.

With increasing electron energy above 100 keV, the absorption of wave 2 increases and its excitation decreases while waves 3 and 4 increase in importance. Even-numbered Bloch waves generally have absorption minima at the first, third, etc, Bragg positions, and odd-numbered waves have minima at the symmetry position, second, fourth, etc, Bragg positions. Since successively numbered waves have alternately minimum and maximum absorption coefficients at a given Bragg position (with minor exceptions), the orientations which give best transmission at 100 keV become positions of poor transmission at higher voltages. The best orientations for maximising the penetration using 1 MeV electrons have been investigated in some detail both experimentally and theoretically, and tables giving these orientations

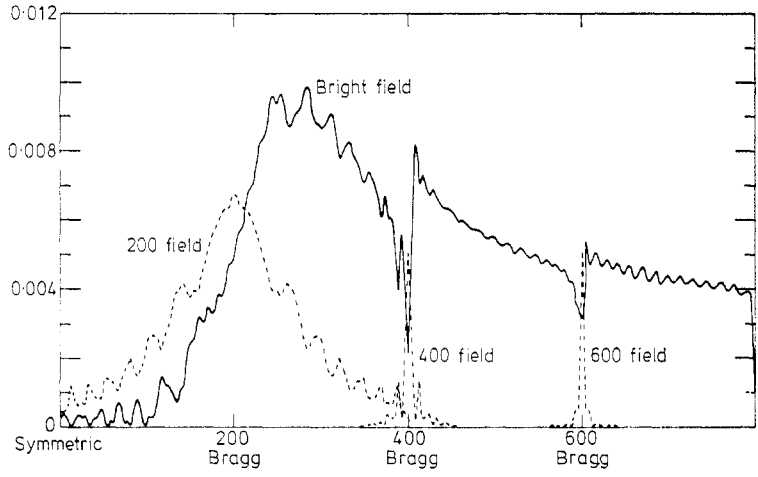

Figure 17. The transmitted intensity, for bright-field and various dark-field beams, as a function of orientation for 100 keV electrons incident upon copper 2000 Å thick (from Humphreys *et al* (1971), by courtesy of The Philosophical Magazine).

have been published by Humphreys *et al* (1971). An electron micrograph of a bent crystal is shown in figure 18 (plate) which illustrates the variation of intensity with orientation for a number of different Bragg reflections excited. The orientation which maximises the penetration for incident electron energies up to 10 MeV has been studied theoretically by Humphreys (1972) and experimental studies up to 3 MeV have been made by Fujita *et al* (1974) and Rocher *et al* (1974). As shown in figure 19 for electrons incident upon aluminium, the orientation for good penetration is a function of the incident electron energy. Incident energies greater than about 10 MeV are unlikely to be useful for diffraction work owing to the effects of bremsstrahlung and radiation displacement damage on the specimen. The optimum energy for maximising the penetration in light atomic weight materials is about 3 MeV, and rather less than this for heavy materials (see Humphreys 1972).

5.5. Back-scattering of electrons

So far we have considered the scattering of fast electrons by crystals with particular reference to electron transmission, and the back-scattering of electrons has been ignored. If the specimen is thin, as used in transmission electron microscopy, it is a valid approximation to neglect the back-scattered electrons. However as the specimen thickness increases the back-scattered intensity increases until for solid specimens the back-scattered intensity is large (for example, over 30% of incident 20 keV electrons are back-scattered from solid copper).

The traditional method of calculating electron back-scattering is to use Monte Carlo methods with appropriate scattering models. These methods ignore diffraction and hence essentially are only applicable to 'amorphous solids'. However Monte Carlo techniques have yielded valuable information on electron back-scattering, x-ray production, etc, from a wide range of materials (see Heinrich *et al* 1976).

In this review we are concerned with scattering by crystals, and hence with diffraction effects, and we shall not consider 'amorphous solid' Monte Carlo methods further. Hirsch *et al* (1962) predicted that when electrons were incident upon crystals

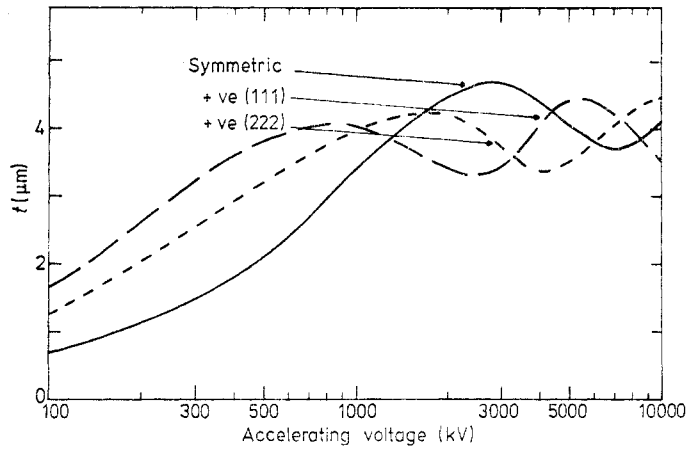

Figure 19. Electron penetration in aluminium as a function of the accelerating voltage for various orientations of the crystal (from Humphreys (1972), by courtesy of The Philosophical Magazine).

the intensity of the back-scattered electrons (and also x-rays) should depend upon the orientation of the crystal relative to the incident beam. This was confirmed experimentally by Duncumb (1962) and Hall (1966) for thin crystal specimens. Diffraction effects were first observed in back-scattered electrons from bulk specimens by Coates (1967) who observed weak Kikuchi-like patterns superimposed on scanning electron micrographs. He used these orientation-dependent patterns to determine the crystallographic orientation of the specimen. The patterns are formed because the back-scattered electron intensity is a function of the angle of incidence of the beam. Booker *et al* (1967) qualitatively interpreted this orientation dependence in terms of the anomalous absorption effect (see §5.3). The patterns are known as Coates patterns, or as electron channelling patterns, and a typical example is shown in figure 20 (plate).

A qualitative explanation of the orientation dependence of back-scattered electrons is as follows. For simplicity we assume the crystal is oriented near a Bragg reflecting position and make the two-beam approximation. Within the crystal the incident electron density is as shown schematically in figure 15. The main back-scattering mechanism is phonon scattering, which is localised at the atomic sites, hence wave 1 is back-scattered more strongly than wave 2. With the crystal set slightly off the Bragg position in the $s<0$ sense the type 1 wave is preferentially excited, while when set with $s>0$ the type 2 wave is preferentially excited. Hence there are more back-scattered electrons on the $s<0$ side of the Bragg position than on the $s>0$ side. This behaviour is opposite to that which occurs with transmitted electrons (see §5.4) and explains the observations of Duncumb (1962) that dark bend contours observed using transmitted electrons correspond to bright bend contours observed using back-scattered electrons.

A complete quantitative theory of back-scattered electrons should include diffraction effects (i.e. multiple elastic scattering), multiple inelastic scattering and energy losses. Such a theory has not yet been formulated, although considerable progress has been made. Back-scattering theories for perfect crystals which take into account diffraction but ignore energy losses and only deal crudely with multiple inelastic scattering have been developed by Hirsch and Humphreys (1970), Vicario *et al*

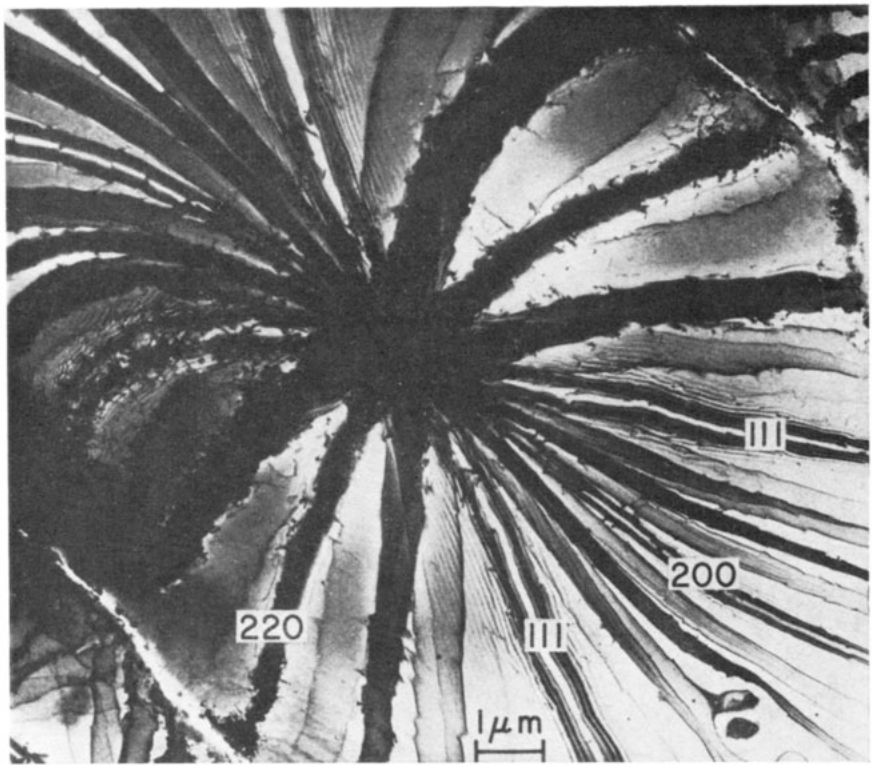

Figure 18. Bright-field bend contours at a [110] zone axis in gold (1 MeV incident electrons). Note how the optimum orientations for maximising the penetration are a function of the Bragg reflection excited (from Humphreys *et al* (1971), by courtesy of The Philosophical Magazine).

(1970) and Reimer *et al* (1971). For a comparison of these theories see Spencer *et al* (1972). The above theories account qualitatively very well for the observed dependence of the intensity of back-scattered electrons upon the orientation of the crystal with respect to the incident beam. The above theories were generalised to include back-scattering from imperfect crystals by Clarke and Howie (1971) and Spencer *et al* (1972).

A theory has also been developed which takes into account diffraction and treats multiple inelastic scattering more accurately, but ignores energy losses (Spencer and Humphreys 1973). This theory agrees quantitatively with experiment. Also a theory has been developed which includes diffraction and energy losses, while still treating multiple inelastic scattering crudely (Sandström *et al* 1974). Further details of both the theory and applications of electron channelling patterns are given in the article by Booker and Humphreys (1975).

The Coates patterns, or electron channelling patterns, described above result from the variation of back-scattered electron intensity as a function of the angle of incidence of the incident beam. The orientation dependence arises from diffraction of the incident beam before back-scattering occurs. A different type of orientation dependence has been observed by Venables and Harland (1973). In their electron back-scattering patterns the crystal is in a fixed orientation relative to the incident beam and angular variations in intensity of the back-scattered electrons are observed. These patterns, as distinct from 'electron channelling patterns', arise from diffraction after back-scattering has occurred.

5.6. The reciprocity theorem

The reciprocity principle was originally proved by Helmholtz for the case of the propagation of sound waves. The principle essentially states that if a certain signal is detected at a point A when a source is placed at another point B, then the same signal in amplitude and phase would be detected at B if the source were placed at A. von Laue (1935) proved the above statement for the case of electron diffraction and elastic scattering, and Pogany and Turner (1968) extended the theory to include inelastically scattered electrons with small energy loss, for which case there is a reciprocity of intensities rather than of amplitudes.

This elegant and important theorem has found considerable application in electron microscopy in recent years in the interpretation of images formed using the scanning transmission electron microscope (STEM). Cowley (1969) and Crewe and Wall (1970) have shown using the reciprocity theorem that under the appropriate conditions STEM images should be similar to the corresponding images obtained using TEM (transmission electron microscopy). However, STEM and TEM images are not usually identical for a variety of reasons: in the normal modes of operation of STEM the incident and collected angular cones of electrons do not correspond in a reciprocal manner with those in TEM (Howie 1972, Booker *et al* 1973); in thick specimens there is appreciable inelastic scattering; in the imaging of defects, if the column approximation (see §6.4) breaks down then reciprocity is not easily applicable (Humphreys and Drummond 1976a). Thus although the reciprocity principle is very useful, its correct application requires care.

5.7. Convergent-beam electron diffraction

One method of observing the variation of diffracted intensity as a function of the

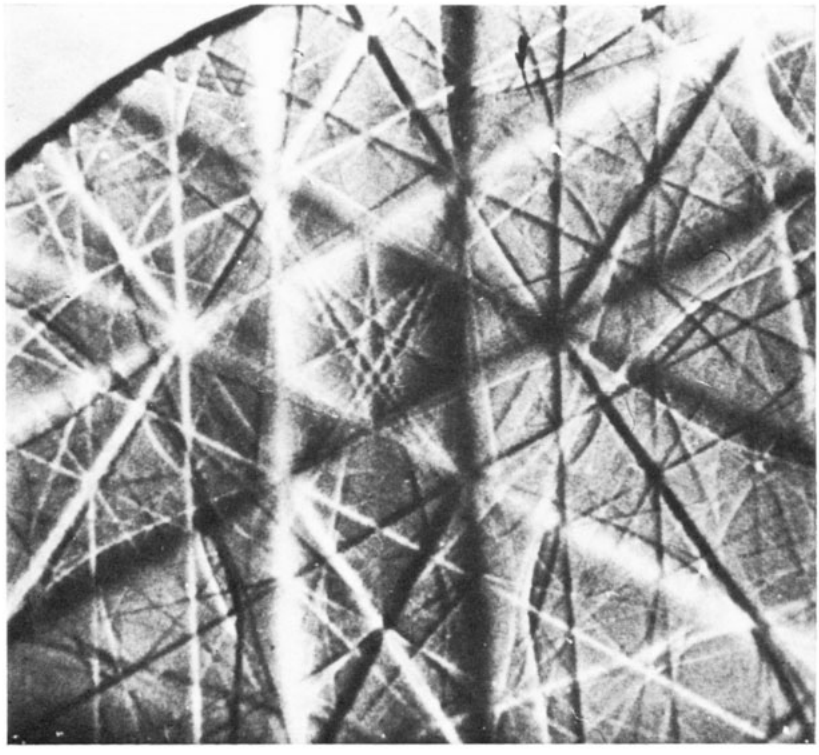

Figure 20. Electron channelling pattern for 30 keV electrons incident on a silicon crystal with a (111) surface normal. The pattern has been differentiated electronically to enhance the contrast.

angle of incidence, as plotted theoretically in figure 17, is by using convergent-beam electron diffraction (CBED). In this method an electron beam is focused onto the specimen (as distinct from the reasonably parallel beam used in normal transmission electron microscopy). If the incident beam is defined by a circular aperture (usually placed in the condenser lens system), each spot in the diffraction pattern is spread into a circular disc. Each point in a disc corresponds to a particular angle of incidence, so that the variation of intensity across each disc represents the variation of intensity in each diffracted beam as a function of the angle of incidence.

The CBED technique was first used by Kossel and Mollenstedt (1939) and has been developed by Hoerni (1950), Goodman and Lehmpfuhl (1964) and Cockayne *et al* (1967). The importance of the technique lies in the high angular resolution of 10^{-4} rad observable in each diffracted disc, a large number of diffracted beam discs being observable simultaneously.

Applications of the CBED technique include determining Fourier coefficients of the crystal potential (Goodman and Lehmpfuhl 1967), determining crystal point groups and space groups (Goodman and Lehmpfuhl 1968, Gjønnes and Moodie 1965, Buxton *et al* 1976), measuring crystal thicknesses to an accuracy of one unit cell (Goodman and Moodie 1974) and measuring lateral changes in lattice parameters (Jones *et al* 1977). The CBED method has recently been combined with the critical voltage technique (§5.9) which yields particularly accurate values of Fourier coefficients of the crystal potential (Moodie *et al* 1978). An example of a CBED pattern is shown in figure 21 (plate).

5.8. Zone axis patterns

CBED patterns are formed using a convergent beam incident upon a flat specimen and they are observed in the diffraction plane. An alternative method of recording a rocking curve (i.e. an intensity against angle of incidence curve) is to use a parallel beam incident upon a uniformly bent crystal and to observe in the image plane. As the crystal bends through Bragg reflecting positions the image (dark-field or bright-field) is crossed by 'bend contours', also known as 'extinction contours'. The image of a particular diffracted beam is similar to that of the corresponding CBED disc, except that the bent crystal image has lower angular resolution than that of a CBED pattern. The reason for this is that the 'parallel' incident beam required for the bent crystal method in practice must have a finite convergence which limits the angular resolution attainable.

If the beam is incident along a zone axis and the crystal is bent in a dome or cup shape then bend contour zone axis patterns (ZAPS) are produced (see figure 22 (plate)). Such patterns contain information on the projected crystal potential and the use of ZAPS images has been termed 'real-space crystallography' (Steeds *et al* 1976), by comparison with x-ray crystallography in which information is obtained from a reciprocal-space diffraction pattern.

Electron microscopy and diffraction methods, such as ZAPS, lattice imaging and CBED, have some significant advantages over x-ray diffraction techniques. In particular, x-ray diffraction methods use relatively large crystals and the structure obtained is a structure averaged over the diffracting volume of the crystal. In electron microscopy, on the other hand, highly magnified images can be formed of thin crystals so that the structure is 'projected' in the z direction only, and any structural defects are apparent in the image. In the diffraction mode, CBED patterns can be formed using

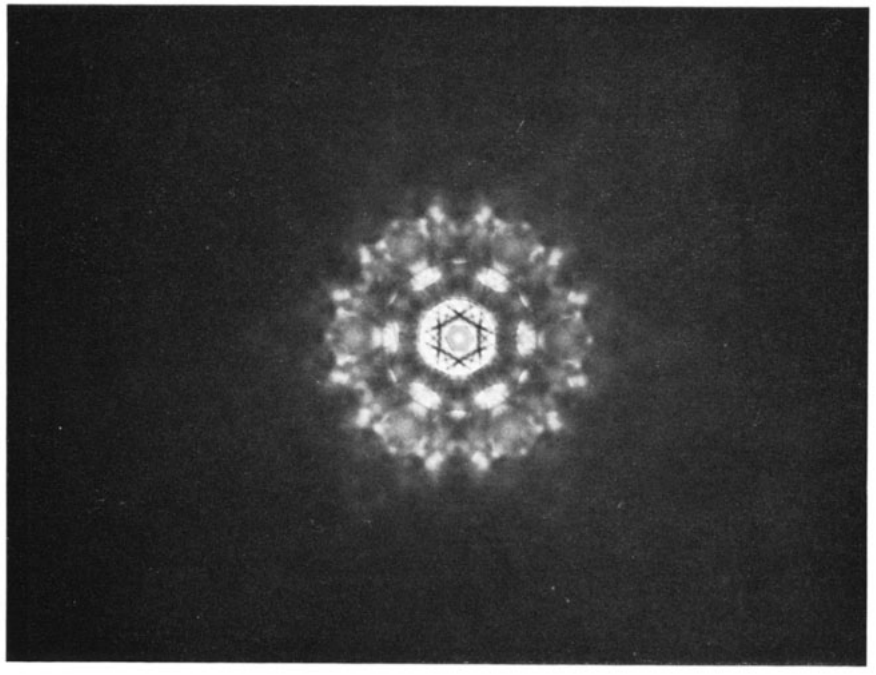

Figure 21. [0001] convergent-beam zone axis pattern (100 keV electrons) of a Laves phase precipitate (approximate composition $Fe_{1.3}Cr_{0.5}Ni_{0.1}Si_{0.1}Mo$) in a sample of 316 stainless steel. (Courtesy of N Evans and J W Steeds.)

electron spot sizes of very small diameter and hence only a very small diffracting volume of crystal may be used which, by observing the image, may be chosen to be free of defects. Hence electron microscopy and diffraction may be used for the structural analysis of precipitates, crystal phases, etc, on a much finer scale than is possible using x-ray diffraction methods.

5.9. The critical voltage effect

The critical voltage effect is one of the more remarkable discoveries in electron diffraction. If a crystal is set at a Bragg reflecting position normally one expects the diffracted beam intensity to be strong, unless the crystal thickness is an integral number of extinction distances, owing to the constructive interference of waves scattered in the diffracted beam direction. However, for a particular incident electron accelerating voltage, known as the critical voltage, V_c, the diffracted beam intensity is very small, due to destructive rather than constructive interference. The critical voltage is a function of the material, Bragg reflection and temperature used.

This effect was discovered in Japan about ten years ago (Nagata and Fukuhara 1967, Uyeda 1968, Watenabe *et al* 1968). It was quickly realised (see Watenabe *et al* 1968) that the critical voltage is very sensitive to the first-order Fourier coefficient of the crystal potential, V_g, and hence can be used to determine V_g very accurately (to better than 1%). Comparison of experimental critical voltage determined V_g values with theoretical free-atom values, gives information on the ionicity of atoms in a crystal (Watenabe and Terasaki 1972), covalent bonding charge redistributions (Hewat and Humphreys 1974) and band structures in metals (Smart and Humphreys 1978).

The sensitivity of V_g values to the critical voltage can also be used to measure Debye temperatures, and the degree of long-range and short-range order in alloys (Lally *et al* 1972), and to measure alloy compositions (Butler 1972).

The effect essentially arises because of an accidental degeneracy of two Bloch waves. The simplest case to consider is the minimising of a second-order reflection due to this effect. In general, at any voltage, the intensity of a second-order reflection, I_{2g}, is given by (using equation (5.23)):

$$I_{2g}(t) = \left| \sum_j C_0^{(j)*} C_{2g}^{(j)} \exp(2\pi i k_z^{(j)} t) \exp(-2\pi q^{(j)} t) \right|^2. \tag{5.26}$$

For a crystal set at the second-order reflecting position, Bloch waves 2 and 3 normally have the strongest excitation amplitudes, and wave 1 the next strongest. The excitations of all other Bloch waves are very small. Also waves 2 and 3 are usually the least absorbed waves, wave 1 being the most strongly absorbed. Equation (5.26) can therefore be written in the form

$$I_{2g}(t) = \left| \sum_{j=2,3} C_0^{(j)*} C_{2g}^{(j)} \exp(2\pi i k_z^{(j)} t) \exp(-2\pi q^{(j)} t) + \Delta \right|^2 \tag{5.27}$$

where Δ represents the contributions of all waves other than 2 and 3. Because of anomalous absorption, Δ is very small for reasonably thick crystals.

Below a certain accelerating voltage, the critical voltage, wave 3 is antisymmetric and wave 2 symmetric. The kinetic energies of the two waves are different and hence $k_z^{(2)} \neq k_z^{(3)}$. As the accelerating voltage is raised, the kinetic energies of waves 2 and 3 become more nearly equal until at the critical voltage, V_c, the kinetic energies are identical and $k_z^{(2)} = k_z^{(3)}$. This is an accidental degeneracy of the two Bloch

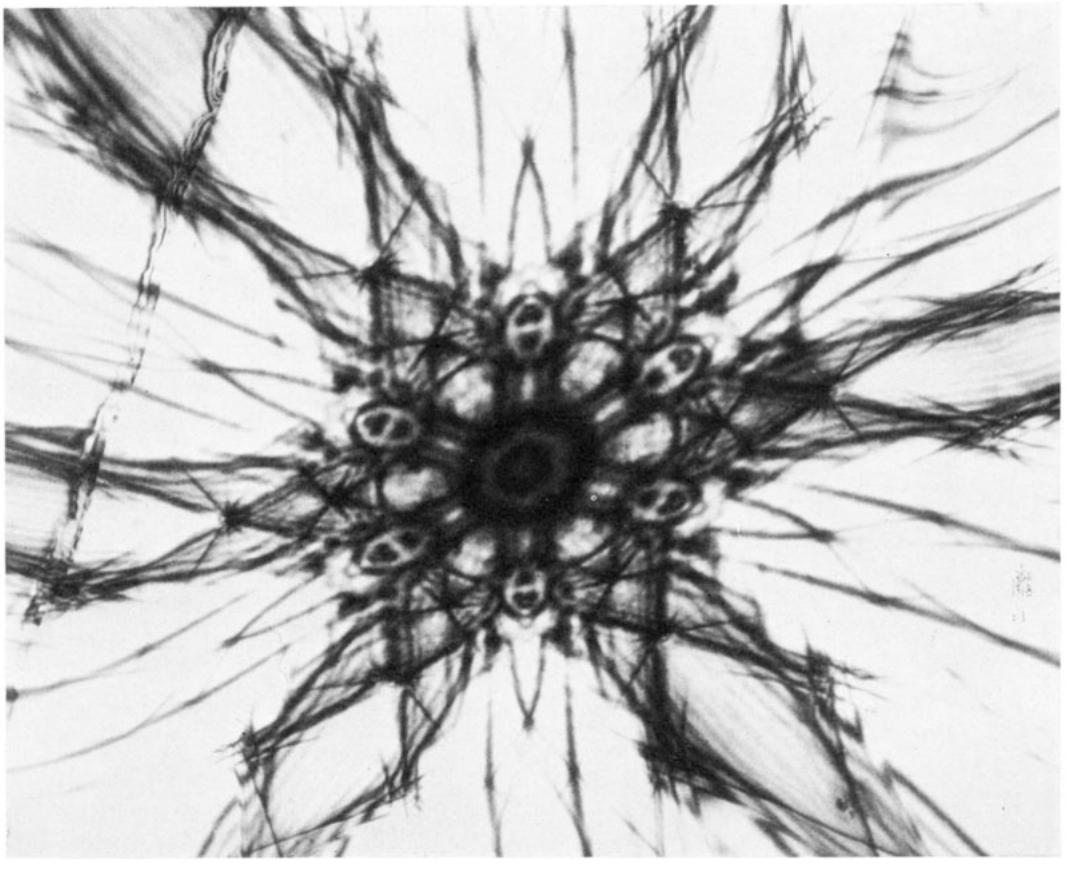

Figure 22. [0001] bend contour zone-axis pattern of TiS_2. 600 keV incident electrons. (Courtesy of K K Fung and J W Steeds.)

waves. On passing through the critical voltage the symmetries of waves 2 and 3 interchange and the dispersion surface branches separate and are non-degenerate again.

At $V = V_c$, $k_z^{(2)} = k_z^{(3)}$, $C_0^{(2)} C_{2g}^{(2)} \simeq -C_0^{(3)} C_{2g}^{(3)}$ and $q^{(2)} \simeq q^{(3)}$. Hence from equation (5.27) waves 2 and 3 destructively interfere and $I_{2g}(t)$ is very small. More complicated critical voltage effects occur in two-dimensional diffraction situations (Steeds *et al* 1976) but in each case the cause is due to an accidental degeneracy of Bloch waves (Buxton and Loveluck 1977).

The accidental degeneracy theoretically occurs at a precise value, V_c, of the electron accelerating voltage. The utility of the effect depends upon the experimental accuracy with which V_c can be determined. The most accurate method appears to be the one recently proposed by Moodie *et al* (1978), in which a Kikuchi line within a convergent-beam electron diffraction disc is observed at the critical voltage. It is expected that the critical voltage method will continue to be developed and that the important problem of measuring electron densities and lattice potentials in crystals will be studied with increasing precision on a wide variety of crystals.

5.10. Inelastic scattering and resonance errors

For elastic scattering, the Laue condition for a diffracted maximum is given by equation (3.3), i.e.

$$\boldsymbol{k}' - \boldsymbol{k} = \boldsymbol{g}. \tag{3.3}$$

As discussed in §3.5, the Laue condition strictly applies for a perfect, infinite crystal only. For a finite crystal we have finite diffracted intensity when

$$\boldsymbol{k}' - \boldsymbol{k} = \boldsymbol{g} + \boldsymbol{s} \tag{3.6}$$

where $\boldsymbol{s}$ is a small vector in reciprocal space.

For inelastic scattering the situation is similar. For an infinite crystal we must have

$$\boldsymbol{k}' - \boldsymbol{k} = \boldsymbol{q} \tag{5.28}$$

where $\boldsymbol{k}$ and $\boldsymbol{k}'$ are the incident and the scattered electron wavevectors, respectively, and $-\boldsymbol{q}$ is the wavevector of the crystal excitation created (plus a reciprocal lattice vector if an *umklapp* process is involved). For a finite crystal we have

$$\boldsymbol{k}' - \boldsymbol{k} = \boldsymbol{q} + \delta\boldsymbol{k} \tag{5.29}$$

where $\delta\boldsymbol{k}$ is known as a resonance error. Hence the wavevector change of the fast electron will not in general be exactly opposite to that of the crystal excitation created. $\delta\boldsymbol{k}$ for inelastic scattering is clearly analogous to $\boldsymbol{s}$ for elastic scattering. In addition, for a crystal of finite thickness $\boldsymbol{q}$ is not continuous but discrete, since in a crystal of thickness t the allowed wavevector components q_z are given by n/t, from applying periodic boundary conditions (where n is an integer).

The concept of resonance errors in electron diffraction was introduced by Howie (1963), and has been applied to scattering by perfect crystals by Young and Rez (1975) and in detail by Rez *et al* (1977). For finite perfect crystals resonance errors are important because the same phonon, for example, can give rise to transitions to a given final-state Bloch wave from different initial-state Bloch waves. This leads

to partial coherence effects in the inelastically scattered electron (Rez *et al* 1977). For an imperfect crystal the resonance error in a sense couples to the defect strain field since both effects give rise to phase changes in the inelastically scattered electrons. Calculations of electron scattering by crystalline defects taking into account inelastic scattering and resonance errors have been made by Melander and Sandström (1975a, b) and Rez (1976). A qualitative discussion of resonance errors has been given by Humphreys (1977).

6. Diffraction from imperfect crystals

6.1. Introduction and general theory

In the last twenty years an enormous expansion in the theory and practice of electron diffraction and microscopy of imperfect crystals has occurred. This has largely been a result of the discovery that dislocations could be imaged in an electron microscope (Hirsch *et al* 1956, Bollmann 1956). In one section of a review article it is impossible to cover this topic adequately: we shall therefore be highly selective and present the general theory, give some applications, comment upon some approximations made in image interpretation and mention some recent developments. Early developments have been well covered in the book by Amelinckx (1964). More recent work is discussed by Hirsch *et al* (1977) and Humphreys (1979).

Let a perfect crystal be deformed. If the jth atom is moved from position $\boldsymbol{r}_j$ to $\boldsymbol{r}_j+\boldsymbol{R}(\boldsymbol{r}_j)$ the potential at any point $\boldsymbol{r}$ in the deformed crystal is clearly different from that at point $\boldsymbol{r}$ in the perfect crystal. In the deformable ion approximation, the potential at any point $\boldsymbol{r}$ in the deformed crystal is identified with the potential at the point $(\boldsymbol{r}-\boldsymbol{R}(\boldsymbol{r}))$ in the undeformed crystal. Hence the potential in the deformed crystal can be expanded as a Fourier series, as was done for the undeformed crystal (equation (4.2)), i.e.

$$V(\boldsymbol{r})=\sum_{\boldsymbol{g}} V_{\boldsymbol{g}} \exp\left(-2\pi i \boldsymbol{g}.\boldsymbol{R}\right) \exp\left(2\pi i \boldsymbol{g}.\boldsymbol{r}\right). \tag{6.1}$$

This deformable ion type of potential is the potential normally used in electron diffraction calculations for imperfect crystals. The potential is not valid if $\boldsymbol{R}(\boldsymbol{r})$ varies rapidly, e.g. close to a dislocation core. In addition the potential neglects changes in $V_{\boldsymbol{g}}$ due to changes in the volume of the 'unit cell' which again occurs near to a dislocation core, for example. The rigid ion model is probably a better approximation than the deformable ion model for rapid variations of the displacement $\boldsymbol{R}$ (see Rez 1978b). In the rigid ion approximation the imperfect crystal potential is the sum of atomic potentials:

$$V(\boldsymbol{r})=\sum_{j} V_{\text{atomic}}(\boldsymbol{r}-\boldsymbol{r}_j-\boldsymbol{R}_j(\boldsymbol{r}_j)). \tag{6.2}$$

The correct potential would take into account not only the atomic positions in the deformed crystal, which in general are not accurately known, but also the valence electron redistribution in the neighbourhood of the defect, which again is not known. There are therefore difficulties in the interpretation of defect images at very high resolution, i.e. at about 4 Å or better. However, away from the defect core region the deformable ion approximation, equation (6.1), should be valid, and we shall use this below.

Comparing equations (6.1) and (4.2) it is clear that the Fourier coefficient $V_{\boldsymbol{g}}$

in the undeformed crystal becomes $V_g \exp(-2\pi i \boldsymbol{g}.\boldsymbol{R})$ in the deformed crystal. Similarly the electron wavefunction at a point $\boldsymbol{r}$ in the deformed crystal may be written as (cf equations (5.3) and (5.4))

$$\Psi(\boldsymbol{r}) = \sum_j \alpha^{(j)}(\boldsymbol{r}) \sum_g C_g^{(j)} \exp[2\pi i(\boldsymbol{k}^{(j)} + \boldsymbol{g}).\boldsymbol{r}] \exp(-2\pi i \boldsymbol{g}.\boldsymbol{R}) \tag{6.3}$$

where $\alpha^{(j)}(\boldsymbol{r})$ is the amplitude of the jth Bloch wave at position $\boldsymbol{r}$. In a perfect crystal each Bloch wave amplitude $\alpha^{(j)}(\boldsymbol{r})$ only changes due to absorption (equation (5.4)). In an imperfect crystal, the effect of the displacement $\boldsymbol{R}(\boldsymbol{r})$ is to cause scattering between the Bloch waves, so that $\alpha^{(j)}(\boldsymbol{r})$ may increase or decrease due to scattering to and from other Bloch waves. It is this scattering which produces the defect contrast. Scattering between different Bloch wave states, i.e. from one branch of the dispersion surface to another, is called interbranch scattering. Scattering along the same branch of the dispersion surface is called intrabranch scattering.

In order to evaluate equation (6.3), the variation of $\alpha^{(j)}(\boldsymbol{r})$ with $\boldsymbol{r}$ due to the displacement $\boldsymbol{R}(\boldsymbol{r})$ must be calculated. This is a problem of some complexity and most calculations in electron diffraction and microscopy make a simplifying approximation known as the column approximation (Hirsch *et al* 1960, Howie and Whelan 1961). In this approximation the imperfect crystal is divided into narrow columns with the length of each column being parallel to the reflecting planes operating. The displacement in a given column is assumed to vary only along the length of the column, defined as the z direction, so that the displacement is $\boldsymbol{R}(z)$. The basic assumption of the column approximation is that each column may be chosen sufficiently narrow that the displacement within it is essentially only a function of z, yet sufficiently wide that an electron entering the top of the column is not scattered out of the column in its passage through the crystal. Use of the column approximation greatly facilitates calculations for imperfect crystals since it essentially enables the problem of solving a coupled set of three-dimensional second-order partial differential equations to be reduced to that of solving a complete set of one-dimensional (in z only) first-order ordinary differential equations, i.e. equation (6.4) below. This important approximation is discussed further in §6.4.

Using the column approximation, the problem of calculating the variation of $\alpha^{(j)}(\boldsymbol{r})$ with $\boldsymbol{r}$ due to a displacement $\boldsymbol{R}(\boldsymbol{r})$ reduces to evaluating in a given column the variation of $\alpha^{(j)}(z)$ with depth z due to $\boldsymbol{R}(z)$. Substituting equations (6.1) and (6.3) into the Schrödinger equation (equation (4.11)), and using the column approximation, gives the variation of $\alpha^{(j)}(z)$ with z as

$$\frac{\mathrm{d}\alpha^{(j)}(z)}{\mathrm{d}z} = 2\pi i \sum_i \alpha^{(i)}(z) \exp[2\pi i(k_z^{(i)} - k_z^{(j)})z] \sum C_g^{*(j)} C_g^{(i)} \frac{\mathrm{d}}{\mathrm{d}z}(\boldsymbol{g}.\boldsymbol{R}(z)) - 2\pi q^{(j)} \alpha^{(j)}(z). \tag{6.4}$$

Equation (6.4) represents the change in amplitude of the jth Bloch wave in a slice of crystal of thickness $\mathrm{d}z$ at a depth z. The last term gives the amplitude lost due to absorption within the slice. The first terms give the amplitude gained (or lost if negative) due to interbranch scattering (the terms for which $i \neq j$) and intrabranch scattering ($i = j$).

Equation (6.4) may be integrated numerically for a given $\boldsymbol{R}(z)$ using standard computer routines to yield $\alpha^{(j)}(t)$, the Bloch wave amplitudes at the bottom surface

of the crystal of thickness t. The intensity of the gth diffracted beam is then given by, from equation (4.32),

$$I_g(t) = \left| \sum_j \alpha^{(j)}(t) C_g^{(j)} \exp\left(2\pi i k_z^{(j)} t\right) \right|^2. \tag{6.5}$$

Thus we may calculate the diffracted intensities from a crystal containing any defect of given displacement $\boldsymbol{R}$.

A very important question is that of uniqueness. Do different defects, with different displacement functions $\boldsymbol{R}$, give rise to different and unique diffracted intensities? Head (1969) has shown that the component of the displacement field in the direction of the diffracting vector is uniquely specified by the corresponding electron micrograph. The proof is for two-beam or many-beam systematic diffraction conditions; it assumes that there is a direction in the crystal along which the displacements are constant and the column approximation is assumed also. Hence, given these assumptions, a set of three micrographs taken with non-coplanar diffracting vectors uniquely identify a defect and specify its displacement field. For an arbitrary 'cross-grating' orientation, Head (1969) showed that three independent micrographs also uniquely identify the defect displacement field, although there is no longer a direct connection between one micrograph and one component of the displacement field.

Hence the electron microscope is an extremely powerful tool for determining defect strain fields. As an illustration we consider below the particular case of dislocations.

6.2. Imaging of dislocations

Initially some general principles will be illustrated for a simple screw dislocation followed by a more general discussion. For a detailed discussion of the images of dislocations with complicated displacement fields see the book by Head *et al* (1973).

The simplest case to consider is a screw dislocation parallel to the plane of the specimen and at depth y. We also assume isotropic elasticity theory in an infinite medium. The displacement at a depth z in a column of perpendicular distance x from the dislocation is then given by

$$\boldsymbol{R} = \frac{\boldsymbol{b}}{2\pi} \tan^{-1}\left(\frac{z-y}{x}\right) \tag{6.6}$$

From equation (6.4) there is no interbranch or intrabranch scattering (and hence the defect is invisible) if, for all reflections $\boldsymbol{g}$ operating,

$$\frac{\mathrm{d}}{\mathrm{d}z}(\boldsymbol{g}.\boldsymbol{R}) = 0. \tag{6.7}$$

For equation (6.7) to hold everywhere in the crystal this implies that for a dislocation there is no image contrast if

$$\boldsymbol{g}.\boldsymbol{R} = 0 \tag{6.8}$$

for all $\boldsymbol{g}$. Normally in 100 kV microscopy the crystal is oriented so that only one diffracted beam is strong, which clearly facilitates Burgers vector analysis. (The term 'defect invisibility' means that the scattering from the region of crystal con-

taining the dislocation is identical to and indistinguishable from the scattering from the rest of the (perfect) crystal.)

The following results are obtained using equations (6.6) and (6.4):

(i) If $\boldsymbol{g}.\boldsymbol{b}=0$ the dislocation image is invisible. Thus the Burgers vector can be determined.

(ii) If $\boldsymbol{g}.\boldsymbol{b}=1$, and if the dislocation lies near the middle of a reasonably thick foil oriented near the Bragg position, the image consists of a single dark peak of similar shape in both bright-field and dark-field. Figure 23 shows a computed image profile using two-beam theory. The dark peak is a result of anomalous absorption (see §5.3) and may be simply explained using two-beam theory as follows. At the top surface of the crystal Bloch waves 1 and 2 have approximately equal amplitudes $\alpha^{(1)}$ and $\alpha^{(2)}$ (if the crystal is near the Bragg position). Wave 1 is strongly absorbed, and if the crystal is reasonably thick mainly electrons represented by wave 2 reach

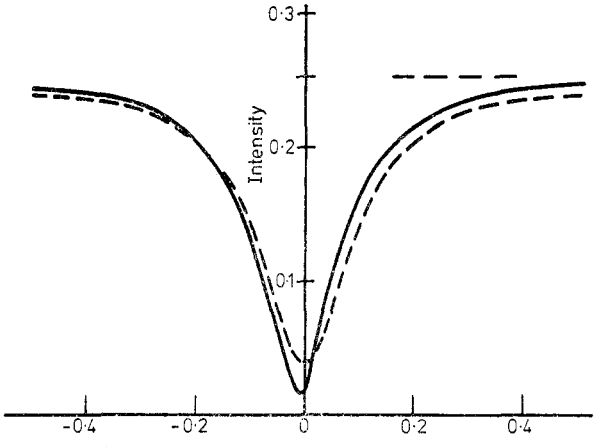

Figure 23. Computed bright-field (full curve) and dark-field (broken curve) images for a screw dislocation in the middle of a thick foil with $t=8\xi_g$ and $\boldsymbol{g}.\boldsymbol{b}=1$, two-beam theory, 100 keV incident electrons. The crystal is at an exact Bragg position and the intensity is plotted as a function of x/ξ_g, where x is the distance from the dislocation core. The horizontal broken line indicates the perfect crystal background intensity (from Howie and Whelan (1961), by courtesy of The Royal Society).

the dislocation. Since the amount of interbranch scattering from wave i is proportional to $\alpha^{(i)}$, the interbranch scattering by the dislocation is mainly from wave 2 to wave 1, which is then strongly absorbed as it propagates to the lower surface of the crystal. Hence a dislocation (or any defect which produces interbranch scattering) near the middle of a thick foil produces a decrease in the transmitted electron intensity.

(iii) If the crystal is very thin, so that absorption is negligible, bright-field and dark-field images are complementary owing to electron conservation. Most specimens, however, are sufficiently thick for absorption to be important, as in case (ii) above.

(iv) If the dislocation is inclined, running from the top to the bottom of the specimen (i.e. varying y in equation (6.6)), the image profile varies as y varies and typically near the top and bottom of the specimen the image appears like a zigzag line, with black and white oscillations in contrast. This effect is not due to the

changes in strain field near the surface (which should be taken into account in calculations) but is a dynamical diffraction effect due to the fact that the dislocation is situated in the beat pattern of the Bloch wave fields. From equation (6.4) the amount of interbranch scattering is a function of $\exp[2\pi i(k_z^{(i)}-k_z^{(j)})z]$. Now $(k_z^{(i)}-k_z^{(j)})^{-1}$ is equal to the extinction distance ξ_g for branches i and j. It follows that the depth periodicity of the oscillations is the extinction distance, and thus this effect can be used to simply measure the distance of the dislocation from the surface.

(v) The image peak has a width of about $0{\cdot}2\xi_g$. Since extinction distances for low-order reflections are typically in the range 200–1000 Å for many materials, the width of the image is typically in the range 40–200 Å. Hence the effective resolution when imaging dislocations in the conventional manner described so far (i.e. a bright-field or a dark-field image with the crystal oriented near a low-order Bragg position) is rather poor. The weak-beam imaging technique, which results in narrower images, will be described in §6.3.

(vi) For $\boldsymbol{g}.\boldsymbol{b}=2$, the image of a screw dislocation near the middle of a reasonably thick foil consists of two dark peaks. For an inclined dislocation near the foil surfaces oscillating contrast is again produced.

(vii) The bright-field image of an inclined screw dislocation is symmetrical about the centre of the dislocation, while the dark-field image is asymmetrical, being similar to the bright-field image near the top surface of the foil and pseudo-complementary to it near the bottom surface. Hence the sense of the inclination of the dislocation may be determined.

For an edge dislocation to be invisible, it follows from the edge dislocation displacement $\boldsymbol{R}$, in an infinite isotropic medium, that both $\boldsymbol{g}.\boldsymbol{b}$ and $\boldsymbol{g}.\boldsymbol{b}\wedge\boldsymbol{u}$ must be zero, where $\boldsymbol{u}$ is a unit vector along the dislocation line. These conditions are fulfilled by choosing a diffracting vector which is along the line of the dislocation. As with the case of a screw dislocation, invisibility physically occurs because the diffracting planes are undistorted by the dislocation.

Edge dislocation profiles are qualitatively similar to the screw dislocation profiles described above (exhibiting oscillatory contrast near the surface, etc) for the same physical reasons. Due to the different strain fields the image of a pure edge dislocation is, however, wider than that of a screw, typically by a factor of about two.

A mixed dislocation produces displacements in all directions, hence it is impossible to find a diffracting vector to render the dislocation invisible. The Burgers vector can only be found by detailed comparison of calculated profiles with experimental images. Also the simple invisibility criteria stated above for pure edge and screw dislocations were derived using isotropic elasticity: they do not apply to materials in which elastic anisotropy is important. Again, for such materials a detailed comparison of calculated and experimental micrographs must be made. The anisotropic elasticity description of $\boldsymbol{R}$ must normally be computed numerically for use in the diffraction calculation.

The conventional method of displaying the calculated intensity of electrons scattered from a crystal containing a defect is to draw an intensity profile (see, for example, figure 23), i.e. a plot of the variation of the intensity along a line traversing the defect. However, as mentioned above, defect identification often requires the detailed comparison of an experimental micrograph with theory. To facilitate this the concept of 'computed micrographs' was proposed (Head 1967, Humble 1970, Head *et al* 1973), in which computed intensities are presented directly in micrograph

form for easy comparison with experiment. The method proposed by Head (1967) to present the calculated intensity values in the form of half-tone 'micrographs' utilises a standard computer line printer, and this display method is the one most widely used at the present time. The normal dots in a halftone reproduction are replaced by line printer characters: a grey scale is produced by using punctuation marks (e.g. full stop, colon, etc) at the light end of the scale and by overprinting characters at the dark end. The number of shades of grey normally employed using this method is about ten. Better quality computed micrographs can be produced using cathode ray tube displays (Maher *et al* 1971) or sophisticated optical instruments. Figure 24 (plate) shows such computed micrographs, which are almost indistinguishable in quality from experimental micrographs.

6.3. The weak-beam method

The main disadvantage of the conventional dislocation imaging methods discussed above is that, although the instrumental resolution of a modern 100 kV electron microscope is typically about 3 Å (point-to-point), dislocation image widths are of the order of 100 Å. Thus not only is the resolution capability of the microscope not utilised but also, and more importantly, the dislocation images are sufficiently broad that fine structure in the object (e.g. a pair of partial dislocations separated by 50 Å) cannot be resolved. The main advantage of the weak-beam method (Cockayne *et al* 1969) is that the dislocation image width is very much narrower (typically about 15 Å) than conventional strong-beam images and hence higher resolution work is possible. Figure 25 (plate) shows a comparison of a conventional strong-beam image and weak-beam image. The narrower dislocation images and hence higher resolution is clearly evident in the weak-beam image.

A simple qualitative explanation of the weak-beam technique is as follows. If a perfect crystal is oriented at an exact Bragg position, the corresponding diffracted beam is strong (unless the crystal thickness happens to be an integral multiple of the extinction distance). As the crystal is tilted away from the Bragg position, the intensity in the diffracted beam decreases, so that the diffracted beam becomes a 'weak beam'. If the crystal contains a dislocation, the lattice planes around the dislocation are locally tilted and hence some of these planes may locally be tilted back into the Bragg position. If this is the case, the scattered intensity from perfect crystal regions will be weak, but the intensity scattered locally from the region of crystal that satisfies the Bragg condition will be strong. As the deviation of the perfect crystal from the Bragg position increases, the dislocation image comes from crystal regions that are increasingly distorted, i.e. increasingly close to the dislocation core.

Most applications of the weak-beam technique have been concerned with the measurement of stacking fault energies, obtained from the separation of two partial dislocation image peaks (Cockayne *et al* 1969, 1971a, b, Stobbs and Sworn 1971, Jenkins 1972). However, the method is increasingly being used to reveal dislocation structures at high resolution (Ray and Cockayne 1971, Bicknell 1971, Nordlander and Thölén 1973, Jenkins *et al* 1973, Carter and Hirsch 1977, Carter and Holmes 1977).

6.4. The column approximation and elastic diffuse imaging

As noted in §6.2, most calculations in electron diffraction and microscopy make

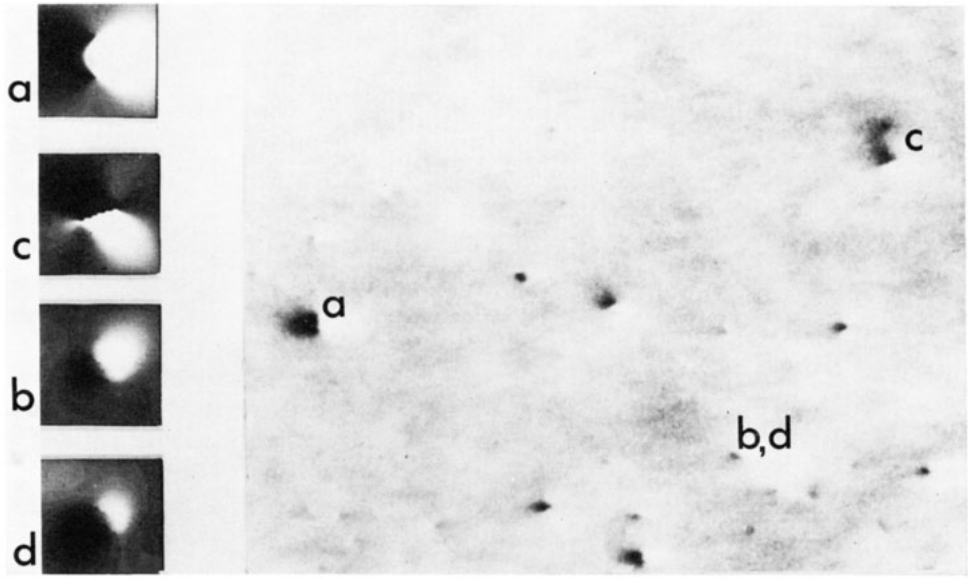

Figure 24. Computed micrographs (on left) and experimental micrograph (on right). The computed micrographs were produced using an optical instrument which can reproduce 64 shades of grey from digitised intensities. The specimen was copper irradiated with 30 keV Cu^+ ions and the defects produced are dislocation loops of various types which can be identified by comparing the experimental and computed micrographs (for further details see Saldin *et al* (1979), by courtesy of The Royal Society).

the column approximation. Although this approximation is normally valid for medium or low resolution electron microscopy (Howie and Basinski 1968, Jouffrey and Taupin 1967), for high-resolution microscopy (resolution better than about 10 Å), the column approximation can break down significantly (Humphreys and Drummond 1976b).

The breakdown of the column approximation is particularly noticeable if the crystal is not oriented at an exact Bragg position. The electron flux is then not parallel to the columns of the column approximation and hence an incident electron is not contained within this column on propagating through the crystal. There is therefore a net 'sideways' scattering which the column approximation cannot take into account. Figure 26 shows weak-beam images of a dislocation calculated with

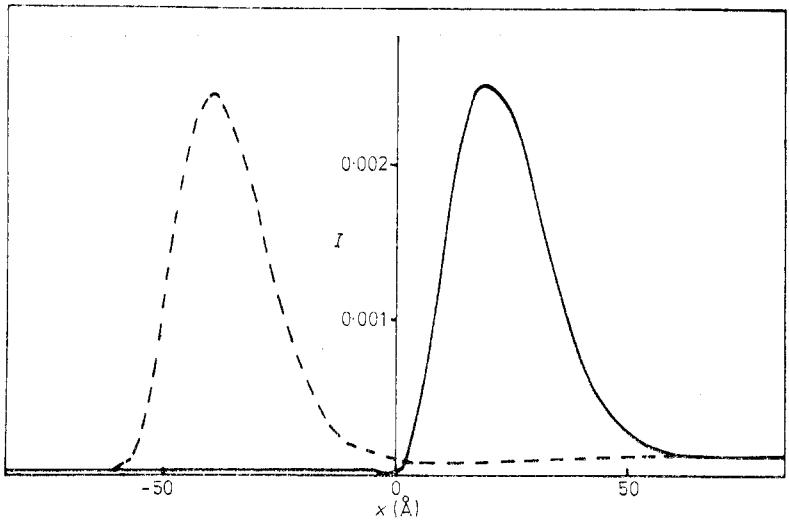

Figure 26. Calculated weak-beam images of an edge dislocation in Cu with (———) and without (– – – –) the column approximation. Dislocation at depth ξ_g (=4·78 Å) in a foil thickness $4\xi_g$, $\boldsymbol{g}=2\bar{2}0$, $s=-2\cdot5\times10^{-2}$ Å^{-1}, $\boldsymbol{u}=[11\bar{2}]$, $\boldsymbol{b}=[1\bar{1}0]$, 100 keV electrons (from Humphreys and Drummond (1977), by courtesy of The Institute of Physics).

and without assuming the column approximation. The shapes of the images are very similar but there is a marked shift in the image peak positions. The column approximation calculation puts the image peak on the wrong side of the projected dislocation core position in this case. Although in this case the shapes of the images are similar at very high resolutions (better than about 4 Å) the column approximation may break down completely (Humphreys and Drummond 1976b) since it does not correctly take into account elastic diffuse scattering.

Whereas a perfect crystal scatters into discrete Bragg directions, an imperfect crystal scatters in all directions. This scattering by the imperfection(s) into directions other than Bragg directions is known as elastic diffuse scattering. If very high resolution electron micrographs of defects are to be correctly interpreted it is necessary to take the elastic diffuse scattering properly into account. In addition, in order to achieve higher resolution than is possible using the weak-beam technique, it may be necessary to use explicitly the elastic diffuse scattering for imaging (Fields and

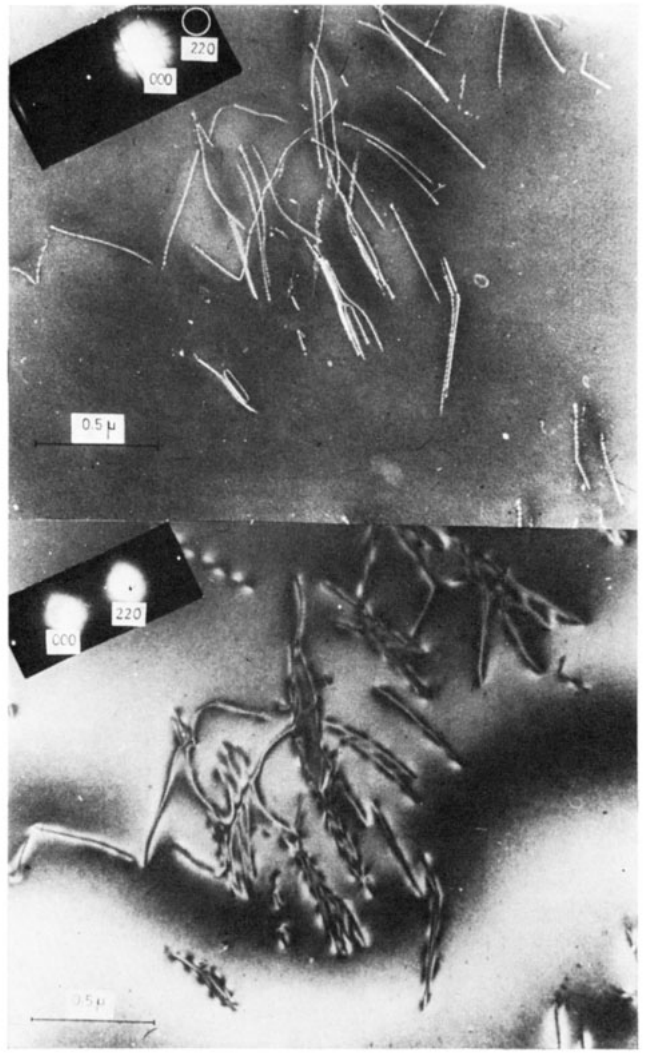

Figure 25. A weak-beam (top) and a strong-beam (bottom) image of the same region of a silicon specimen containing inclined dislocations. The strong-beam dark-field image (bottom) was formed using a strong 220 reflection. The weak-beam image used the same 220 reflection, but under weak-beam conditions. The dislocation geometry and dissociation is clearly observed in the weak-beam image (from Ray and Cockayne (1971), by courtesy of The Royal Society).

Cowley 1977, Humphreys and Drummond 1977, Humphreys *et al* 1977, Krakow *et al* 1977, Spence 1977).

For an isolated defect the elastic diffuse scattering is peaked around the Bragg directions, the scattering from regions of small distortion being close to the Bragg directions and the scattering from the highly disordered region around the dislocation core being further away. Figure 27 shows the intensity distribution in the diffraction pattern due to a single dislocation, calculated dynamically and without using the column approximation. The elastic diffuse scattering between the Bragg spots is clear and this diffuse intensity is evidently very sharply peaked about the Bragg positions (the intensity axis in figure 27 is logarithmic).

In order to calculate the diffuse scattering in the diffraction plane, the wavefunction of the fast electron at the bottom surface of the crystal is calculated, not using the

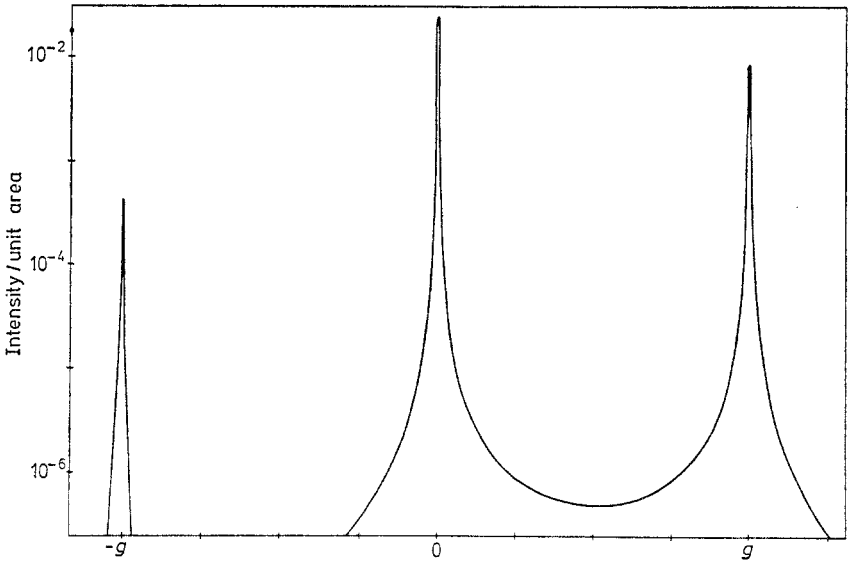

Figure 27. The intensity distribution in the diffraction pattern due to the elastic diffuse scattering from a Cu crystal containing an edge dislocation. All parameters as in figure 26 caption except that dislocation at depth ξ_g in a foil thickness $2\xi_g$ (from Humphreys and Drummond (1977), by courtesy of The Institute of Physics).

column approximation. The Fourier transform of this wavefunction gives the amplitude in the diffraction plane. (The intensity distribution of figure 27 is the squared modulus of this amplitude.) The image can be calculated by considering an aperture placed at any chosen position in the diffraction pattern and calculating the Fourier transform of the amplitude within this aperture. Corrections can also be made for defocus and aberrations using the appropriate transfer function. Figure 28 shows dark-field images of an edge dislocation for a crystal set at the exact Bragg position. Figure 28(*c*) has the same aperture as figure 28(*b*) except that there is a very small stop in the centre of the aperture (i.e. an annular aperture). The complete change of the image demonstrates the importance of elastic diffuse scattering.

At present it is not clear what are the optimum experimental conditions necessary in order to obtain information on the arrangement of atoms in dislocation cores and around point defects. It is, however, clear that such information must be contained

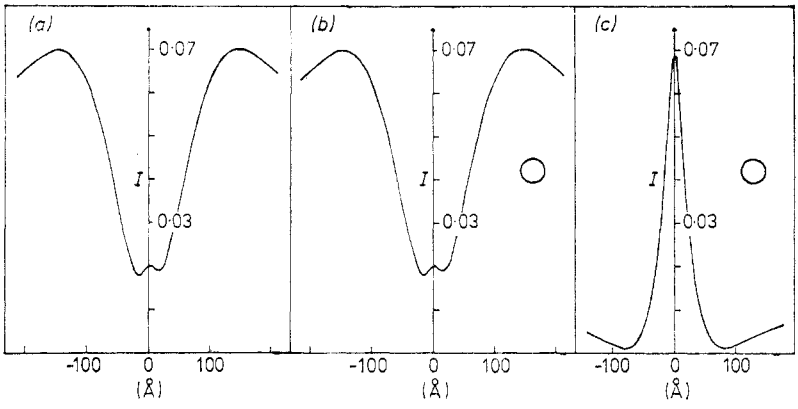

Figure 28. Dark-field images for an edge dislocation in Cu. Crystal at exact Bragg $2\bar{2}0$ position: (*a*) usual calculation, (*b*) image calculated for objective aperture diameter $\frac{1}{4}g$ centred on diffraction spot, (*c*) image calculated for annular aperture centred on diffraction spot: aperture diameter $\frac{1}{4}g$, central stop diameter $g/359$ (from Humphreys and Drummond (1977), by courtesy of The Institute of Physics).

in the elastic diffuse scattering from such defects. It is expected that within the next 10 years it should prove possible to determine from high-resolution electron micrographs the atomic configuration in dislocation cores and around point defects and other imperfections. Thus the scattering of fast electrons by crystals can be used not only to measure precisely perfect crystal parameters such as the bonding charge density (§§5.7 and 5.9) and the crystal symmetry (§§5.7 and 5.8) but also to characterise the atomic structure of crystal imperfections.

Acknowledgments

The author is grateful to many colleagues for useful discussions, Dr R A A Drummond for assistance with computing and diagrams and for reading the text, and Mr D Smart for his comments on the text.

References

Amelinckx S 1964 *The Direct Observation of Dislocations* (New York: Academic)
Berry M V 1971 *J. Phys. C: Solid St. Phys.* **4** 697
Bethe H A 1928 *Ann. Phys., Lpz.* **87** 55
Bicknell R W 1971 *Phys. Stat. Solidi* a **7** K1
Boersch H, Jeschke G and Raith H 1964 *Z. Phys.* **181** 436
Bollmann W 1956 *Phys. Rev.* **103** 1588
Booker G R and Humphreys C J 1975 *Electron Microscopy in Materials Science* ed U Valdrè and R Ruedl (Luxembourg: Commission of the European Communities) Part IV, p1199
Booker G R, Joy D C, Spencer J P and Humphreys C J 1973 *Scanning Electron Microscopy/1973* ed O Johari (Chicago: IIT Research Institute) p251
Booker G R, Shaw A M B, Whelan M J and Hirsch P B 1967 *Phil. Mag.* **16** 1185
Born M 1926 *Z. Phys.* **37** 863, **38** 803
Bragg W L 1913 *Proc. Camb. Phil. Soc.* **17** 43
Butler E P 1972 *Phil. Mag.* **26** 33
Buxton B F, Eades J A, Steeds J W and Rackham G M 1976 *Phil. Trans. R. Soc.* **281** 171
Buxton B F and Loveluck J E 1977 *J. Phys. C: Solid St. Phys.* **10** 3941

Carter C B and Hirsch P B 1977 *Phil. Mag.* **35** 1509
Carter C B and Holmes S H 1977 *Phil. Mag.* **35** 1161
Cherns D 1974 *Phil. Mag.* **30** 549
—— 1979 *Surf. Sci.* **90** in press
Clarke D R and Howie A 1971 *Phil. Mag.* **24** 959
Coates D G 1967 *Phil. Mag.* **16** 1179
Cockayne D J H, Goodman P, Mills J C and Moodie A F 1967 *Rev. Sci. Instrum.* **38** 1093
Cockayne D J H, Jenkins M L and Ray I L F 1971a *Phil. Mag.* **24** 1383
Cockayne D J H, Parsons J R and Hoelke C W 1971b *Phil. Mag.* **24** 139
Cockayne D J H, Ray I L F and Whelan M J 1969 *Phil. Mag.* **20** 1265
Cowley J M 1969 *Appl. Phys. Lett.* **15** 58
—— 1975 *Diffraction Physics* (Amsterdam: North-Holland)
Cowley J M and Moodie A F 1957 *Proc. Phys. Soc.* B **70** 486
—— 1970 *Acta Crystallogr.* A **26** 152
Crewe A V and Wall J 1970 *Optik* **30** 461
Crewe A V, Wall J and Langmore J P 1970 *Science* **168** 1138
Cundy S L, Howie A and Valdrè U 1969 *Phil. Mag.* **20** 147
Darwin C G 1914 *Phil. Mag.* **27** 315, 675
Davisson C J and Germer L H 1927 *Nature* **119** 558
de Broglie L 1924 *Phil. Mag.* **47** 446
Dederichs P H 1972 *Solid St. Phys.* **27** 135
Doyle P A and Turner P S 1968 *Acta Crystallogr.* A **24** 390
Duncumb P 1962 *Phil. Mag.* **7** 2101
Ewald P P 1913 *Phys. Z.* **14** 465
Fields P M and Cowley J M 1977 *Proc. 35th Annual Meeting of the Electron Microscopy Society of America* ed G W Bailey (Baton Rouge: Claitors) p14
Formanek H, Muller M, Hahn M H and Koller T H 1971 *Naturw.* **58** 339
Freeman A J 1959 *Acta Crystallogr.* **12** 274, 929
—— 1960 *Acta Crystallogr.* **13** 190, 618
Friedrich W, Knipping P and Laue M von 1912 *Proc. Bavarian Acad. Sci.* p303
Fujimoto F 1959 *J. Phys. Soc. Japan* **14** 1558
Fujita H, Tabata T, Sumida N and Yoshida K 1974 *High Voltage Electron Microscopy* ed P R Swann, C J Humphreys and M J Goringe (New York: Academic) p426
Fujiwara K 1962 *J. Phys. Soc. Japan* **17** *Suppl.* BII 118
Fukuhara A 1965 *Proc. Phys. Soc.* **86** 1031
Gjønnes J K 1964 *Acta Crystallogr.* **17** 1075
—— 1966 *Acta Crystallogr.* **20** 240
Gjønnes J K and Moodie A F 1965 *Acta Crystallogr.* **19** 65
Glauber R and Schomaker V 1953 *Phys. Rev.* **89** 667
Goodman P 1976 *Acta Crystallogr.* A **32** 793
Goodman P and Lehmpfuhl G 1964 *Z. Naturf.* **19a** 818
—— 1967 *Acta Crystallogr.* **22** 14
—— 1968 *Acta Crystallogr.* A **24** 400
Goodman P and Moodie A F 1974 *Acta Crystallogr.* A **30** 280
Hall C R 1966 *Proc. R. Soc.* A **295** 140
Hashimoto H, Howie A and Whelan M J 1962 *Proc. R. Soc.* A **269** 80
Hashimoto H, Kumao A, Hino K, Yotsumoto H and Ono A 1971 *Jap. J. Appl. Phys.* **10** 1115
Head A K 1967 *Aust. J. Phys.* **20** 557
—— 1969 *Aust. J. Phys.* **22** 43, 345
Head A K, Humble P, Clarebrough L M, Morton A J and Forwood C T 1973 *Computed Electron Micrographs and Defect Identification* (Amsterdam: North-Holland)
Heinrich K F J, Newbury D E and Yakowitz H (ed) 1976 *Use of Monte Carlo Calculations in Electron Probe Microanalysis and Scanning Electron Microscopy. NBS Special Publ.* 460 (Washington: US Government Printing Office)
Heisenberg W 1925 *Z. Phys.* **33** 879
Henkelman R M and Ottensmeyer F P 1971 *Proc. Nat. Acad. Sci.* **68** 3000
Hewat E A and Humphreys C J 1974 *High Voltage Electron Microscopy* ed P R Swann, C J Humphreys and M J Goringe (New York: Academic) p52

Hirsch P B, Horne R W and Whelan M J 1956 *Phil. Mag.* **1** 677
Hirsch P B, Howie A, Nicholson R B, Pashley D W and Whelan M J 1977 *Electron Microscopy of Thin Crystals* (New York: Krieger)
Hirsch P B, Howie A and Whelan M J 1960 *Phil. Trans. R. Soc.* A **252** 499
—— 1962 *Phil. Mag.* **7** 2095
Hirsch P B and Humphreys C J 1970 *Proc. 3rd Annual Scanning Electron Microscope Symp.* ed O Johari (Chicago: IIT Research Institute) p449
Hoerni J A 1950 *Helv. Phys. Acta* **23** 587
—— 1956 *Phys. Rev.* **102** 1534
Hoerni J A and Ibers J A 1953 *Phys. Rev.* **91** 1182
Howie A 1963 *Proc. R. Soc.* A **271** 268
—— 1972 *Proc. 5th Europ. Congr. on Electron Microscopy, Manchester* (Bristol: The Institute of Physics) p408
Howie A and Basinski Z S 1968 *Phil. Mag.* **17** 1039
Howie A and Stern R M 1972 *Z. Naturf.* **27a** 382
Howie A and Whelan M J 1961 *Proc. R. Soc.* A **263** 217
Humble P 1970 *Modern Diffraction and Imaging Techniques in Materials Science* ed S Amelinckx, R Gevers, G Remaut and J Van Landuyt (Amsterdam: North-Holland) p99
Humphreys C J 1972 *Phil. Mag.* **25** 1459
—— 1977 *Proc. 35th Annual Meeting of the Electron Microscopy Society of America* ed G W Bailey (Baton Rouge: Claitors) p78
—— 1979 *Dislocations in Solids* ed F R N Nabarro (Amsterdam: North-Holland) in press
Humphreys C J and Drummond R A 1976a *Proc. 6th Europ. Congr. on Electron Microscopy, Jerusalem* vol 1 (Jerusalem: Tal International) p176
—— 1976b *Proc. 6th Europ. Congr. on Electron Microscopy, Jerusalem* vol 1 (Jerusalem: Tal International) p142
—— 1977 *Electron Microscopy and Analysis 1977* ed D L Misell (Bristol: The Institute of Physics) p241
Humphreys C J, Drummond R A, Hart-Davis A and Butler E P 1977 *Phil. Mag.* **35** 1543
Humphreys C J and Fisher R M 1971 *Acta Crystallogr.* A **27** 42
Humphreys C J, Hart-Davis A and Spencer J P 1974 *Proc. 8th Int. Congr. on Electron Microscopy, Canberra* vol 1 (Canberra: Australian Academy of Science) p248
Humphreys C J and Hirsch P B 1968 *Phil. Mag.* **18** 115
Humphreys C J, Thomas L E, Lally J S and Fisher R M 1971 *Phil. Mag.* **23** 87
Humphreys C J and Whelan M J 1969 *Phil. Mag.* **20** 165
Hurley A C, Johnson A W S, Moodie A F, Rez P and Sellar J R 1978 *Electron Diffraction 1927–1977* ed P J Dobson, J B Pendry and C J Humphreys (Bristol: The Institute of Physics) p34
Ibers J A and Hoerni J A 1954 *Acta Crystallogr.* **7** 405
Ichikawa M and Ohtsuki Y H 1968 *J. Phys. Soc. Japan* **27** 953
Iijima S and Allpress J G 1974 *Acta Crystallogr.* A **30** 22
International Tables for X-Ray Crystallography 1962 (Birimingham: Kynoch)
Isaacson M, Kopf D and Utlaut M 1977 *Proc. 35th Annual Meeting of the Electron Microscopy Society of America* ed G W Bailey (Baton Rouge: Claitors) p78
James R W 1967 *The Optical Principles of the Diffraction of X-rays* (London: Bell and Sons)
Jenkins M L 1972 *Phil. Mag.* **26** 747
Jenkins M L, Cockayne D J H and Whelan M J 1973 *J. Microsc.* **98** 155
Jones P M, Rackham G M and Steeds J W 1977 *Proc. R. Soc.* A **354** 197
Jouffrey B and Taupin D 1967 *Phil. Mag.* **16** 703
Kainuma Y 1955 *Acta Crystallogr.* **8** 247
Kambe K and Molière K 1970 *Advances in Structure Research by Diffraction Methods* vol 3 ed R Brill and R Mason (Oxford: Pergamon) p53
Kossel W and Mollenstedt G 1939 *Ann. Phys., Lpz.* **36** 113
Krakow W, Chang A L J and Sass S L 1977 *Phil. Mag.* **35** 575
Lally J S, Humphreys C J, Metherell A J F and Fisher R M 1972 *Phil. Mag.* **25** 321
Langmore J P, Wall J and Isaacson M S 1973 *Optik* **38** 335
von Laue M 1935 *Ann. Phys., Lpz.* **23** 705
Lenz F 1954 *Z. Naturf.* **9a** 185

MacGillavry C H 1940 *Physica* **7** 329
Maher D M, Perrin R C and Bullough R 1971 *Phys. Stat. Solidi* b **43** 707
Melander A and Sandström R 1975a *Acta Crystallogr.* A **31** 166
—— 1975b *J. Phys. C: Solid St. Phys.* **8** 767
Metherell A J F 1975 *Electron Microscopy in Materials Science* ed U Valdrè and E Ruedl (Luxembourg: Commission of the European Communities) Part II, p397
Metherell A J F and Fisher R M 1969 *Phys. Stat. Solidi* **32** 551
Moodie A F, Humphreys C J, Imeson D and Sellar J R 1978 *Electron Diffraction 1927–1977* ed P J Dobson, J B Pendry and C J Humphreys (Bristol: The Institute of Physics) p129
Moodie A F and Warble C E 1967 *Phil. Mag.* **16** 891
Morris R H, Bottoms W R and Peacock R G 1968 *J. Appl. Phys.* **39** 3016
Morse P M 1932 *Phys. Z.* **33** 443
Mott N F 1930 *Proc. R. Soc.* A **127** 658
Mott N F and Massey H S W 1965 *The Theory of Atomic Collisions* (Oxford: Oxford University Press)
Nagata F and Fukuhara A 1967 *Jap. J. Appl. Phys.* **6** 1233
Natta M 1968 *J. Physique* **29** 337
Niehrs H 1959a *Z. Naturf.* **14a** 504
—— 1959b *Z. Phys.* **156** 466
Nordlander I and Thölén A R 1973 *J. Microsc.* **98** 221
Pendry J B 1974 *Low Energy Electron Diffraction* (London: Academic)
Pogany A 1971 *Electron Microscopy and Analysis* (Bristol: The Institute of Physics) p64
Pogany A P and Turner P S 1968 *Acta Crystallogr.* A **24** 103
Radi G 1970 *Acta Crystallogr.* A **26** 41
Ray I L F and Cockayne D J H 1971 *Proc. R. Soc.* A **325** 543
Reimer L, Badde H G, Seidel H and Bühring W 1971 *Z. Angew. Phys.* **31** 145
Rez P 1976 *DPhil Thesis* University of Oxford
—— 1978a *Acta Crystallogr.* A **34** 48
—— 1978b *Electron Diffraction 1927–1977* ed P J Dobson, J B Pendry and C J Humphreys (Bristol: The Institute of Physics) p109
Rez P, Humphreys C J and Whelan M J 1977 *Phil. Mag.* **35** 81
Rocher A, Ayroles R, Mazel A, Mory C and Jouffrey B 1974 *High Voltage Electron Microscopy* ed P R Swann, C J Humphreys and M J Goringe (New York: Academic) p436
Saldin A K, Stathopoulos A Y and Whelan M J 1979 *Phil. Trans. R. Soc.* A **292** 523
Sandström R, Spencer J P and Humphreys C J 1974 *J. Phys. D: Appl. Phys.* **7** 1030
Schomaker V and Glauber R 1952 *Nature* **170** 290
Schrödinger E 1926 *Ann. Phys., Lpz.* **79** 361
Smart D J and Humphreys C J 1978 *Electron Diffraction 1929–1977* ed P J Dobson, J B Pendry and C J Humphreys (Bristol: The Institute of Physics) p145
Spence J C H 1977 *Proc. 35th Annual Meeting of the Electron Microscopy Society of America* ed G W Bailey (Baton Rouge: Claitors) p178
Spencer J P and Humphreys C J 1973 *Scanning Electron Microscopy: Systems and Applications* (Bristol: The Institute of Physics) p126
Spencer J P, Humphreys C J and Hirsch P B 1972 *Phil. Mag.* **26** 193
Sprague J A and Wilkens M 1970 *Proc. Septième Congrès de Microscopie Electronique, Grenoble* vol 1 (Paris: Société Française de Microscopie Electronique) p95
Steeds J W, Jones P M, Rackham G M and Shannon M D 1976 *Developments in Electron Microscopy and Analysis 1975* ed J A Venables (New York: Academic) p351
Stern R M, Perry J J and Boudreaux D S 1969 *Rev. Mod. Phys.* **41** 275
Stobbs W M and Sworn C H 1971 *Phil. Mag.* **24** 1365
Sturkey L 1957 *Acta Crystallogr.* **10** 856
—— 1962 *Proc. Phys. Soc.* **80** 321
Takagi S 1958 *J. Phys. Soc. Japan* **13** 278, 287
—— 1962 *Acta Crystallogr.* **15** 1311
Terakura K, Ohtsuki Y H and Yanagawa W 1966 *J. Phys. Soc. Japan* **21** 1973
Thomson G P and Reid A 1927 *Nature* **119** 890
Uyeda R 1968 *Acta Crystallogr.* A **24** 175
Venables J and Harland C 1973 *Phil. Mag.* **27** 1193

Vicario E, Pitaval M and Fontaine G 1970 *Proc. 7th Int. Congr. on Electron Microscopy, Grenoble* vol 2 (Paris: Société Française de Microscopie Electronique) p211
Watenabe D and Terasaki O 1972 *Proc. NBS 5th Materials Research Symp. NBS Special Publ.* 364 (Washington: US Government Printing Office) p155
Watenabe D, Uyeda R and Kogiso M 1968 *Acta Crystallogr.* A **24** 249
Wentzel G 1927 *Z. Phys.* **40** 590
Whelan M J 1962 *J. Phys Soc. Japan.* **17** *Suppl.* BII 122
—— 1965 *J. Appl. Phys.* **36** 2099
—— 1975 *Adv. Electron. Electron Phys.* **39** 1
Wu T and Ohmura T 1962 *Quantum Theory of Scattering* (Englewood Cliffs, NJ: Prentice-Hall)
Yoshioka H 1957 *J. Phys. Soc. Japan* **12** 618
Young A P and Rez P 1975 *J. Phys. C: Solid St. Phys.* **8** L1